Wettability, Water Droplet Dynamics and Freezing on Irregularly Roughened Stainless-Steel Surfaces for Ice Protection Application

By

© Kewei Shi

A Dissertation submitted to the School of Graduate Studies in partial fulfillment of the requirements for the degree of

Doctor of Philosophy

Faculty of Engineering and Applied Science

Memorial University of Newfoundland

February 2023

St. John's, Newfoundland and Labrador

Canada

Abstract

In the Arctic and other cold environments, ice can jeopardize local infrastructure, hinder field operations, damage buildings, offshore and ship superstructures and threaten life and property. Ice protection techniques are essential for equipment, structures, and personnel in these environments. Passive techniques rely on the physical properties of the target surface to dispose of ice or prevent ice build-up without any required external energy source. As a passive ice protection technology, (super)hydrophobic metallic surfaces can significantly delay the water droplet impact and freezing process. However, hydrophobic surfaces are not always icephobic. The droplet impact dynamics and freezing process on irregularly roughened (super)hydrophobic metal surfaces have not been fully understood. Previous experimental studies have limited the impact and freezing of water droplets on cold surfaces at room temperature. Most experimental and modelling investigations have also been limited to separately studying droplet impingement and freezing processes. Hence, this study aims to investigate dynamic wetting behaviours and freezing processes coupled with the impact dynamics of a water droplet on irregularly roughened metal surfaces experimentally and analytically.

To achieve this, irregularly roughened stainless-steel surfaces are fabricated by applying sandblasting, Zinc electrodeposition, stearic acid coating, and their combinations to receive various water wettability. The combination of electrodeposition and sandblasting can significantly increase the static contact angle from 91° ± 6° to 151° ± 2°, and these techniques can be applied on an industrial scale.

Surface dynamic wetting characterization illustrates the challenges of understanding the wetting dynamics on irregularly roughened surfaces, including dynamic contact angles and pinning that affect the sliding behaviour on inclined surfaces. These effects result in a poor

correlation between the measured dynamic contact angles and the observed critical sliding angles. Significant variations in the values of these dynamic wetting parameters are inherent to the heterogeneity of surface roughness, which limits the utility of standard dynamic wetting criteria. These findings have implications for academic and industrial research that focuses on achieving a uniform wettability of coating materials throughout their service life.

This study examines the droplet impact dynamics and freezing process on the above-fabricated surfaces through experiments and analytical analysis. The freezing delay of water droplets on the metal surfaces is measured in a cold room below the freezing point of water. The experimental results demonstrate that the superhydrophobic surfaces can significantly delay water droplet freezing, with up to a 57.47 ± 5.22 s freezing delay. Also, the freezing delay time increases with the static contact angles of water on the sample surfaces.

Furthermore, droplet impact from a higher distance on the same target surface leads to faster freezing. The heat transfer analysis demonstrates that a poor wetting condition (e.g., on the superhydrophobic surfaces) contributes to a smaller final contact area of a water droplet on the surface. The average freezing rate per unit mass is approximately proportional to the final contact area. This indicates the longer freezing delay on the (super)hydrophobic surfaces.

The analytical framework coupled the droplet impact dynamic and the freezing process. This model can estimate the total freezing delay time for a water droplet impact and freezing on a surface by evaluating the droplet impact and freezing processes. The experimental results validate the analytical predictions, which verify the feasibility of the method and assumptions used in this study. The analytical consideration not only provides a straightforward and valid solution but also simplifies the rather complicated mechanism of the droplet dynamic and freezing process on metal surfaces and provides a directly estimated total freezing delay time under different conditions. This

approach benefits engineers and reduces extensive and sophisticated computations. This fast and effective method for predicting the droplet impact and the freezing process has also filled the gap in the literature.

This comprehensive study of wettability, droplet impact dynamics and freezing processes connects surface wettability and ice repellency by investigating the wetting behaviour of water droplets on irregular rough solid surfaces; at the same time, connecting droplet impact dynamics and freezing delay and providing a better theoretical analysis of droplet impact, subcooling, nucleation, recondensation and solidification processes will benefit the research field.

Acknowledgement

I would like to express my sincerest gratitude to my supervisor Dr. Xili Duan. Without his assistance and support, I would not have been able to complete my study, research, and thesis. He has helped me to better understand how to become a qualified Ph.D. candidate by guiding me, to the best of his ability, on how to find a research direction, how to conduct a literature review, how to design and conduct experiments, how to connect the experiments with theories, and how to develop an analytical framework. These are abilities that I did not possess when I first started my doctoral program. When he also found it difficult, he was even more anxious to help me find a master or other specialist who could offer me any assistance. When I felt most helpless, he was the one who told me not to be anxious and not to panic and who helped me find the help I was looking for, so that I could continue my research.

I would also like to thank Dr. Kristin M. Poduska and Dr. Greg F. Naterer, who are the members of the supervisory committee, for their guidance and assistance with my research and Dr. Poduska for providing the room and equipment for sample preparation and guiding me through the surface treatment of the samples.

I gratefully acknowledge the financial support received from the Petroleum Research Newfoundland and Labrador (PRNL) and the School of Graduate Studies of the Memorial University of Newfoundland that made this research possible.

I would also like to express my sincere thanks to Dr. Geoff Rideout, who is the department head of Mechanical Engineering at Memorial University, Dr. Yuri Muzychka, who is the previous department head of Mechanical Engineering and a member of the thermal fluid group at Memorial University, Dr. Kevin Pope, who is a member of the thermal fluid group at Memorial University, and Craig Mitchell, who is the technician in the thermal fluid lab, for their time, efforts and for

their dedication and patient assistance in completing my theoretical and experimental research, and thanks to Jianxun Huang for his assistance in MATLAB coding for the analytical framework.

Finally, my sincerest thanks to my parents and my dearest friends who have supported me in any possible way throughout my doctoral study, offering me understanding, patience and encouragement, without which I could not have achieved this far.

Table of Contents

List of Tables

List of Figures

Nomenclature

A_c	The final contact area	[mm^2]
A_c^*	Dimensionless final contact area	$A_c^* = \frac{A_c}{A_i}$
A_i	Cross-sectional area of the water droplet	[m^2]
A_m	The surface area of a water molecule	[m^2]
A_p	The projected area	[m^2]
c_p	Specific heat capacity	[J/kg·°C]
D	The mass diffusivity	[m^2/s]
D_c	Droplet final contact diameter	[m]
D_c^*	Dimensionless final contact area diameter	$D_c^* = \frac{D_c}{D_i}$
D_i	Initial droplet diameter	[m]
e	Mathematical constant (Euler's number)	$e \approx 2.71828$
E	Energy	[J]
E^*_{diss}	The dimensionless during the droplet oscillation period	$E^*_{diss} = \frac{E_{diss}}{E_{s_i}}$
E^*_{ki}	The dimensionless initial kinetic energy	$E^*_{k_i} = \frac{E_{k_i}}{E_{s_i}}$
E^*_{sf}	The dimensionless surface energy of the droplet in the air	$E^*_{s_f} = \frac{E_{s_f}}{E_{s_i}}$
E_{diss}	The energy dissipation during the droplet oscillation period	[J]

E_{ki}	Initial kinetic energy:	[J]
E_{sf}	The surface energy of the droplet at the equilibrium stage	[J]
E_{si}	The initial surface energy of the droplet in the air	[J]
F_D	The net rate of attachment to the critical nucleus	[s^{-1}]
f	the geometrical factor for nucleation	
g	Acceleration of gravity	[m/s^2]
G	The Gibbs free energy	[J]
h	Falling height	[m]
h_D	Convective heat transfer coefficient = $\bar{N}u_d \cdot k / D_i$	[$W/(m^2 \cdot K)$]
H_{SL}	The latent heat of fusion	[J/kg]
i^*	The critical embryo size	
J	The nucleation rate	[s^{-1}]
k	Thermal conductivity	[W/m·K]
k_B	The Boltzmann constant 1.380649×10^{-23}	[J/K]
K_c	Kinetic constant	
N	The number of critical nuclei	
N_A	The Avogadro's constant $N_A = 6.022 \times 10^{23}$	[mol^{-1}]
n_L	The number density of molecules in the liquid particle	[m^{-3}]
n_S	The number density of molecules in the solid particle	[m^{-3}]
Nu_D	Nusselt number for a falling droplet = $2 + 0.6re_d^{1/2}Pr^{1/3}$	
Pr	Prandtl number	$\mathrm{Pr} = \frac{\mu c_p}{k}$
q	Freezing rate	[W]

Q	Amount of heat transfer	[J]
r^*	The critical nucleation radius	[m]
Re	Reynolds number	$\mathrm{Re} = \frac{\rho u d_i}{\mu}$
RH	Relative humidity	
r_{mean}	The mean particle separation distance	[m]
R_p	The size of the nucleating particle	[m]
s	The interface location	[m]
S	Surface energy	[J]
Ste	Stefan number	$\mathrm{Ste} = \frac{c_p \Delta T}{H_{SL}}$
$t*$	Dimensionless icing delay time	$t^* = \frac{t_{freezing}}{t_{falling}}$
T_∞	The temperature in the cold room	[°C]/[K]
T_{cp}	The temperature of the cold plate	[°C]/[K]
$t_{dynamic}$	The droplet dynamic time	[s]
$t_{falling}$	Falling time	[s]
$t_{freezing}$	The total freezing delay time	[s]
$t_{freezing, m}$	The total freezing delay time per unit mass	[s/kg]
T_i	Initial temperature	[°C]
T_I	The temperature of the ice	[°C]
T_{impact}	The droplet impact temperature	[°C]
T_{int}	The temperature of the interface	[°C]

T_m	The melting/freezing temperature	[°C]
t_n	The nucleation time	[s]
T_n	The nucleation temperature	[°C]
t_s	The equilibrium solidification time	[s]
T_{sub}	Temperature of substrates	[°C]
T_{tb}	The temperature of the thermal bath	[°C]
T_w	The temperature of a water droplet	[°C]
u	Velocity of droplet	[m/s]
V_c	The size of the critical nucleus	[m^3]
V_D	The volume of the water droplet	[m^3]
We	Weber number	$\mathrm{We} = \frac{\rho u^2 D_i}{\gamma}$
We_i	Impact Weber number	$\mathrm{We}_i = \frac{\mathrm{We}}{0.5(1-\cos\theta_a)}$
Z_{hete}	The heterogeneous Zeldovich factor	
ΔD	The base length change	[m]
ΔG^*	The critical Gibbs energy for nucleation	[J]
ΔG_V	The volumetric Gibbs energy change	[J/m^3]

Greek

α	The thermal diffusivity	[m^2/s]
γ	The surface tension of a liquid	[N/m]
δ	The thickness of the substrate	[m]
θ	Contact angle	[°]

θ_a	Advancing contact angle	[°]
θ_{led}	The contact angles at the leading edge of a droplet pining on a tilted surface	[°]
θ_r	Receding contact angle	[°]
θ_s	Static contact angle	[°]
θ_{sl}	Sliding angle	[°]
θ_t	Surface tilt angle	[°]
θ_{tra}	The contact angles at the trailing edge of a droplet pining on a tilted surface	[°]
μ	Dynamic viscosity	[Pa·s]
ρ	Density	[kg/m^3]

Chapter 1 Introduction[1]

This chapter focuses on the background of the research and the problems to be solved in this thesis. Section 1.1 briefly introduces the background of this thesis. Section1.2 presents the ice problems on offshore structures. Section 1.3 presents the motivation and objectives of this comprehensive study, and section 1.4 presents the thesis structure.

1.1 Background

Undesirable ice formation has become a significant challenge for cold regions, where severe icing can hinder economic activities and damage engineering structures such as power transmission equipment, communication systems, marine vessels, and offshore platforms [1–5]. Falling ice and surface freezing can result in the injury or death of personnel. Ice formation and accumulation in cold offshore harsh environments may create significant hazards and hinder field operations [5–8]. The harsh marine environments can include freezing temperatures, strong waves and wind, high humidity and high salinity, all of which can be challenging for crew and offshore structures [9,10]. These conditions are typical in the harsh environments of the Arctic and Subarctic regions. Increasing offshore resources exploration and transportation development in these regions require more effective ice protection techniques.

---

[1] The content in Section 1.1 and Section1.2 includes parts of a previously published paper (K. Shi, X. Duan, A Review of Ice Protection Techniques for Structures in the Arctic and Offshore Harsh Environments, J. Offshore Mech. Arct. Eng. 143 (2021).) The author of this thesis is the first author of the published paper. The first author conducted a comprehensive study on ice protection techniques for structures in the arctic and offshore harsh environments, identified the research topic, prepared the manuscripts and the corresponding revisions. Dr. Xili Duan, as the second author, provided his professional suggestions on this topic and assisted in preparing the manuscript and the corresponding revisions.

The ice protection techniques can delay atmospheric and/or sea spray ice and/or keep the ice from accumulating on offshore structures in the Arctic or other harsh marine environments. These methods can be divided into two categories: de-icing and anti-icing methods. De-icing refers to those processes of removing snow, ice, or frost from the surface of structures and equipment [5,11–14]. On the other hand, anti-icing methods can delay ice nucleation, prevent ice from forming on the surfaces, or decrease the ice adhesion so that it can be easily removed afterwards [5,15–17]. Some ice protection approaches can not only melt the ice formed and accumulated on the surface (for example, electric heating coatings) but also delay the reformation of ice for a certain period (for example, superhydrophobic surfaces, slippery liquid infused porous surfaces (SLIPS)) or decrease the adhesion of ice and make mechanical removal more manageable (for example, self-lubricating liquid water layer (SLWL), low-interfacial toughness (LIT) materials/coatings).

1.2 Ice problems occurred on offshore structures

When the ambient temperature drops to -1.7 °C, wind speed is above 9 m/s, and the temperature of seawater droplets decreases to 7 °C, ice starts to form on offshore structures [18]. Many factors affect the icing on offshore structures. These include, for example, the temperature of sea surface water, wind speed, ambient temperature, the humidity of the atmosphere, dimension of droplets, seasons, ocean currents, state of the ocean, sizes and types of structures, and the influence icing on offshore structures [18–20].

There are two primary sources of icing, i.e., sea spray and atmospheric icing, for offshore structures and marine vessels: sea spray and atmospheric icing, as shown in Figure 1-1. Figure 1-2 shows a more detailed breakdown of the causes of offshore icing in Arctic sea areas [3].

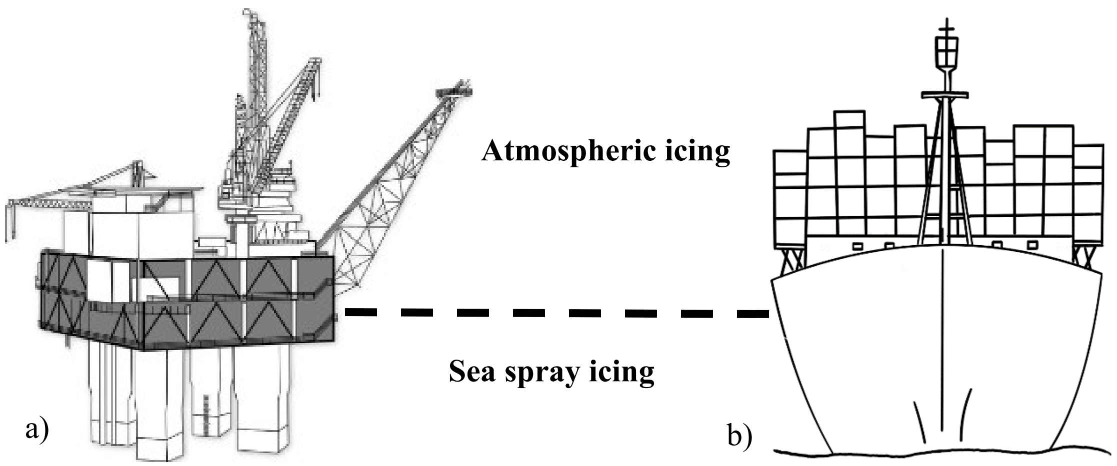

Figure 1-1 Icing sources for a) offshore structures, b) marine ships. Atmospheric icing is formed by supercooled water vapour, forming raindrops, cumulus clouds, clouds, or ice that distribute on marine and offshore structures. Sea spray icing occurs when the waves from the ocean hit the bare surface of the offshore or marine vessel and then become ice under the frozen state. The figure is adapted from a previously published paper by the author [21] with the permission of ASME International.

Sea spray icing happens when wave or wind-generated spray from the ocean impacts the exposed surface of an offshore structure or a marine vessel and becomes ice during freezing[18,22,23]. Sea spray icing accounts for 50% of all causes of marine icing problems, as shown in Figure 1-2a. Also, it has been generally considered the most serious menace to the safety of marine and offshore structures [18,22,24–29]. However, a few researchers hold different views on this point [3,30]. Several parameters affect sea spray icing, for example, the sizes of sea spray aerosol [31,32], wind speed [18,33–37], air (ambient) temperature [24,38–40], ocean surface temperature [39,41,42]. Figure 1-2b illustrates the percentages of sea spray icing in different areas.

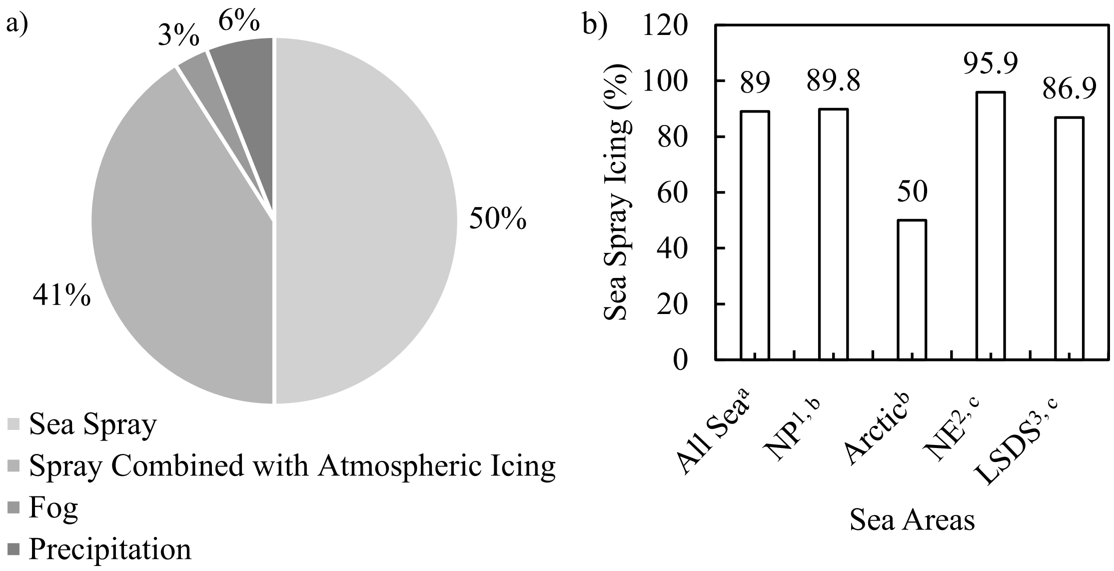

Figure 1-2 a) The Cause of Icing on Offshore Structures, b) Seaspray icing in different ocean areas: 1 represents North Pacific, 2 represents NE Newfoundland Shelf, 3 represents the Labrador Sea and Dabis Strait; [a]see reference[43], [b]see reference[44], [c]see reference[45]. The figure is adapted from a previously published paper by the author [21] with the permission of ASME International.

Seaspray icing can cause severe hazards and safety problems for marine and offshore structures. For example, it can diminish the stability of marine structures or devices, and the overladed ice will destroy the superstructures or the deck equipment. Also, it covers and blocks windows, lifesaving and firefighting equipment and incapacitates cranes, radar, communication antennas, and winches on marine structures. Further, it hinders vent system inlets, valves, and hatches. Finally, it leads to slipping threats, for example, slippery handrails, decks, and stairs, and contributes to the breakdown of infrastructures and operational equipment [15,18,23].

Atmospheric icing is due to the water vapour, supercooled fog or cloud droplets freezing on marine and offshore structures. Examples include frost, snow, freezing rain and drizzle, and sleet [3,15,23]. This type of icing accounts for 41% of the overall causes of icing in the Arctic area [3].

Although atmospheric icing is not as frequent as spray icing, it can still cause hazards and harm to life and property safety. For instance, atmospheric icing can develop significantly on the mesh, lattice, and filigree structures. Also, it can be found on the railing, antenna cables, winches, cranes, hatches, lifesaving and firefighting equipment. Atmospheric icing can lead to, sometimes, falling ice from high positions, which can threaten personal life and property safety. The icing on communication antennas and radar can induce the malfunction of communication and radar detecting systems. Also, it develops a slippery deck and stairs, which contributes to personal hazards[1,3,46].

Either sea spray icing or atmospheric icing can appear in two forms under different thermal conditions: glaze ice or rime ice. Under a wet state, glaze ice is generated when the surface temperature is around 0 °C. Rime ice grows in a dry condition when the surface temperature is below 0 °C, and the density of rime ice is relatively lower than glaze[1,3]. The glaze is arduous to remove due to its high density, high adherence, and firmness.

1.3 Motivation and objectives

Ice can cause serious hazards that threaten life and other properties. Many researchers attempt to develop techniques to remove or prevent ice accretion. These approaches refer to the methods and techniques that can delay or avoid ice formation or reduce the ice adhesion to remove the formed ice easily by itself or other means. As explained earlier, ice protection techniques are also known as de-icing or anti-icing techniques[1,4,5,15,23,47]. De-icing/anti-icing technology can be divided into two categories depending on whether energy is required, which are passive and active techniques. Passive techniques use the physical properties of the target surface to dispose of ice or stop the aggregation of ice. In contrast, active techniques utilize an external energy supplier to prevent ice formation and accumulation or melt and remove the ice after ice aggregation, such as defrosting in refrigerators.

One promising passive anti-icing technique is designing a surface with low surface energy to repel water and prevent icing. However, hydrophobic surfaces are not always icephobic, which has been explained by many researchers [48–51]. The relationship between surface wettability and icephobicity is still unclear. The freezing process and droplet dynamics of a water droplet impact on roughened superhydrophobic surfaces have not been fully understood. Hence, the objectives of this thesis are:

1. to fabricate irregularly roughened stainless steel (super)hydrophobic surfaces via sandblasting and electrodeposition techniques since these techniques are widely used in industry and can be applied to large-scale applications.
2. to understand dynamic wetting behaviours of irregularly roughened metal surfaces.
3. to understand the impact dynamics and freezing process of a water droplet on irregularly roughened surfaces.
4. to develop an analytical model for the impact dynamics and freezing process of a water droplet on irregularly roughened surfaces.

The flow chart shown in Figure 1-3 brief demonstrates the methodology to achieve these objectives.

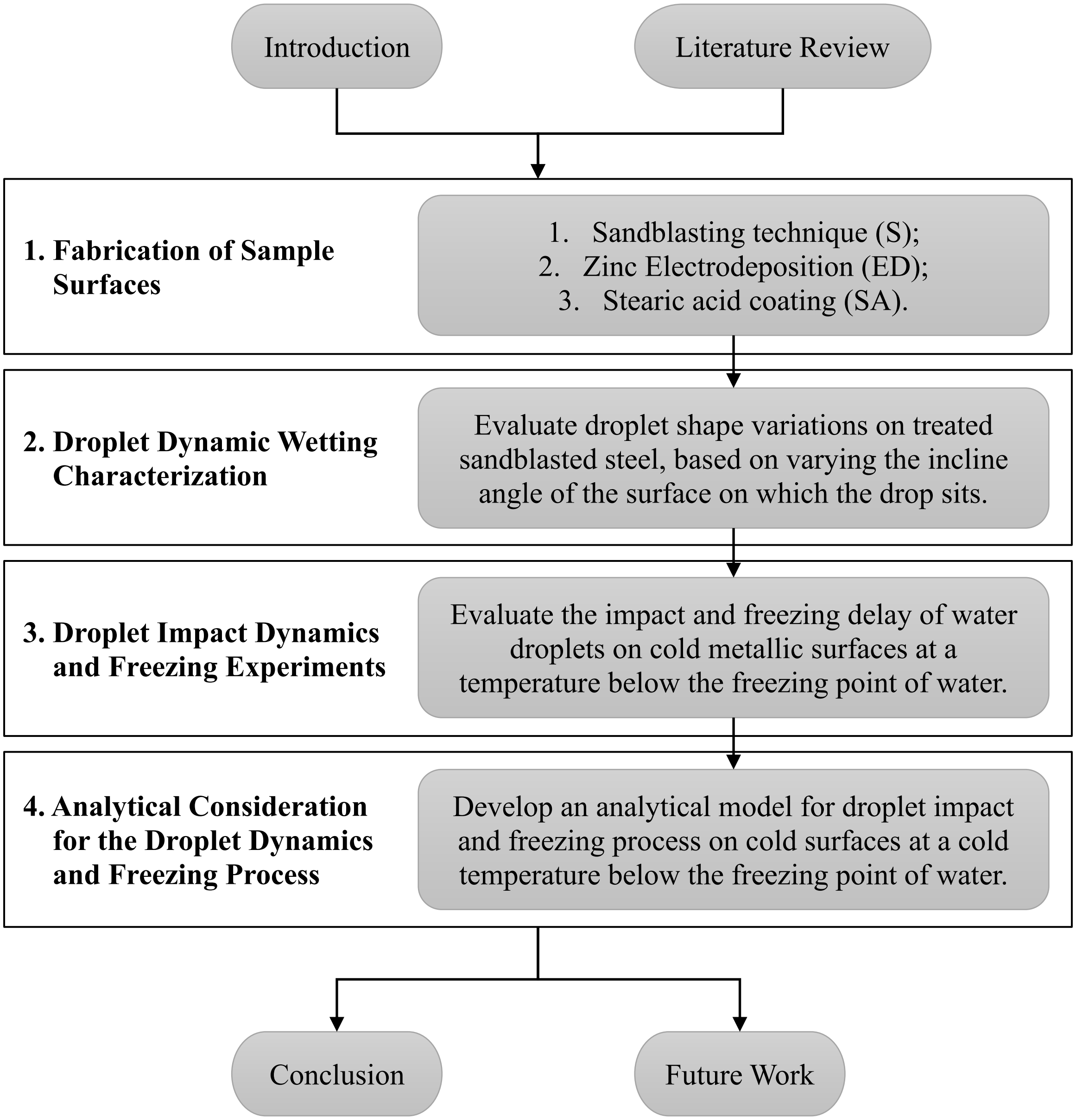

Figure 1-3 Flow chart outlining the methodologies to achieve the objectives in this thesis

1.4 Thesis structure

This thesis is presented in seven chapters shown as follows.

- Chapter 1 presents the background of this study, objectives and a brief introduction to the methodologies used in this study.

- Chapter 2 presents a comprehensive literature review of passive ice protection and surface fabrication techniques.
- Chapter 3 introduces the detailed fabrication and characterization of the metal surfaces.
- Chapter 4 presents the experiments which report details of droplet shape variations on coated sandblasted steel based on varying the incline angle of the surface on which the drop sits.
- Chapter 5 presents the experiments and heat transfer analysis, including dimensional analysis, on the droplet impact and freezing delay processes of a water droplet on the cold metallic surface at a cold temperature below the freezing point of water.
- Chapter 6 presents the analytical consideration and validation of a droplet impact and freezing delay processes of a water droplet on the cold metallic surface at a cold temperature below the freezing point of water.
- Chapter 7 presents the conclusions and contributions of the study and suggests recommendations for future work.

Chapter 2 Ice Protection and Surface Fabrication Techniques[2]

2.1 Introduction

This chapter focuses on the two main categories of ice protection and surface fabrication techniques in the literature. Section2.2 and Section2.3 present the active and passive ice protection techniques, respectively. Section 2.4 presents the fabrication techniques for air film isolating surfaces. Section 2.5 presents the summary of this chapter.

2.2 Active ice protection techniques

2.2.1 Mechanical de-icing techniques

Mechanical de-icing methods utilize external forces, for example, aerodynamic force, centrifugal force, vibration, or workforce, to break and remove ice from the target surfaces.

---

[2] The main content in this chapter is a part of a previously published paper (K. Shi, X. Duan, A Review of Ice Protection Techniques for Structures in the Arctic and Offshore Harsh Environments, J. Offshore Mech. Arct. Eng. 143 (2021).) The author of this thesis is the first author of the published paper. The first author conducted a comprehensive study on ice protection techniques for structures in the arctic and offshore harsh environments, identified the research topic, prepared the manuscripts and the corresponding revisions. Dr. Xili Duan, as the second author, provided his professional suggestions on this topic and assisted in preparing the manuscript and the corresponding revisions

Figure 2-1 Manual de-icing on a ship. The figure is adapted from [23] with the permission of Elsevier Science and Technology Journals.

As depicted in Figure 2-1, the manual method is a traditional technique used primarily on marine vessels and offshore structures, especially during the 1980s [52]. It consumes low energy and requires no maintenance for tools, but it is unsafe for individuals operating on high-level superstructures. Also, it is only possible for accessible areas and may need to be done multiple times during severely cold weather if there is significant ice accretion. The commonly used tools are hammers and shovels, which are not initially intended for ice protection purposes [5].

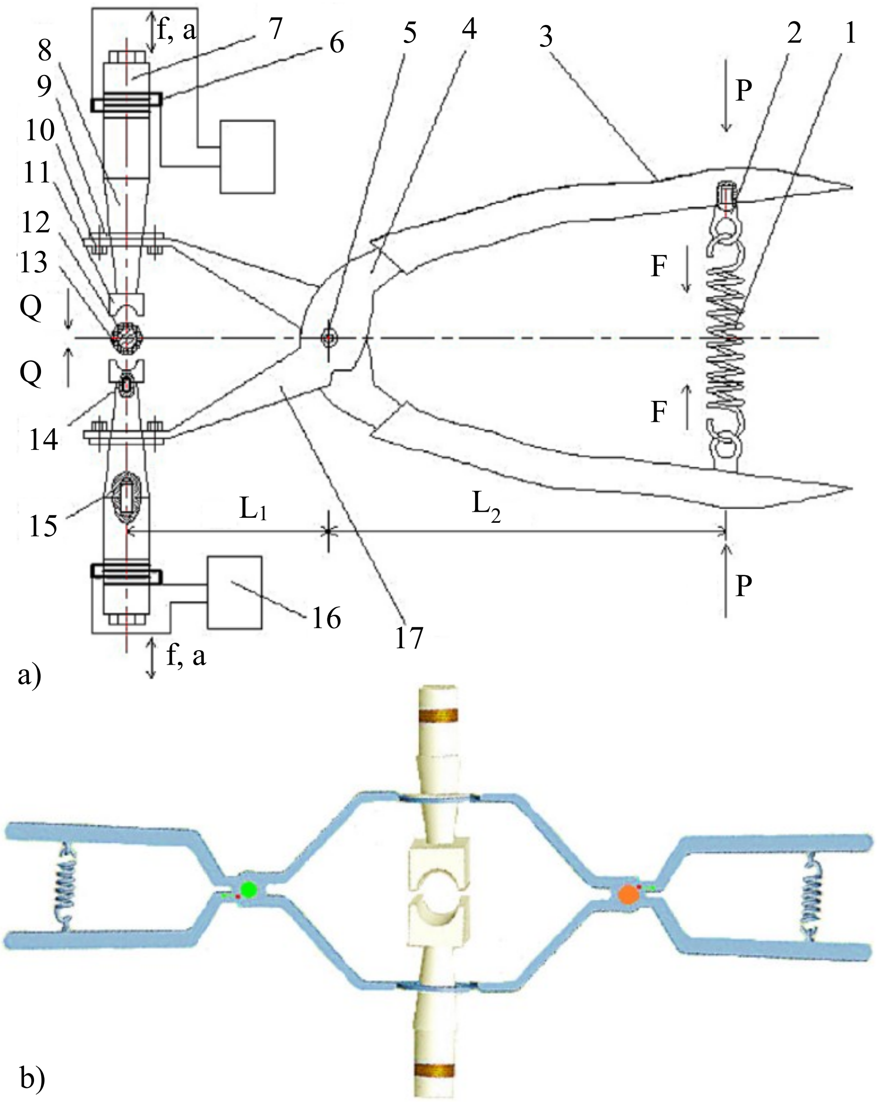

Figure 2-2 a) Schematic of the ultrasonic de-icing device, b) 3-D diagram of the ultrasonic de-icing device (two clamps). 1-tension spring, 2-hanging ring, 3-insulation sleeve, 4-de-icing plier handlebars, 5-rivet, 6-electrode, 7-sandwich piezoelectric transducer, 8-amplitude transformer, 9-flange, 10-bolt, 11-tool head, 12-transmission line, 13-ice cover, 14-the first bolt, 15-the second bolt, 16-ultrasonic generator, 17-de-icing tong jaw. The figure is adapted from [53] with the permission of Elsevier Science and Technology Journals.

A mechanical vibration system was developed for aircraft de-icing. The system contains a motor that drives an eccentric mass in rotational motion. The eccentric weight moves the outer surface, which causes the separation of ice from the aircraft surface [12].

Ultrasonic de-icing methods are based on cavitation, heating, and predominately mechanical effects induced by ultrasonic vibration to remove ice from target surfaces. Such a method takes advantage of the fact that the adhesive bond of the ice-substrate interface is relatively weak in shear strength. It uses the shear force generated by the ultrasonic wave, which is induced by the electrical signal in the thin plate, to overcome the adhesion strength between the ice and the target surface. Figure 2-2 illustrates an ultrasonic de-icing device for transmission lines. It is reported that this device can avoid not only damaging transmission lines but also improve de-icing efficiency and remove ice from the power line [53]. These methods are proven to be energy-saving, simple, cheap, applicable on most aircraft, wind turbines, and transmission lines, and can also be adapted to most marine and offshore structures [53–57].

2.2.2 Thermal techniques

Thermal ice protection techniques work by applying heat to the target surfaces. These methods can be anti-icing techniques when the heat is applied in advance, and the surface temperature is maintained slightly higher than the icing point to prevent ice formation on the target surfaces. Thermal approaches can also be de-icing techniques to melt ice after it forms on surfaces. For example, hot air and steam can be ejected on the targeted surfaces to melt ice. This technique is relatively inexpensive and requires minimal instruction, but it often has to be operated by workers, and at least three persons are required [5]. Also, the workers are exposed to a harsh environment when they operate the de-icing systems. Thermal methods also require additional pipes and rearrangement in different regions. Thus, it is better to use these techniques for short-term ice prevention [58].

High-speed hot water or steam is another option that can provide thermal and mechanical abilities to melt and cut large ice accumulated on structures into small blocks. Steam can be generated from the boiler or exhaust boiler on ships. The cost mainly depends on the arrangement of pipes and the amount of water and steam consumed while de-icing. This technique cannot protect the complex superstructures on offshore platforms and vessels [5]. The mechanical and thermal shock of high-speed water and steam can break fragile equipment, glass, delicate surfaces, and sensitive electronics [5,59]. If not removed in time after de-icing, excess water residuals or condensed steam may freeze again, which can lead to slippery conditions on the floors and steps, among other hazards.

Table 2-1 The lowest power required for thermal de-icing devices. The table is adapted from a previously published paper by the author [21] with the permission of ASME International.

Power required	Areas
300 W/m^2	Open deck, helicopter deck, gangways, stairs, etc.
200 W/m^2	Superstructures
50 W/m^2	Railings with electrical heat tracing pulled inside the tubular steel handrail

Electrothermal techniques can also be good options to address the icing problem for offshore structures. It is proposed that these methods be implemented on support structures below the main deck, pipe sections, air intakes, bulkheads, hatches (including parts of the lunar basin), and the basement deck [23]. One form of electrical heating technique, which is called electrical heating tracing (EHT), can be used on offshore platforms. This method is generally easy to design and arrange with high temperatures from 200°C to 593°C. Still, there are limitations with this method, including high-runaway temperature and more care required for the circuits due to exposure to high temperatures. Table 2-1 presents the lowest energy required in different parts of marine vessels and offshore structures [60], and other details are provided in the same reference. Other options are electric heating coatings [60–63], pulse interfacial de-icing [5,64,65], and ice dielectric heating [66,67], which will be further discussed in the following sections.

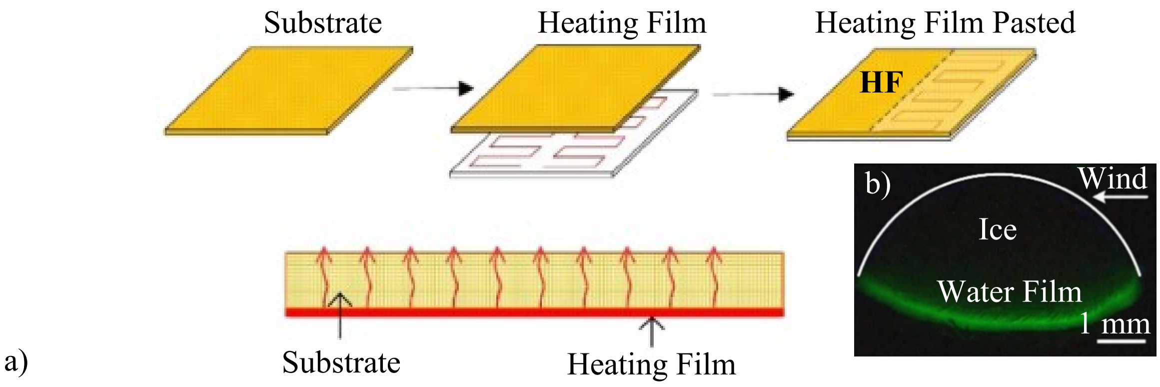

Figure 2-3 a) Schematic of the fabrication process and the traditional electrical heating film (HF) heating mode. b) The momentary fluorescence images of the ice drop before it was precisely blown away on HF. The figure is adapted from [61] with the permission of Elsevier Science and Technology Journals.

The traditional heating film (HF) is embedded in the substrate, as shown in Figure 2-3. A water film is formed between the ice and the coating surface, as shown in Figure 2-3b, so the adhesion of ice is significantly reduced. External forces can easily remove the ice, for example, vibration, gravity, wind force, or workforce [61]. The electric heating coating can be applied in fibre-reinforced plastic de-/anti-icing systems such as aircraft wings and wind turbines. The application on metal surfaces is untested and is quite power-consuming (0.98 W/cm^2) when applied to large areas for de-icing [61]. Liu et al. investigated an electric heating coating (EHC) [63], as shown in

Figure 2-4. This coating can significantly reduce the ice adhesion strength, as verified experimentally. EHC has a power consumption of 0.89 W/cm^2, which is similar to that of HF. However, it has the same disadvantages as HF. Its application on ships and offshore structures is limited due to the number of metal surfaces on these structures, which can lead to an electric shock hazard.

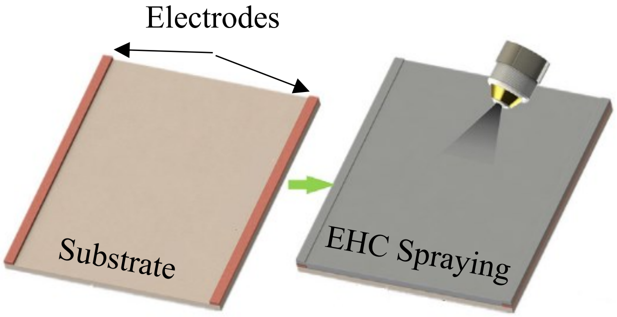

Figure 2-4 Schematic of the smooth electrical heating coating (EHC) fabrication. The figure is adapted from [63] with the permission of Elsevier Science and Technology Journals.

The infrared anti/de-icing technique can melt and prevent the accumulation of ice and snow by heating the ice or target surfaces without direct contact. Figure 2-5 illustrates the infrared de-icing experiments conducted by Koenig et al. (2011). They found that the melting rate did not change significantly over time with regard to ice thickness. Also, the melted water could block heat transmission from the infrared heater to the ice-water interface, which can slow down the melting rate. Nevertheless, they proposed that ice can absorb the most infrared energy between 0.4

and 20 μm [68]. A small amount of infrared energy with a wavelength greater than 3 μm can be transmitted through sub-millimetre-thick ice.

Consequently, other materials that do not absorb wavelengths longer than about 3 μm must be chosen carefully to prevent fire danger [5,68]. However, this is difficult to accomplish. For instance, polished aluminium absorbs 10% of incident radiation for a given wavelength, while oils absorb 90%. Consequently, greases, oils, and numerous segments in the nacelle can rapidly overheat [5]. This situation requires exceptional precautionary safety measures. Emitters can also be expensive, and infrared energy may damage surfaces that are intolerant of heat or waves. Therefore, locations on offshore structures that can use this technique are limited to walkways, stairs, cranes, windlasses, valves, firefighting and rescue equipment, and air intakes.

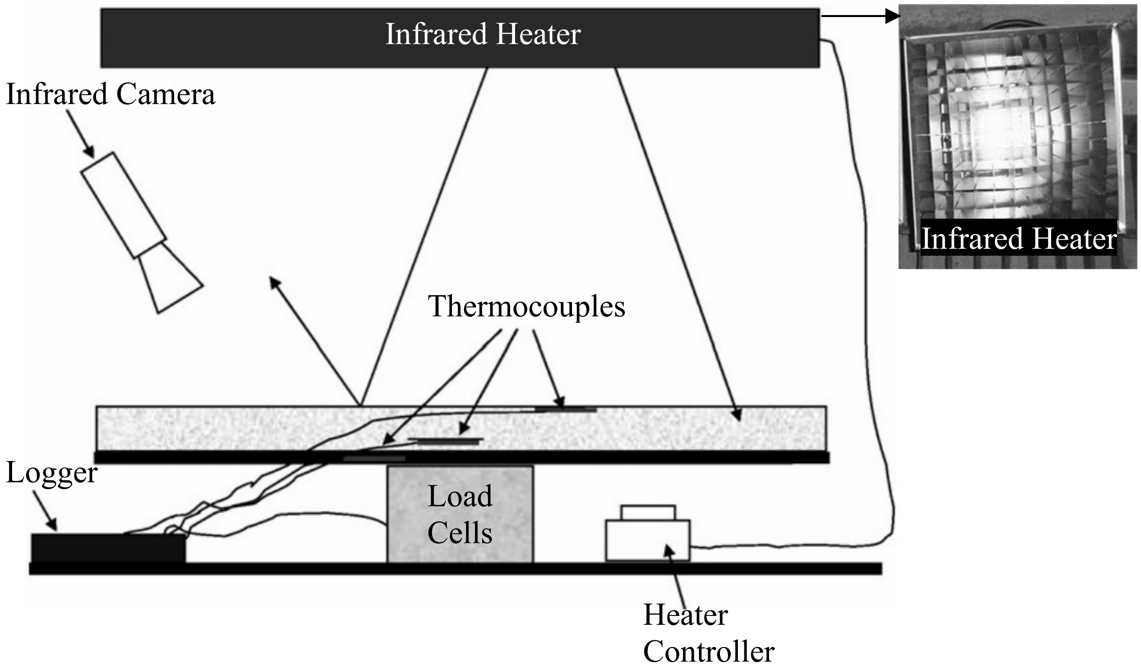

Figure 2-5 Schematic of infrared de-icing experiments by Koenig et al. The figure is adapted from [68] with the permission of Elsevier Science and Technology Journals.

Pulse electrothermal de-icing methods [5,64,65] warm the interface between the ice and the target surface by applying heat as a short pulse rather than continuously (compared to the traditional electric thermal techniques). The melted layer of ice acts as a lubricating water film that decreases the ice adhesion strength between the substrate and ice. The ice above the thin water film can be removed by gravity or other external forces, such as wind, mechanical vibration, or workforce. The Pulse Electro-Thermal De-icer (PETD) [64] is shown in Figure 2-6. It melts the interface immediately with less heat loss during the short heating (melting) process. This method is relatively inexpensive with low power consumption because it requires only a small amount of ice to be melted by a short "heat pulse". This de-icing technology can be applied to aeroplanes, bridges, car windshields, and refrigerator evaporator coils [5,64,65]. When the PETD is used for de-icing, there is a falling ice hazard which requires caution during operation. The potential risk of electrical shock should also be considered when this method is applied in offshore environments (high humidity) on large-scale surfaces. Also, the application of PETD on metal surfaces has not been tested.

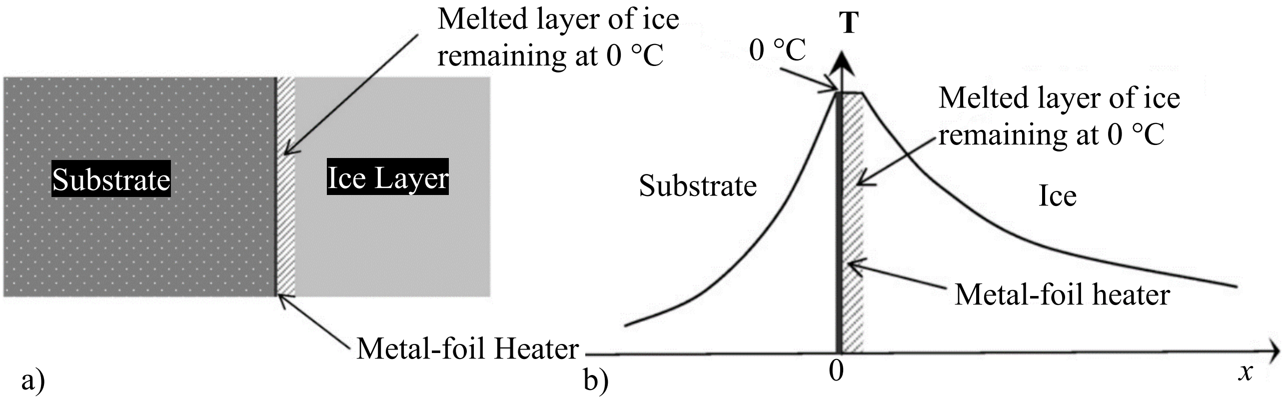

Figure 2-6 Schematic of a) mechanism of PETD, b) temperature distribution along PETD. The figure is adapted from [64] with the permission of Elsevier Science and Technology Journals.

Dielectric heating technology is used for food defrosting, and some researchers proposed that this can be used for de-icing windows and complex surfaces [66,67]. The application of offshore structures is unknown and has not been investigated. Therefore, the dielectric heating technique is not recommended for offshore structure de-icing until further research demonstrates its feasibility.

2.2.3 Chemical ice protection techniques

Chemical anti/de-icing techniques prevent ice accretion using liquid or solid chemical compounds that are applied over the surface of a structure to lower the freezing point of the subsequent ice/chemical arrangement. This method has been widely used in various fields, for example, aircraft, wind turbines, highways, pavement, bridges, and marine and offshore structures. Chemical deicers include chlorides, acetates, glycol-based chemicals, and other categories.

Table 2-2 Chloride deicers, the table is adapted from a previously published paper by the author [21] with the permission of ASME International.

Name	Cost (USD)	Working Temp.	Pros and Cons
NaCl	\$20-40/ton	7 to -10 °C	Pros: Inexpensive, easily applied, and active at a warm temperature. Cons: Operates slowly, corrosive, Ineffective.
$CaCl_2$	\$132/metric ton	-45 °C	Pros: Hygroscopic, effective in low temperatures, operates relatively quickly, exothermic. Cons: Corrosive, slippery residue, expensive.
$MgCl_2$	\$0.10/L	-15 °C	Pros: Similar to $CaCl_2$ Cons: Corrosive

Chlorides are the most commonly used deicers on highways, pathways, and runways due to their low cost and widespread availability [13,14,69–73]. The relatively high corrosivity of chlorides has limited their use on marine and offshore structures. Table 2-2 shows the chlorides that are available for de-icing [5,23,74], including sodium chloride (NaCl), calcium chloride ($CaCl_2$), magnesium chloride ($MgCl_2$) and potassium chloride (KCl).

Table 2-3 Acetate deicers, the table is adapted from a previously published paper by the author [21] with the permission of ASME International.

Name	Cost (USD)	Working Temp.	Pros and Cons
$(CH_3COO)_2Mg$	\$300-660/metric ton	8 °C	Pros: Low corrosivity Cons: Expensive, high BOD, relatively slow acting at low temperature.
CH_3COOK	\$660/metric ton	26 °C	Pros: Low corrosion rate. Cons: Damage brakes, damage cadmium, high BOD.
CH_3COONa	\$3.33/L	-15 °C	Pros: Effective in deep snow, low overall corrosivity. Cons: Corrosive for aircraft, Destructive, Expensive.

Due to their lesser corrosivity, acetates have been used on aircraft, highways, and runways instead of chlorides. Still, acetates are more expensive than chlorides and have high biochemical oxygen demand (BOD), which contributes to water pollution. Three acetates are presented in Table 2-3 for comparison; magnesium acetate ($(CH_3COO)_2Mg$), potassium acetate (CH_3COOK), and sodium acetate (CH_3COOK) [13,14,23,74–78]. Potassium acetate has quite a low corrosive rate and can be used on highways and runways, but it is suspected to ruin brakes and cadmium components on aeroplanes. Sodium acetate is also corrosive to aircraft. When sodium acetate contacts concrete, it induces alkali-silica reactions and will damage buildings and marine and offshore concrete structures [23].

Table 2-4 Glycol-based deicers, the table is adapted from a previously published paper by the author [21] with the permission of ASME International.

Name	Cost (USD)	Working Temp.	Pros and Cons
EG	$1.30-1.82/L	-40 to -46 °C	Pros: Fast effect Cons: Toxic, slippery, expensive.
PG	Same as EG	-40 to -46 °C	Pros: Fast effect, non-toxic. Cons: High BOD, causes eutrophication in water, vapour causes nausea, slippery.

Glycol-based deicers are used for aeroplane de-icing and anti-icing prior to taking off. Two main glycol-based chemicals are presented in Table 2-4. Ethylene glycol (EG) is rarely used due to its toxicity, while propylene glycol (PG) is non-toxic but requires a high BOD value and generates eutrophication in water. When PG vapour ventilates into living areas, it can cause nausea in individuals. Also, glycol-based liquids can make pathways slippery [13,23,79–82].

Table 2-5 Other deicers, the table is adapted from a previously published paper by the author [21] with the permission of ASME International.

Name	Cost (USD)	Working Temp.	Pros and Cons
HCOONa	\$2000/metric ton	-18 °C	Pros: Low corrosivity and BOD. Cons: Expensive, damage zinc-coated galvanized steel.
Urea	\$25/25 kg bag of pellets	-4 °C	Pros: Low corrosivity Cons: Ineffective in low temperatures, high BOD, and high aquatic toxicity, decomposition releases ammonia gas.
Sugar-beet-based products	\$0.50/L	-32 °C	Pros: Minimal corrosivity, high viscosity. Cons: Expensive.
Corn-based products	\$1.75/L	-40 °C	Similar to sugar-beet-based products
Alcohol-based products	\$15.00/ton	-18 °C	Pros: Low BOD, residual effect, low corrosivity, high viscosity. Cons: Slippery.

Other deicers used on runways and pavement include sodium formate (HCOONa), urea, and sugar-based chemicals. Further details are presented in Table 2-5. Sodium formate requires low BOD and has a lower corrosion rate, but this product can damage zinc-coated galvanized steel and is only available in the solid-state [73,83]. Urea has a low corrosion rate but demands high BOD, has high aquatic toxicity, and can also release ammonia gas during decomposing[13,84]. Sugar-based products are produced by agriculture, such as sugar beets, corn, and alcohol. These products have minimal corrosivity and perform well at low temperatures [11,13,14,85,86]. Although they are expensive, sugar-based products can be used on marine and offshore for de-icing purposes. The advantages of these products include their high viscosity, minimal corrosivity, effectiveness in low temperatures, and residual effectiveness between storms [23].

2.3 Passive ice protection techniques

Passive techniques rely on the physical properties of the target surface to dispose of ice or stop ice aggregation without external energy sources. The idea is to create and maintain the icephobicity properties of the target surfaces. These strategies aim to reduce operational costs and keep structures free from ice without requiring power or other control systems. There are many passive ice protection technologies, for example, the air/oil/water film isolating technique. In this section, seven passive techniques have been reviewed.

2.3.1 The air film isolating technique

The air film isolating surfaces can cause water droplets to bounce off from the surface before freezing, therefore preventing ice formation. When the ice forms on these surfaces, the ice adhesion strength could be lowered by the air pockets so that the ice can be removed easily by external forces, for example, gravity, vibration, and workforce [87–89]. The air pockets also reduce heat conduction between the sub-freezing solid surface and the overlying droplet [7], preventing or delaying the icing process. As shown in Figure 2-7, air film isolating surfaces are usually designed to have patterned structures inspired by lotus leaves and water striders. These structures allow air to become trapped between the surface and the liquid above.

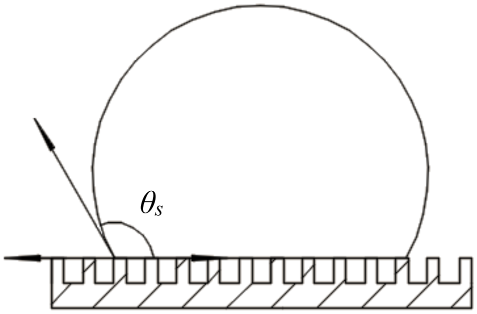

Figure 2-7 The Cassie-Baxter model (θ_s is the apparent static contact angle). The figure is adapted from a previously published paper by the author [21] with the permission of ASME International.

Further, when a water droplet impacts a hydrophobic surface, it spreads significantly less than on a hydrophilic surface. The reduced contact area between the cold surface and the droplet decreases the overall heat transfer rate between the two, leading to an icing delay [90,91]. Some scholars verified that air film isolating surfaces could also decrease ice adhesion. Therefore, the ice can be manually removed more efficiently or even by gravity [87,89,92–95]. Some other researchers argue that these structured surfaces can increase ice adhesion strength significantly when the water droplet impacts the surfaces and presses the air out of the microstructures, which means a Cassie–Baxter to Wenzel state transition [6]. This transition can occur in humid environments, such as offshore ones. When this happens, ice formed on the structured (roughened) surface is much more firmly attached to these surfaces than on smooth surfaces because the roughness can increase the ice adhesion strength after the droplet freezes on the surfaces [51,96]. The relative humidity of the atmosphere can also severely influence surface icephobicity because of excessive condensation in humid environments [97]. Condensation can create a thin water film over the designed surfaces. Therefore, sea spray or atmospheric icing occurs on the thin condensed water film rather than on the designed superhydrophobic surfaces, leading to surface failure for ice protection. Extreme conditions in harsh environments can also damage the micro and nanostructures, for example, volume change while freezing, high pressure, corrosion, and the effect of shear stress. Ice adhesion strength increases up to three times [98].

2.3.2 The oil film isolating technique

The oil film isolating technique is also known as the slippery liquid-infused porous surfaces (SLIPS) [99,100]. The technique has been proposed to tackle the micro and nanostructures of superhydrophobic surfaces damaged by extreme conditions. For example, severe condensation can lead to the failure of the anti-icing performance of superhydrophobic surfaces in high-humidity environments. SLIPS is smooth, without surface defects, and can be self-repaired by capillary forces. It has been reported that the SLIPS present excellent superhydrophobicity, and the contact angle hysteresis is lower than 2.5° [100]. Due to the lubricated features, SLIPS can also prevent water droplets from pinning on the surfaces [101]. Even in an environment with relative humidity higher than 60%, SLIPS-coated substrates remain ice/frost-free by effectively shedding condensed water droplets [100]. However, the drain of lubricating liquid will lead to the loss of superhydrophobicity and ice prevention ability of the SLIPS when the lubricant in the porous structure is depleted [101–103]. Kim et al. presented the aluminium-based SLIPS and evaluated their anti-ice and anti-frost properties [99]. The results demonstrated that this aluminium-based SLIPS could significantly reduce ice accumulation and ice adhesion strength. However, ice was still generated on the surface because several droplets were pinned on the defect points of the surface and eventually solidified into large ice beads. Coady et al. found that the UV-cured polymer networks infused technique can improve the icephobicity and longevity of the SLIPS [93]; however, its abrasive and corrosive characteristics are still unknown. Liu et al. tested the durability of their SLIPS (a heptadecafluorodecyl trimethoxysilane-fluorinated hierarchically micro-structured silicone rubber surface), and the freezing time of water droplets significantly decreased after two freezing and melting cycles due to the gradual depletion of the lubricant [104].

SLIPS can be applied for potential marine and offshore applications on superstructures, radar systems, handrails, and windows (since SLIPS can be fabricated for optical transparency) [100]. SLIPS may not be applied on decks, stairs, work areas, or lower structures because of the unknown abrasive, corrosive performance [93,104] and its potential to cause slipping hazards.

2.3.3 The water film isolating technique

Some researchers argue that wettability is not a significant factor for ice protection. In contrast, the adhesion strength between the ice and the surfaces is the most critical parameter [105,106]. If the adhesion strength is very low, ice formed on these surfaces (not always hydrophobic; instead, some surfaces are hydrophilic) can be shed off by gravity, wind, or natural/mechanical vibrations. Therefore, Chen et al. [106] produced self-lubricating liquid water layer (SLWL) coated surfaces inspired by ice skating. When ice forms on these water film isolating surfaces, the ice can be blown away by the wind since the ice adhesion strength is reduced to 30.0 kPa. This result occurs because the water film has separated the ice and the substrates, which decreases the adhesion strength of the ice, similar to what occurs when ice skating [107,108].

The fabrication of SLWL coated surfaces is similar to the production of air isolating superhydrophobic surfaces or SLIPS. First, a pattern is produced on the top of the surface via mechanical or chemical methods. Then, an intermedia chemical (dipping, spraying, or grafted) is introduced to the base metal and the SLWL as a connection. For example, Chen et al. [106] used hygroscopic polymer; and Dou et al. Dou et al. (2014) coated polyurethane as the anti-icing layer, which is a hydrophobic core-hydrophilic corona coating. The hydrophobic core-hydrophilic corona coating can absorb the water from the moisture or melted ice overlaying it, forming the SLWL.

The anti-icing coating with water film isolation can be applied to substrates of different materials, for example, metals, metal alloys, ceramics, and polymers. It is also more competitive with other methods due to its excellent self-healing features in high humidity [106,108]. The SLWL can decrease ice adhesion strength by one order of magnitude compared with superhydrophobic surfaces. SLWL can also work well, even when the ambient temperature reaches -53 °C [108].

SLWL may be applied to offshore oil transmission pipelines, marine vessel superstructures, and vessel shells and structures close to water. This technique is unsuitable for stairs, work areas, and handrails due to potential slipping hazards. Areas on board with electrical and power transmission equipment must be avoided due to wet conditions, creating electric shock hazards.

2.3.4 The phase change material technique

A phase change material (PCM) absorbs heat and stores it in the form of latent heat. At a specific temperature range, the phase change occurs. The material can later release the stored heat to maintain the surface layer within a particular temperature range [109,110].

The applications of PCMs include thermal energy storage [110–112], waste heat recovery, thermal protection of electronic devices, batteries [90], and undersea pipelines [113]. It can potentially be applied for ice protection in cold regions [114–117]. For example, Duan and Naterer showed that a PCM layer could protect the ground layer in a power transmission line foundation in permafrost regions [118]. Cocu et al. found that n-tetradecane-type paraffin waxes with a solidification temperature of 2ºC or 5ºC can delay water freezing on tested pavement materials; however, the thermal effect is limited [114].

Phase-switching liquids (PSL) are PCMs in the liquid phase at room temperature with solidification points just above 0 °C (the icing point). The PSL stays in the solid phase away from the condensed droplets on supercooled surfaces but switches into the liquid phase in their immediate vicinity by absorbing the latent heat from condensation. Therefore, the icing nucleation process of the condensed water droplets can be delayed when they are in contact with the PSL on a supercooled substrate [117].

Table 2-6 The properties of PSLs [117], the table is adapted from a previously published paper by the author [21] with the permission of ASME International.

Materials	Abbreviation	Molecular Formula	Melting point (ºC)	Safety
Cyclohexane	SCh	C_6H_{12}	6.52	Flammable/ irritant/ health hazard/ environmental hazard
Cyclooctane	SCt	C_8H_{16}	14	Flammable/ health hazard
Anhydrous benzene	SB	C_6H_6	5.53	Flammable/ irritant/ health hazard
Tetradecane	ST	$C_{14}H_{30}$	5.86	Health hazard
Pentadecane	SP	$C_{15}H_{32}$	9.96	Health hazard
Hexadecane	SH	$C_{16}H_{34}$	18.19	Health hazard
Dimethyl sulfoxide	SD	$(CH_3)_2SO$	18.52	Explosion hazard/ irritant

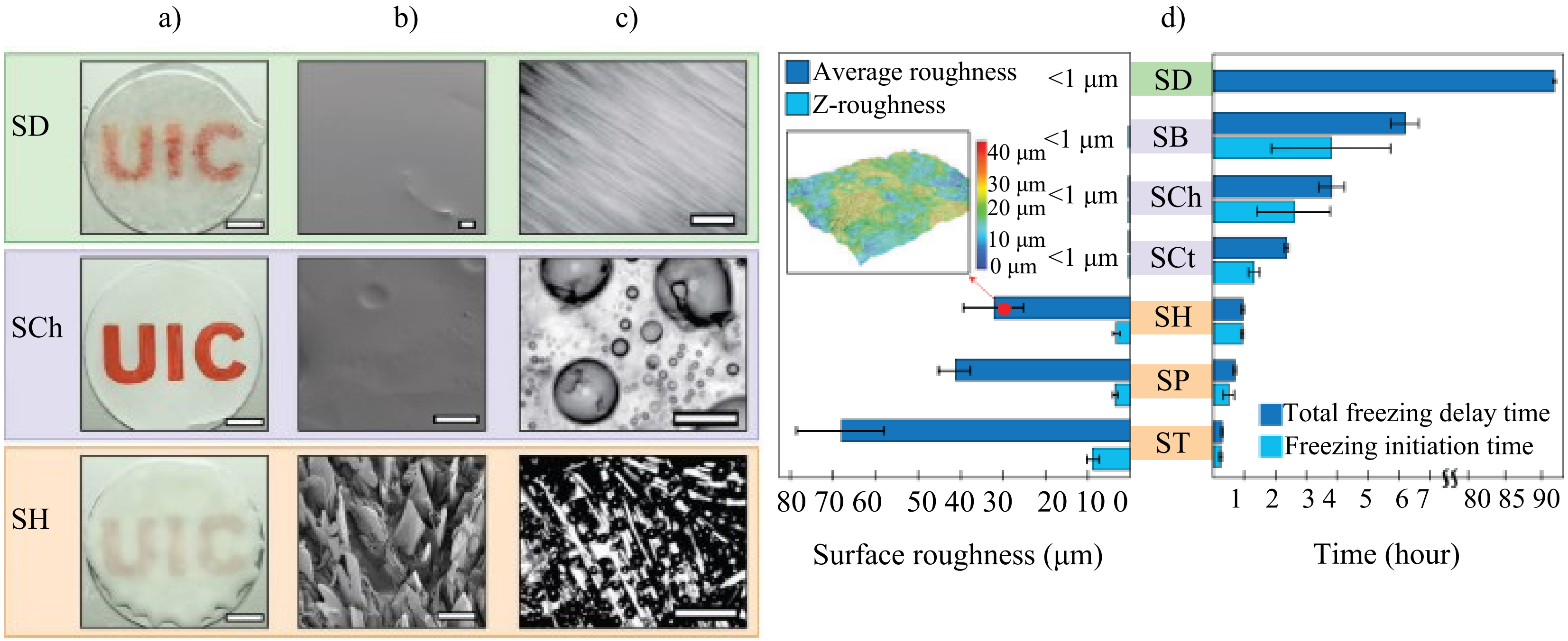

Figure 2-8 The key findings of Chatterjee et al. 2019: a) optical transparency of PSLs on aluminium surfaces (scale bar: 1 cm); b) SEM images at 45º (scale bar: 25 µm); c) optical microscopy images of typical condensation behaviour on corresponding bulk S-PSL (solidified PSL) surfaces at $T_{pel} = -15$ °C, RH = 80% (scale bars: 200 µm); d) S-PSL surface roughness (left, "Average roughness" is the arithmetic mean of absolute height shifts about the mean reference plane while "Z-roughness" denotes the distance between the highest peak and lowest valley on the surface) and condensation–frosting performance of various bulk S-PSLs (right) cooled to $T = -15$ °C in 80% RH environment. The figure is adapted from [117] with the permission of John Wiley and Sons – Books.

The first step in fabricating the PSL surface is to have a substrate roughened via mechanical or chemical methods to achieve a patterned structure and increase the adhesion strength between the PSL and the base materials. Second, the superfluous PSL spreads out to cover the textured surfaces completely. Then, the coated substrate is spun to remove excess liquid and achieve uniform impregnation, followed by a gravity-shed method to further remove excess liquid. [117]. Seven different PSLs have been listed in Table 2-6. These tests confirmed that the PSLs could significantly delay frost and ice formation on the target surface, as shown in Figure 2-8. Also, the PSLs are resilient to mechanical damage and can self-heal in nature [117]. Despite the excellent icing delay performance, some of the listed PSLs are unsafe to use. Most PSLs are flammable and will lead to environmental and health hazards. Also, durability is a problem under some circumstances; for example, the PSLs can be evaporated in warmer weather conditions. Further investigation is required to develop PSLs optimized for offshore and marine harsh environment applications.

2.3.5The photothermal techniques

The photothermal technique is a de-icing method that uses solar radiation or auxiliary illumination sources (LEDs or infrared lamps). As illustrated in Figure 2-9, a top absorber layer on the surface traps incoming sunlight and converts it to heat. A thin water film is then created from the melted ice at the interface. This water film is slippery; thus, the overlying ice can slide off from the substrate. The absorber can continue to trap light to maintain or increase the surface temperature, which can prevent ice accretion and improve anti-icing performance [119–122]. Solar energy is renewable and is usually considered a passive ice protection technique. Dash et al. (2018) investigated the "photothermal trap" by leveraging solar illumination to achieve icephobicity on a base substrate. Three layers are attached to the substrate, as shown in Figure 2-9. These three layers are the absorber (radiation absorption layer), the thermal spreader (heat dissipation layer), and the insulator (heat insulation layer). The absorber can trap the incident energy from artificial light or the sun, and then the local heat can transfer laterally through the spreader with a short response time. The insulator also helps minimize the heat dissipating to the corresponding substrate.

In some situations, these layers can either be bonded together and then attached to the targeted substrate surfaces or sprayed onto the target surfaces. Therefore, the photothermal technology can be integrated with existing offshore structures and allow remote de-icing and large-scale protection [120,121].

The photothermal materials absorb light irradiation to warm the surface above the freezing point. The melting of a thin layer of ice can significantly decrease the adhesion strength between the ice and substrate, and the rest of the ice cap can be removed by gravity or moderate wind power [108,121]. The techniques can be applied on antennas and radar, walkways, stairs, cranes, windlasses, valves, firefighting and rescue equipment, and air intakes. This technology can only be applied in areas exposed to direct sunlight or with additional illumination (LEDs or infrared lamps) [121]. The additional illumination can be more expensive than other active ice protection methods, such as direct heating. Ice can also form during the night or day with poor weather conditions. Further investigation is required to apply this method to offshore structures and marine vessels.

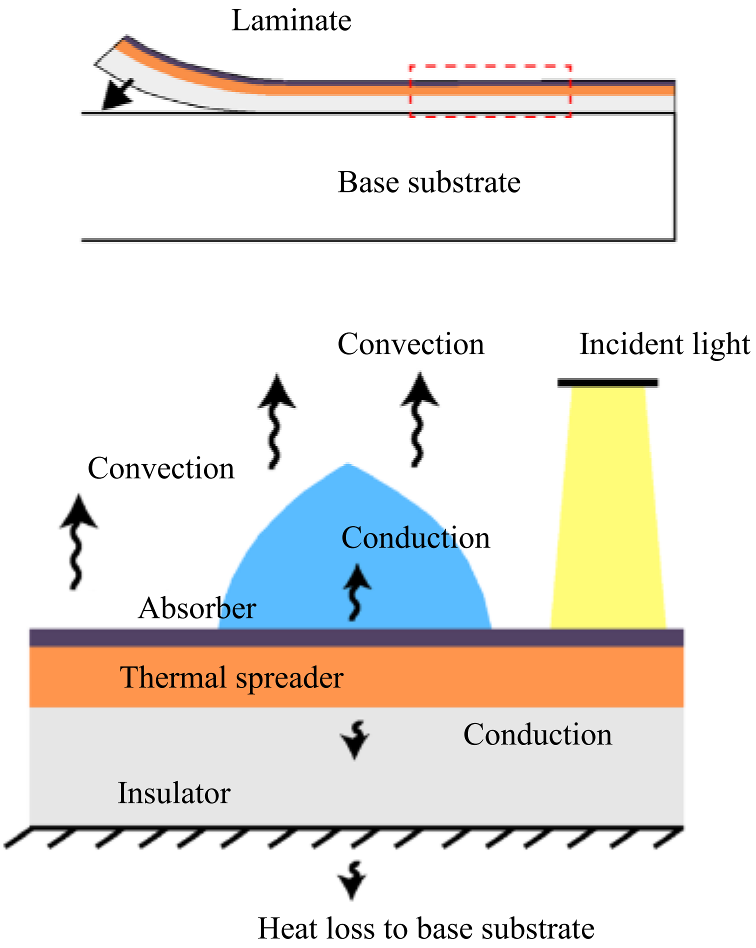

Figure 2-9 Schematic of the "photothermal trap" designed by Dash et al. 2018 and the heat transfer within incident light, overlaying ice cap, and the "photothermal trap." The figure is adapted from [121] with the permission of the American Association for the Advancement of Science.

2.3.6The low-interfacial toughness (LIT) material

The low-interfacial toughness (LIT) materials/coatings can eliminate the adhered ice on surfaces [123]. The testing results demonstrate that this technique is suitable for large area ice protection applications. An increase in surface area for the previously discussed surfaces with low ice adhesion strength will increase the external force required for de-icing. Therefore, the low adhesion strength surfaces may not suit de-icing applications for a large area. The external force required to remove ice on surfaces with low-interfacial toughness is minimal and independent of the surface area. LIT materials have been developed (LIT PS, LIT PVC, and LIT PDMS) with interfacial toughness of $5.9 \pm 1.0 \times 10^{-4}$ J/m^2, $1.2 \pm 0.04 \times 10^{-1}$ J/m^2, and $1.2 \pm 0.14 \times 10^{-4}$ J/m^2, respectively [123]. They found that there is a critical bonded length, L_c. When the accretion ice is longer than this critical bonded length, the force required for de-icing is constant and independent of the area of the interface. The bounded lengths for LIT materials (LIT PS, LIT PVC, and LIT PDMS) are 4.5 ± 2.8 cm, 4.3± 0.9 cm, and 6.7 ± 3.2 cm, respectively. Also, the lower thickness of the LIT coating leads to lower interfacial toughness between the ice and the coating [123]. These materials/coatings can be promising for offshore structure ice protection in large surface areas. They could be applied to superstructures, decks, ship hulls, walkways, stairs, cranes, windlasses, firefighting and rescue equipment, and air intakes. However, more efforts are required to evaluate the durability of these materials.

2.4 Approaches to fabricating air film isolating surfaces on different base materials

Table 2-7 Fabrication of surfaces by the top-down technique.

Method	Reference	Icephobic property	Droplet volume	θ_s (°)	θ_{sl} (°)	Substrate material
Wet chemical etching	[124]	Ice nucleation delay	5 µl	160	1	1045 steel
	[125]	-	4 µl	159.9/ 146.6	-	304/ 316 stainless steel
	[126]	-	-	158	-	Aluminium
	[127]	Ice nucleation delay	-	161.9	6.8	1060 Aluminum
	[128]	-	-	168	2	304 stainless steel
	[129]	-	-	167	3	2024 aluminium
	[130]	-	-	167.9	6.3	Aluminium
	[131]	-	-	170.5	~5	Aluminium
Dry etching	[132]	-	-	156.3	-	Glass
	[133]	Ice nucleation delay/ ice adhesion reduction	5 µl	169	-	Quartz
	[134]	-	-	165.7	-	Silicon
Laser irradiation	[135]	-	-	165	-	Titanium
	[136]	-	-	158	4	Platinum
	[137]	-	-	170	-	Polycarbonate based compounds
	[138]	-	-	155.8	-	1060 aluminium
	[139]	-	-	153	-	Ti-6Al-4 V titanium alloy
	[140]	-	-	152	-	14-4 PH stainless steel

Table 2-8 Fabrication of surfaces by the bottom-up technique. (IND: ice nucleation delay, IAR: ice adhesion reduction.)

Method	Reference	Icephobic property	Droplet volume	θ_s (°)	θ_{sl} (°)	Substrate material
Spray coating	[141]	-	-	155.5	1.5	Glass
	[142]	-	10 µl	171.4	5	Glass
	[143]	-	5 µl	155	-	Cotton fabric
	[144]	IND	5 µl	158	2	1045 steel
	[145]	IND/ IAR/ Anti-frosting	4 µl	155.3	-	Aluminium
Electro-spinning	[146]	Anti-forsting	-	148	-	(Membrane)
	[147]	-	10 µl	163	3	(Membrane)
Spin-coating	[148]	-	5 µl	158	2	Aluminium
	[149]	IND	4 µl	167	5	Glass
	[95]	IND / IAR	5/ 10 µl	153	14.3	Fe foil
	[150]	-	10 µl	~174	-	Glass
Dip-coating	[151]	-	1 µl	150	-	Glass
	[152]	IND	4 µl	153.3	6.5	Glass
	[153]	-	4~7 µl	174	4	Glass
Electro-depositing	[154]	-	5 µl	140	-	17-4 PH stainless steel
	[155]	-	8 µl	170	~0	Zinc
	[156]	-	6 µl	155.4	6.5	Graphite
	[157]	-	4 µl	158.4	2	AZ31 magnesium alloy

There are many approaches to fabricating air film isolating surfaces on different base materials. These base materials can be silicon [134], aluminum [126–131,138,145,148], steel [124,125,128,140,154], glass[132,133,141,142,149–153], titanium [135,158] and other materials [95,134,136,137,143,156,157,159]. Overall, there are three strategies for fabrication: top-down, i.e., top-down, bottom-up, and hybrid methods. Some of the most common top-down methods are listed in Table 2-7. These methods fabricate micro, nano, or micro-nano hierarchical structures by removing materials from the substrate through chemical etching, laser irradiation, and sandblasting. The bottom-up techniques are listed in Table 2-8. These techniques add a coating or generate micro, nano, or micro-nano hierarchical structures on the base materials through spray-coating, dip-coating, electrodeposition, electrospinning, and spin-coating electrodepositing. The hybrid approach combines the top-down and bottom-up methods in various ways.

2.5 Summary

More effective ice protection techniques are required for structures operating in harsh or Arctic marine environments. We evaluated most of the ice protection techniques that can be applied to offshore structures and vessels. These techniques have been divided into three categories: active techniques, passive techniques, and hybrid techniques. Active ice protection methods require extra energy supply, which demands extra space to install energy suppliers and is more expensive than passive methods in the long term.

At the same time, the passive ice protection techniques require no extra energy supply. Instead, they prevent or delay icing or reduce ice adhesion through surface icephobic properties. These technologies can significantly reduce operational costs. However, most passive techniques have limitations; for example, air isolating film surfaces are intolerant of high-humidity environments. Also, lubricants of oil isolating film surfaces, such as SLIPS, can be depleted after multiple freezing and melting cycles. The water film lubricating layer can be slippery and potentially create slipping hazards for individuals working on the surfaces. The application of phase change materials (PCMs) for offshore structures depends on the properties of the materials being used. PSLs can not be applied to marine facilities due to safety considerations. The newly proposed LIT materials/coatings are promising passive ice protection technologies; however, the durability of LIT materials requires further investigation. Regardless of these limitations, the low operational costs are more important from an engineering perspective. In this research, air isolating film surfaces will be used to analyze the water droplet impact and freezing process. A hybrid approach that combines the top-down and bottom-up techniques will be applied to fabricate the stainless steel samples and use them to analyze the droplet wetting behaviours, impact dynamics and freezing delay on these manufactured surfaces.

Chapter 3 Surface Fabrication and Characterization[3]

3.1 Introduction

In this study, two primary fabrication processes, which are mechanical machining and electrochemical coatings, will be applied since these techniques are commonly used in the industry for surface treatment. Section 0 demonstrates the sample preparation for this study. Section 3.2 shows the approaches for the characterization of the fabricated sample surfaces. Section 3.3 presents the summary of this chapter. Stainless steel sample preparation

3.1.1 Mechanical machining

Most studies have been conducted to develop regularly patterned superhydrophobic surfaces [90,140,160,161]. Although patterned surfaces with air gaps can effectively reduce direct contact with water [140,160–162], they are not easily produced on an industrial scale [163]. However, the sandblasting technique has been applied on large metal surfaces to increase the surface roughness, allowing air pockets between water droplets and surfaces. This technique is widely used in the industry for preparing metal surfaces before painting and is readily applied on a large scale

---

[3] The main content in this chapter is a part of a previously published paper (K. Shi, X. Duan, Freezing delay of water droplets on metallic hydrophobic surfaces in a cold environment, Appl. Therm. Eng. 216 (2022) 119131.) The author of this thesis is the first author of the published paper. The first author conducted an experimental study on the freezing delay of water droplets on metallic hydrophobic surfaces in a cold environment, identified the research topic, analyzed data, prepared the manuscripts and the corresponding revisions. Dr. Xili Duan, as the second author, provided his professional suggestions on this topic and assisted in preparing the manuscript and the corresponding revisions.

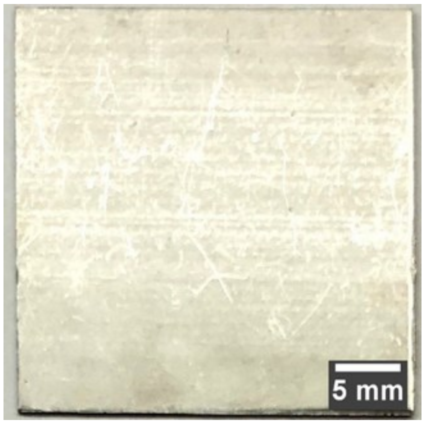

Figure 3-1 The image for a 30 × 30 × 0.8 mm stainless-steel tile.

The testing substrates are 30 × 30 × 0.8 mm stainless-steel tiles (SAE 630/17-4, McMaster-Carr), as shown in Figure 3-1. A micro-abrasive sandblaster (Problast-8008, Vaniman Manufacturing) is used for sandblasting treatment of the stainless-steel tiles, as shown in Figure 3-2. The sandblasting media is Al_2O_3 (White Fused Alumina, Vaniman Manufacturing) in two sizes, i.e., 100 µm and 250 µm.

Figure 3-2 Vaniman Problast-80008 micro-abrasive sandblaster

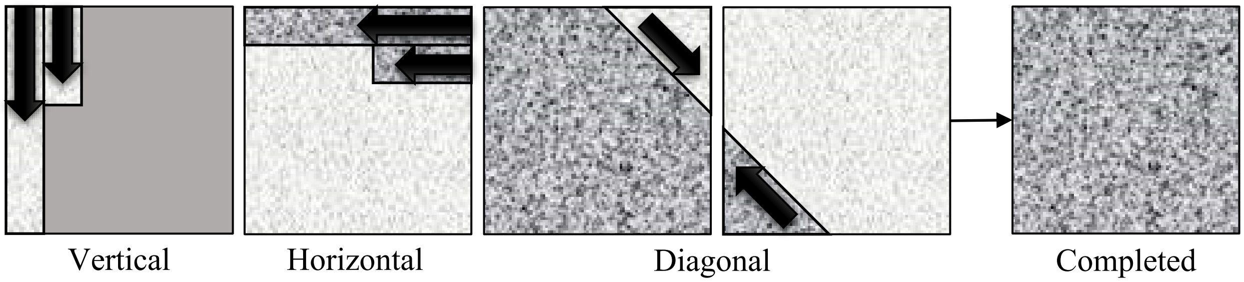

Figure 3-3 Representative the schematic of the sandblasting procedures.

Before sandblasting, all samples are cleaned by sonication in ethanol (95%, Commercial Alcohols, Inc.) and then placed into an ultrasonic cleaner with ultrapure water (Barnstead, 18.2 MΩ·cm) for 10 minutes independently. Ultrapure water is water that has been purified to uncommonly stringent specifications. Ultrapure water is a term commonly used in manufacturing to emphasize the fact that the water is treated to the highest levels of purity for all contaminant types, including organic and inorganic compounds; dissolved and particulate matter; volatile and non-volatile; reactive and inert; hydrophilic and hydrophobic; and dissolved gases. The ultrapure water used eliminates other factors or contaminants in the tape water that may influence the surface fabrication and experimental results. 18.2 MΩ·cm is the resistivity of the ultrapure water. In other words, the tendency of water without ions to resist conducting electricity. The unit of measure is the megohm · centimetre (MΩ · cm). It is generally used for high-purity water. The theoretical maximum is 18.2 MΩ · cm at 25°C. The higher the ionic content - the lower the resistivity, and the lower the ionic content - the higher the resistivity.

After the sonication, the samples are dried in the air at room temperature. During sandblasting, the blast pressure remained constant at 100 psi. At the same time, the nozzle tip was held approximately 1 cm from the target surfaces. Each sample was sandblasted, following the steps shown in Figure 3-3, to receive an optical uniform surface finish. After the sandblasting, all the samples were cleaned by sonication with the procedure described earlier and dried in air at room temperature. Figure 3-4 illustrates the optical images of the surfaces after sandblasting.

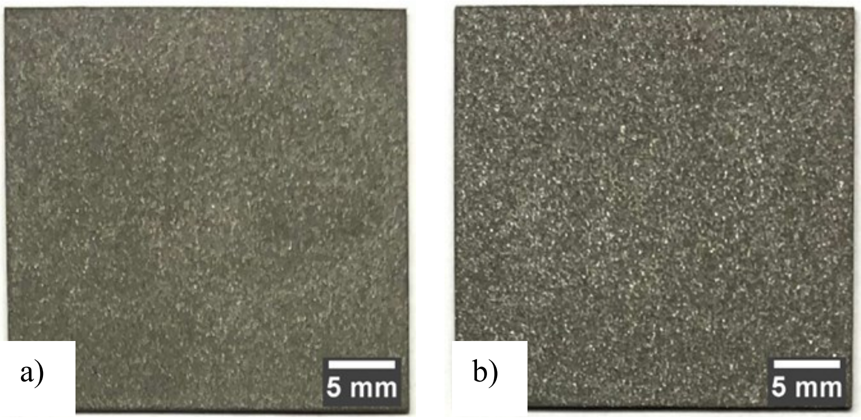

Figure 3-4 The optical images of sample surfaces after a) sandblasting with the 100 µm Al_2O_3 blasting media and b) sandblasting with the 250 µm Al_2O_3 blasting media.

3.1.2 Chemical coatings

In this stage, Zinc electrodeposited layer followed by stearic acid coating is used to decrease the surface energy and fabricate (super)hydrophobic surfaces. Figure 3-5 illustrates the experimental setup for the electrodeposition and the procedure to add the stearic acid coating.

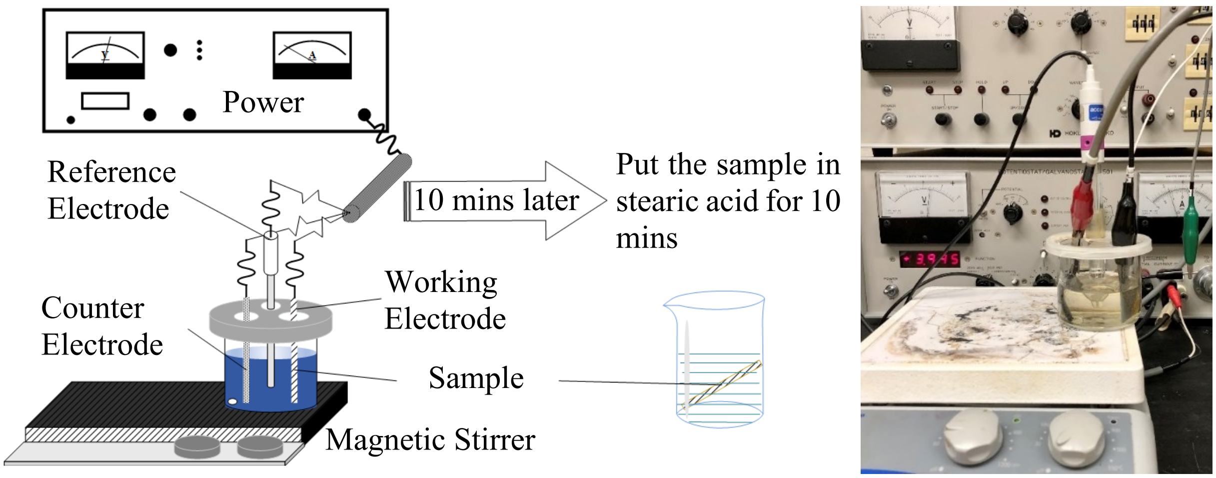

Figure 3-5 The experimental setup of electrodeposition.

Before the electrodeposition, two primary solutions are required. One is a 50 ml electrolyte solution of 1.56 g zinc chloride ($ZnCl_2$) (ACS grade, 97.0%, Caledon) and 9.27 g Ammonium Chloride (NH_4Cl) (ACS grade, 99.5%, ACP) in ultrapure water (Barnstead, 18.2 MΩ cm), and the other is a 45 ml ethanol-based solution (95%, Commercial Alcohols, Inc.) of 0.11 g stearic acid (95.0%, Sigma-Aldrich). The electrolyte pH is adjusted to 8.5 by adding NaOH (ACS grade, 97.0%, ACP) to the solution. After reaching the desired pH, 0.01 g polyethyleneimine (PEI, a variable mass polymer with a repeat unit mass of 42.03 amu) is added as a surfactant. The 3 cm × 3 cm working electrodes are cleaned by sonication in ethanol (15 min, 95%, Commercial Alcohols, Inc.), then in ultrapure water (15 min, 18.2 MΩ cm, Barnstead), dried in air at ambient temperature. The counter electrode is carbon felt (99.0%, Alfa Aesar). The deposition potential is reported relative to a saturated calomel (SCE) reference. Electrodeposition is carried out at constant potential (-1.50 V for non-sandblasted samples or −1.55 V for sandblasted samples vs. SCE) for 10 min at room temperature while stirring at 200 rpm.

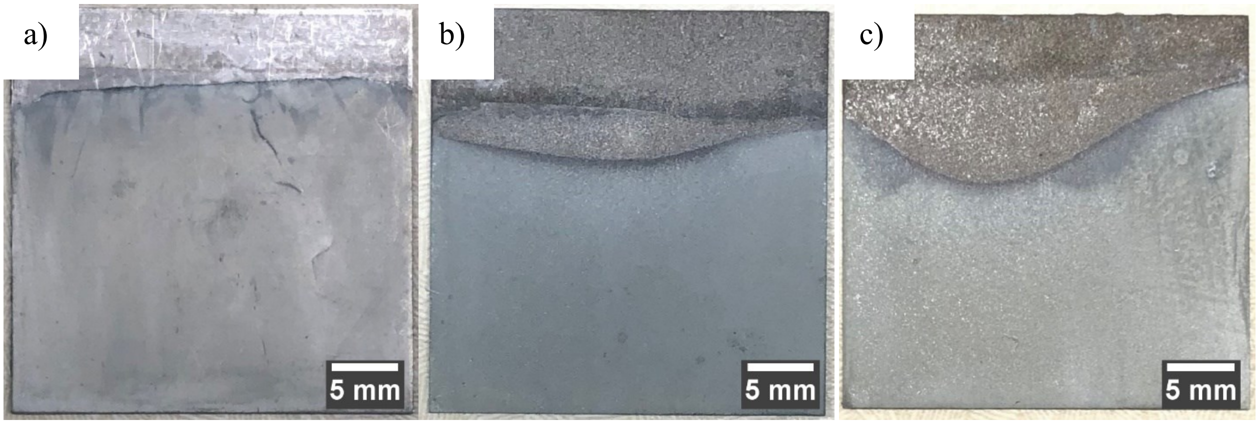

Figure 3-6 The optical images of sample surfaces after a) the original surface electrodeposited with zinc layer and coated with stearic acid, b) the surface with 100 μm Al_2O_3 sandblasting then electrodeposited with zinc and coated with stearic acid, c) the surface with 250 μm Al_2O_3 sandblasting then electrodeposited with zinc and coated with stearic acid.

After the deposition, the sample is rinsed with ethanol and immediately immersed in the ethanol-based solution of 0.11 g stearic acid (95.0%, Sigma-Aldrich) for 10 min, as shown in Figure 3-5. After that, the sample is finally rinsed with ethanol and air-dried before testing. Figure 3-6 illustrates the optical images for electrodeposited samples. As shown in Figure 3-6a, Figure 3-6b and Figure 3-6c, approximately 1/3 of each sample (on the upper side) is not electrodeposited since this part of the sample is used to connect the working electrode.

3.1.3 Summary

In summary, six samples (including the original, untreated sample) are fabricated by several fabrication methods, including sandblasting (S), Zinc electrodeposition (ED), stearic acid coating (SA), and their combinations are used to achieve different water wettability on the stainless-steel surfaces. Table 3-1 shows the samples and the corresponding surface preparation methods.

Table 3-1 Testing samples and fabrication methods

Sample Name	Preparation
ON	The original non-treated stainless-steel tile as the controlled sample
100S	Sandblasted with the 100 μm Al_2O_3 blasting media.
250S	Sandblasted with the 250 μm Al_2O_3 blasting media.
ED-SA	The non-treated stainless-steel tile with Zinc electrodeposition, followed by stearic acids coating and other steps described below.
100S-ED-SA	Sandblasting pre-treatment with the 100 μm Al_2O_3 blasting media, then electrodeposition with Zinc, followed by stearic acids coating and other steps described below.
250S-ED-SA	Sandblasting pre-treatment with the 250 μm Al_2O_3 blasting media, then electrodeposition with Zinc, followed by stearic acids coating and other steps described below.

3.2 Surface characterization

3.2.1 Scanning electron micrograph

The scanning electron microscope (SEM, model FEI MLA 650F, using secondary electron imaging (SEI)) is used to examine the surface topology of all sample surfaces. The scanning electron micrographs are illustrated in Figure 3-7. Features on all sandblasted surfaces are irregular, as expected due to the sandblasting pre-treatment. A comparison of Figure 3-7a and Figure 3-7b indicates that some needle-like zinc is attached to the coated surface, which may increase the surface roughness. The coated surfaces (Figure 3-7c and Figure 3-7d) have more round surface features than surfaces with no coating but have undergone the same blasting process (Figure 3-7e and Figure 3-7f). It is not possible to assess the height of surface features based on greyscale differences in these SEM images since the contrast is not based on height but rather on the number of secondary electrons collected at the detector.

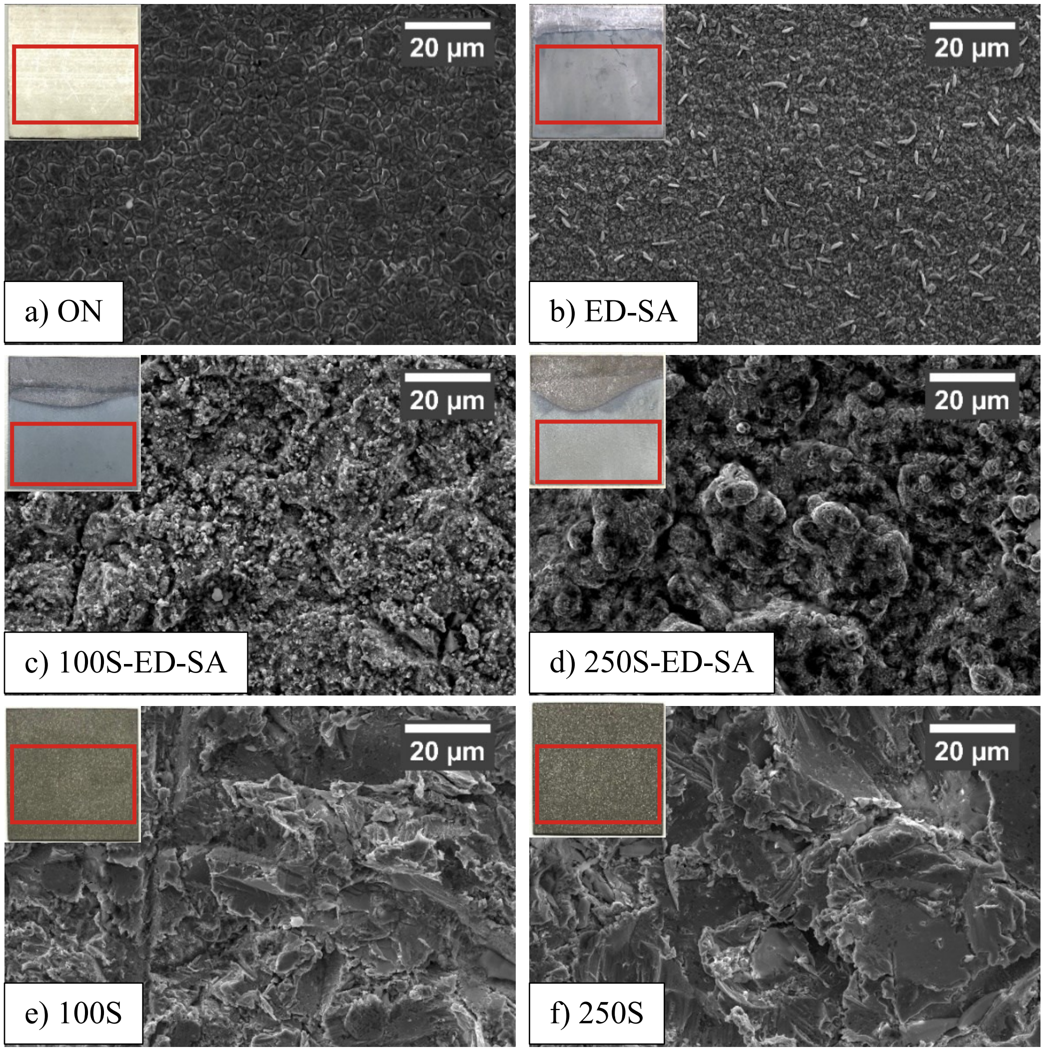

Figure 3-7 Scanning electron micrographs of the stainless steel sample surfaces: a) ON, b) ED-SA, c) 100S-ED-SA, d) 250S-ED-SA, e) 100S, f) s250S. (The scale bar is only applicable to the SEM images). The inserted images on the top left corner are optical images of the surfaces. The locations for SEM images are randomly selected in the red box (area of study) from the sample surfaces.

Other instruments well-suited to assessing surface roughness (such as a profilometer or atomic force microscope) are inappropriate for these samples because their mechanical probes cannot track intricate surface topography, such as undercuts and steep features. The lateral scale of the surface features shown in Figure 3-7 (~10–100 μm) is significantly smaller than a typical drop diameter in the experiments (D_i = 3.26 ± 0.41 mm), which presents in Chapter 5.

3.2.2 Surface wettability

A contact angle measuring system (OCA 15EC, DataPhysics), as shown in Figure 3-8, is used to characterize the static and dynamic contact angles for droplets of ultrapure water (Barnstead, 18.2 MΩ· cm). The measurement system consists of a backlit, an adjustable staging area, a software-controlled liquid dosing system, and a camera (USB-Wide-VGA camera, maximum resolution 752 × 480 pixels, 6× optical magnification, distortion is smaller than 0.05%, maximum sampling rate 15 fps). The syringe-based dosing system used a BD PrecisionGlide 26 G × 1/2 hypodermic needle (diameter = 0.45 cm).

Table 3-2 Measured water wettability on the testing samples

Name	θ_s (°)	θ_a (°)	θ_r (°)	CAH (°)
ON	91 ± 6	100 ± 5	61 ± 5	39.35
100S	108 ± 15	102 ± 5	58 ± 5	44.20
250S	106 ± 6	106 ± 6	68 ± 5	37.98
ED-SA	147 ± 2	157 ± 2	118 ± 5	38.99
100S-ED-SA	151 ± 2	156 ± 4	125 ± 3	31.17
250S-ED-SA	149 ± 4	157 ± 6	120 ± 9	36.96

Each measurement placed a water droplet with the same volume (20 μl) at a random location in the red box on the target sample surfaces, as shown in Figure 3-9. The "plynom fitting" method was used in the static contact angle measurement because this method is proven effective for the asymmetrical water droplet on irregularly roughened stainless-steel surfaces.

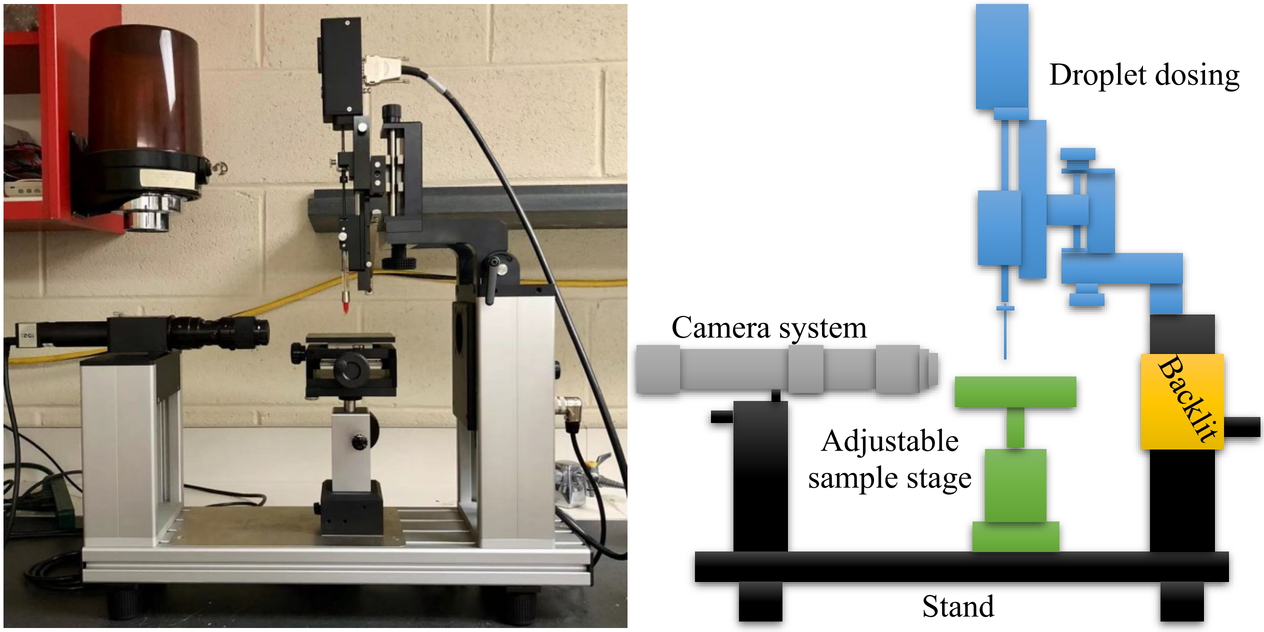

Figure 3-8 Dataphysics OCA 15EC contact angle measurement system, including a backlit, an adjustable staging area, a software-controlled liquid dosing system, and a camera.

The dynamic contact angle is required to determine the contact angle hysteresis (CAH). The advancing contact angle (θ_a) and receding contact angle (θ_r) are measured using the volume change method, which means adding and removing liquid to and from a sessile droplet on a horizontal surface. The *SCA 20* software is configured to add liquid to and then remove liquid from the droplet within a specified time interval. Throughout the process, the software automatically tracks and records the changes in contact angles as the droplet volume increases and decreases. The syringe is moved downwards until the needle tip is approximately 1 to 2 mm from the sample surface, and a 10 µl droplet is dispensed over the surface to measure θ_a and θ_r. While the needle was still in the water droplet, adjusting the needle to the middle of the droplet, then 10 μl of water is added at a rate of 2 μl/s to obtain θ_a. After several seconds, the 10 μl of water is removed at a rate of 2 μl/s to obtain θr. CAH is calculated as the difference between θ_a and θ_r. Static and dynamic contact angles are measured at five positions on each sample. The results are averaged to account for any surface structure or composition irregularities and are represented in Table 3-2.

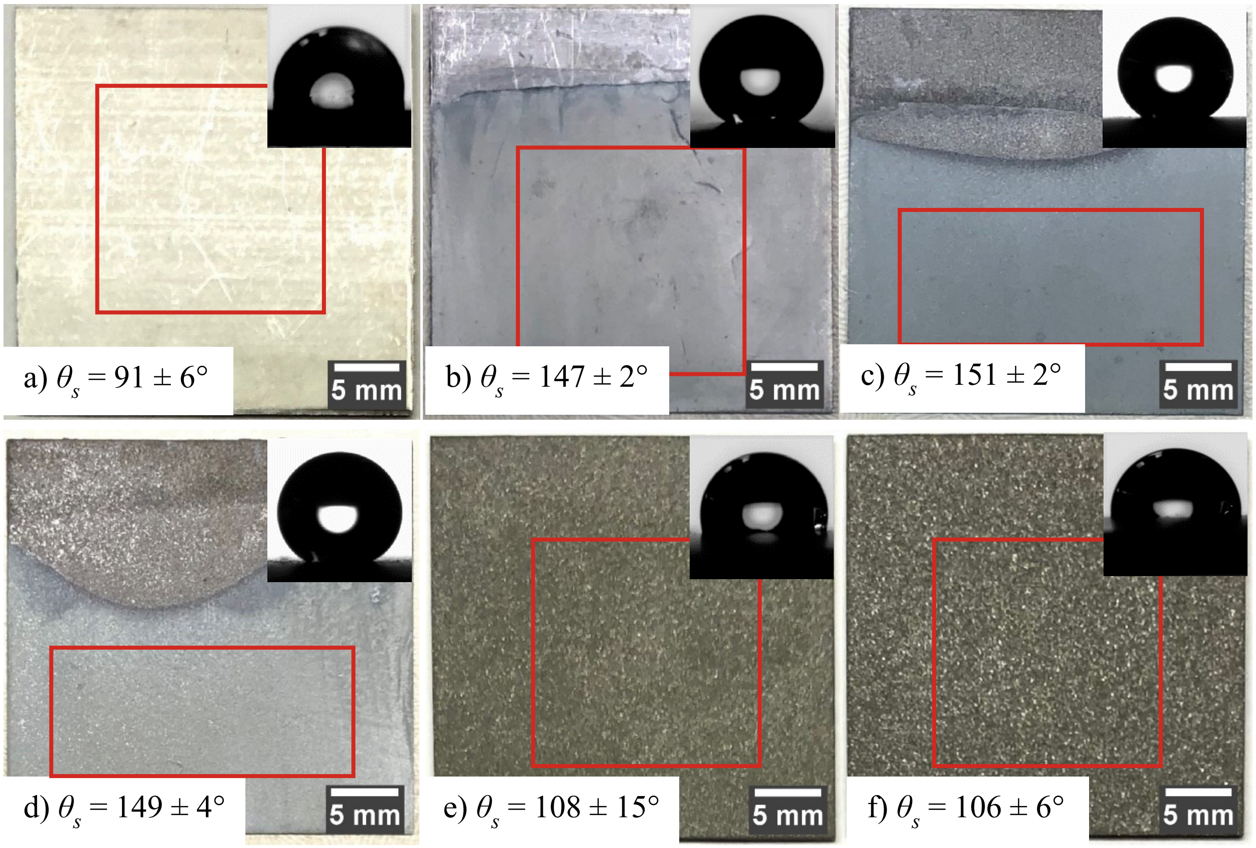

Figure 3-9 The contact angle measurements of a 20 μl sessile water droplet (on the top right corner) placed at a random location in the red box on a) ON, b) ED-SA, c) 100S-ED-SA, d) 250S-ED-SA, e) 100S, f) 250S. (The scale bar only applies to sample surface images, not the droplets). The static contact angle (average values with uncertainty) for each sample is provided at the bottom left corner of each picture.

3.3 Summary

The material and size of the samples used for experiments are 30 × 30 × 0.8 mm stainless-steel tiles. The fabrication process includes sandblasting, Zinc electrodeposition, stearic acid coating, and their combinations, which are used to achieve different water wettability on the stainless-steel surfaces. The static and dynamic contact angles of water droplets in contact with all samples are characterized using the contact angle measuring system (OCA 15EC, DataPhysics). The scanning electron microscope (SEM, model FEI MLA 650F, using secondary electron imaging (SEI)) is used to examine the surface topology of all sample surfaces. However, the other instruments suitable for evaluating surface roughness (for example, profilometers or AFM) are not suitable for these samples as their mechanical probes cannot track complex surface topography features such as grooves and steepness.

The combination of electrodeposition and sandblasting significantly increases the static contact angle, from 91 ± 6° (ON) to 151 ± 2 (100S-ED-SA), and both techniques can be used on an industrial scale. Before investigating the droplet impact dynamics and freezing delay, the dynamic wetting behaviours on the irregularly roughened metal surface should first be investigated. The methodology and outcomes can be found in the following Chapter 4.

Chapter 4 Dynamic Wetting of Irregularly Roughened Surfaces[4]

4.1 Introduction

Unlike intentionally patterned surfaces, sandblasting produces surfaces with irregular roughness, which has not been studied as intensively in the literature [164]. However, investigations of the static contact angles on irregularly roughed silicon surfaces show that the Wenzel (fully wetting) and Cassie-Baxter (partial wetting) models do not explain static contact angles on irregularly roughened surfaces [165,166]. In this chapter, the experimental study identified difficulties in quantifying dynamic wetting behaviour, demonstrating that static contact angles alone are insufficient to characterize randomly roughened surfaces and that sliding angles and contact angle hysteresis data are needed [167].

The experiments emphasize that standard metrics for dynamic wetting behaviour are insufficient to study water on surfaces with irregular roughness. To do this, the experiments report details of droplet shape variations on coated sandblasted steel, based on varying the incline angle of the surface on which the drop sits. In doing so, the results identify droplet pinning and depinning events. The following analysis explains why this leads to significant inherent complications in the

---

[4] The main content of this chapter is a part of a previously published paper (K. Shi, J. Elms, X. Duan, K.M. Poduska, Droplet asymmetry and wetting dynamics on irregularly roughened surfaces, J. Coatings Technol. Res. 18 (2021) 911–919.) The author of this thesis is the first author of the published paper. The first author measured the dynamic wetting behaviour of water droplets on the target surfaces using the sliding droplet method, identified the research topic, analyzed the corresponding data,prepared the manuscripts and the corresponding revisions. As the second author, Justin Elms measured the dynamic wetting behaviour of water droplets on the target surfaces by volume change method, identifying the research topic and analyzing the corresponding data. However, the part of research conducted by the second author is not included in this thesis. Dr. Xili Duan and Dr. Kristin M. Poduska, the third and fourth author, provided their professional suggestions on this topic and assisted in preparing the manuscript and the corresponding revisions.

measure of dynamic wetting behaviour on irregularly roughened surfaces. Section 4.2 presents the methodology of this experimental study. Section 4.3 shows the characterization of the fabricated sample surfaces. Section 4.4 demonstrates the results and discussion of this droplet dynamic wetting experiment. Section 4.5 presents the main conclusion from this chapter.

4.2 Dynamic contact angle measurements

A contact angle measuring system (OCA 15EC, DataPhysics) in Figure 4-1 was used to characterize dynamic contact angles for droplets of ultrapure water (Barnstead, 18.2 MΩ cm). The measurement system consisted of a backlit staging area, a syringe liquid dosing system, and a camera with 6× optical magnification. The camera is a USB-Wide-VGA camera integrated with Dataphysiscs OCA 15EC. The maximum resolution is 752×480 pixels. The image distortion is smaller than 0.05%. The sample rate is 15 fps.

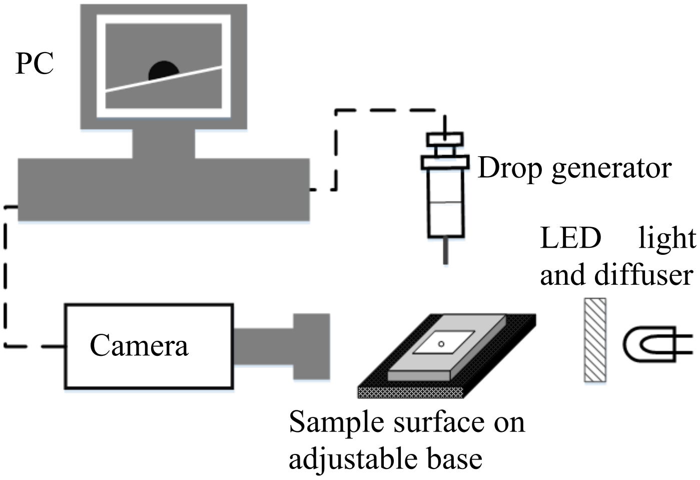

Figure 4-1 Schematic diagram of the dynamic contact angle measurement setup.

This study measures dynamic contact angles using the sliding method, as shown in Figure 4-2. The surface was tilted until the droplet began to slide (θ_t), at which point the advancing (θ_a) and receding (θ_r) contact angles were measured.

The substrates were cleaned with deionized water for 10 minutes and dried prior to affixing them to the tilted base. A certain volume of water (typically 20 µL) was placed on the substrate. The camera tracked the shape and position change of the droplet (20 µL) as the substrate incline angle was gradually increased from 0 degrees (level) to the sliding point ($\theta_{t,\,c}$, critical tilt angle).

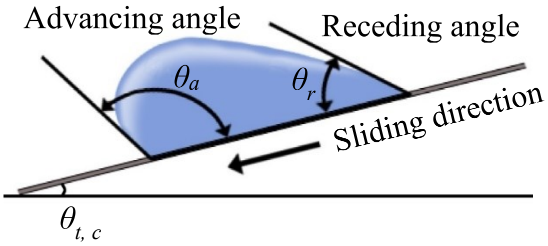

Figure 4-2 Schematic diagrams of the sliding method to measure dynamic contact angles

4.3 Surface characterization

Figure 3-7c, Figure 3-7d, Figure 3-7e, and Figure 3-7f show the representative SEM images of the sample surfaces used for dynamic contact angle measurements. These images are for substrates used for sliding experiments (100S-ED-SA, 250S-ED-SA, 100S, 250S). Features on all surfaces are very irregular, as expected, due to the sandblasting pre-treatment. The coated surfaces (Figure 3-7c and Figure 3-7d) appear to have more rounded surface features than the as-blasted substrates (Figure 3-7e and Figure 3-7f). It is impossible to assess the height of surface features based on grayscale differences in these SEM images since the contrast is not based on height but rather on the number of secondary electrons collected at the detector. The other instruments well-suited to assessing surface roughness (such as a profilometer or atomic force microscope) are inappropriate for these samples because their mechanical probes cannot track intricate surface topography, such as undercuts and steep features. The lateral scale of the surface features shown in Figure 3-7 (~10–100 μm) is significantly smaller than a typical drop diameter in the experiments (~2 mm).

Furthermore, our droplet diameters are less than the maximum capillary length for water under our experimental conditions. To calculate this, we used gravitational acceleration (9.8 m/s^2) and a temperature of 20 °C to give a water density ρ = 998 kg/m^3. Taking the surface tension of water to be 72.8 × 10^{-3} N/m, we find a maximum capillary length $\lambda_c = \sqrt{}\gamma/(\rho g)$ = 2.7 mm.

4.4 Results and discussion

By comparing our sliding data to a commonly used (Furmidge) model [168], this simple model is insufficient to explain the data.

First, Figure 4-3 shows how gravitational effects influence a tilted droplet. As the substrate tilt angle increases, the component of gravity along the surface direction (g·sin(θ_t)) increases. However, the component of gravity normal to the surface (g·cos(θ_t)) decreases. When the droplet pins, the decreasing normal gravity component (g·cos(θ_t)) causes a contact angle decrease on both the leading and trailing parts of the droplet (from θ_1 to θ_0) in Figure 4-3), while the along-surface component (g·sin(θ_t)) causes a contact angle to increase along the leading edge (θ_{led} increasing) and decrease along the trailing edge (θ_{tra} decreasing).

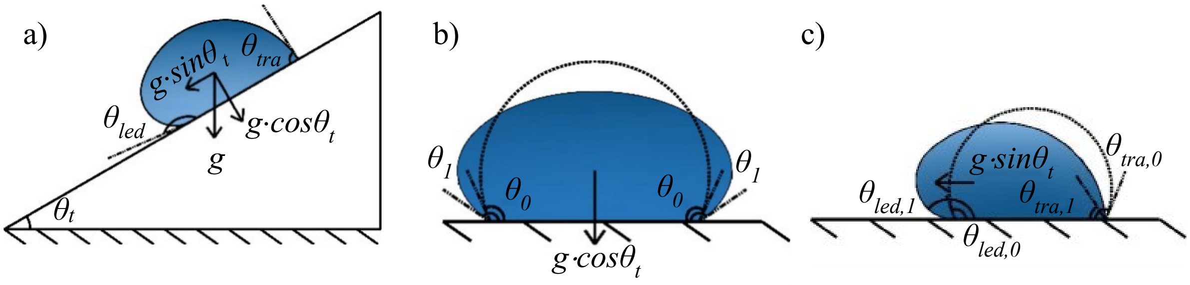

Figure 4-3 Schematic of the effect of gravity on water droplet shape while on an inclined surface. a) illustrates the actual, anisotropic droplet shape. b) shows the impact of the component of gravity normal to the surface, where θ_0 is the original contact angle of the drop and θ_1 is the contact angle after drop deformation due to the component of gravity g·cos(θ_t) increasing. c) represents the effect of the component of gravity along with the surface direction g·sin(θ_t), where and $\theta_{led,0}$ and $\theta_{tra,0}$ are the original contact angles, while $\theta_{led,1}$ and $\theta_{tra,1}$ are the contact angles at the leading and trailing edges after drop deformation.

This gravity-induced effect of pinning is visible in our data. Figure 4-4 shows how droplet contact angles change as the surface tilt angle increases. For example, the contact angle at the leading edge (θ_{led}) stays nearly constant as the substrate tilt angle (θ_t) is increased from 0 to 15°. However, the contact angle at the trailing edge (θ_{tra}) changes significantly. These trends are qualitatively explained in Figure 4-3, and they agree well with the findings of others [169].

There is another striking distinction between the trends we see in the advancing and receding contact angle data. The statistical uncertainties of the contact angles, as represented by the error bars on data points in Figure 4-4, are different: those for advancing contact angles are significantly larger (± 2.4°) than those for the receding contact angles (± 0.1°). These fluctuation differences are not an artefact of poor droplet image fitting parameters. Instead, they appear to result from inherent asymmetries in droplet pinning on these irregularly roughened surfaces.

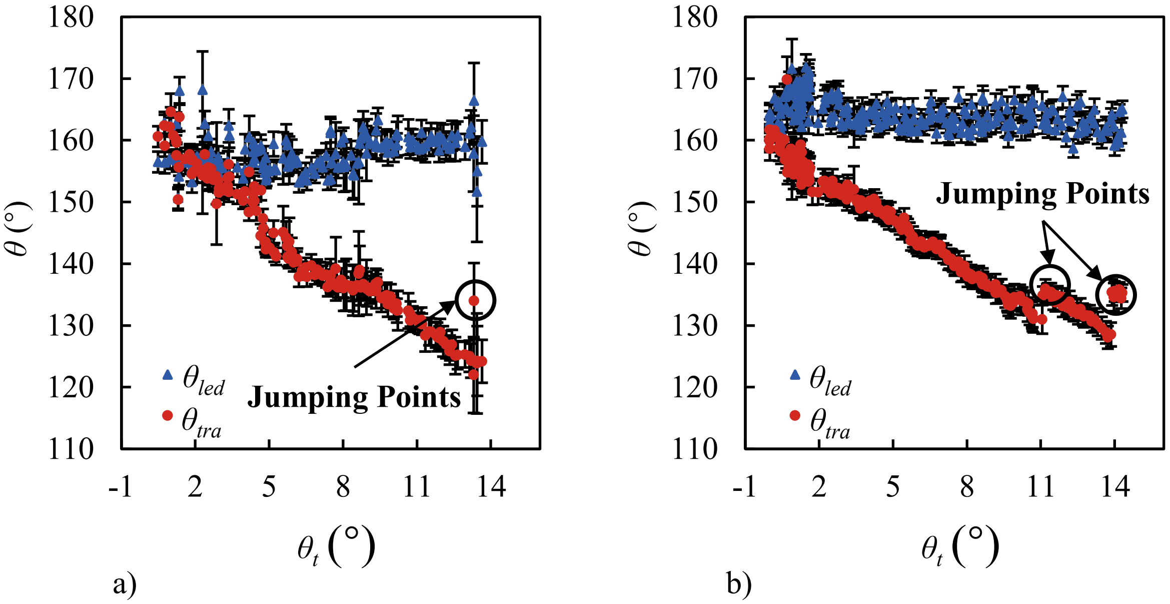

Figure 4-4 Representative contact angles at the leading edge (θ_{led}, red circles) and at the trailing edge (θ_{tra}, blue triangles) as a function of increasing substrate tilt angle (θ_t), shown here for (a) 250S-ED-SA and (b) 100S-ED-SA. Discontinuities in the contact angle trend are labelled as jumping points.

Going beyond the magnitude of contact angle fluctuations, several substrate tilt angles at which θ_{tra} changed rapidly between successive frames. These points are labelled “jumping points" and are circled in Figure 4-4. An image of the droplet at the first jumping point (Figure 4-4a) shows that part of the droplet depins but does not yet roll. To accommodate this depinning, the length of the base of the droplet decreases slightly (ΔD = 0.03 mm). We note that this distance ΔD is substantially more significant than the surface roughness scale (Figure 3-7c and Figure 3-7d) and that the uncertainty in all ΔD values is approximately 5%. An image of the droplet at the second jumping point (Figure 4-4b) corresponds to the incline angle at which the droplet begins to slide. In this case, the contact points between the surface and the droplet move on both ends of the droplet with similar magnitudes: the leading edge advances by ΔD_a = 0.05 mm, while the receding edge advances by ΔD_r = 0.06 mm.

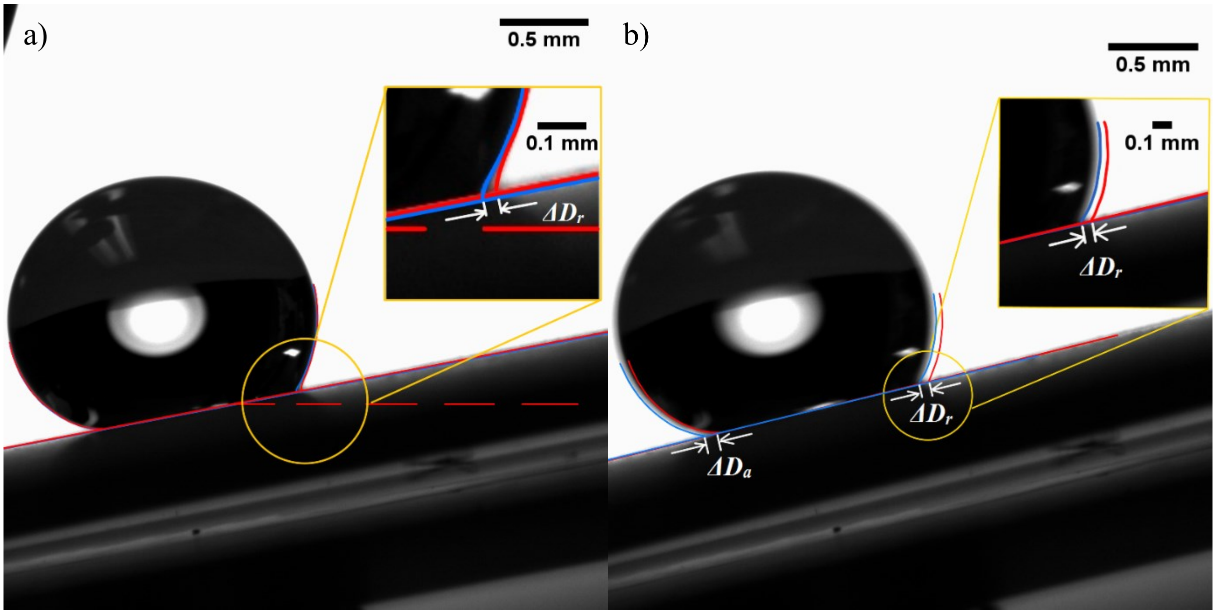

Figure 4-5 Representative examples of a droplet on an inclined surface with (a) partial depinning and (b) sliding that correspond to the discontinuities circled on the plot in Figure 4-4b.

For this experiment, a simple (Furmidge) model is applied [168] to demonstrate that the droplet pinning that occurs on the irregularly roughened surfaces introduces an additional asymmetry to droplets on inclined surfaces. Numerous studies have shown that droplet size, the degree of substrate wettability, adhesion between droplet and substrate, and surface roughness can affect the sliding behaviour of a water droplet [170–174]. In ideal cases, the sliding angle is proportional to the difference between the cosines of the dynamic advancing and receding contact angles, based on a simple relation introduced by Furmidge [168].

$$\frac{mg\sin\theta_{t,c}}{w} = \gamma_{LV}\left(\cos\theta_r - \cos\theta_a\right) \tag{4-1}$$

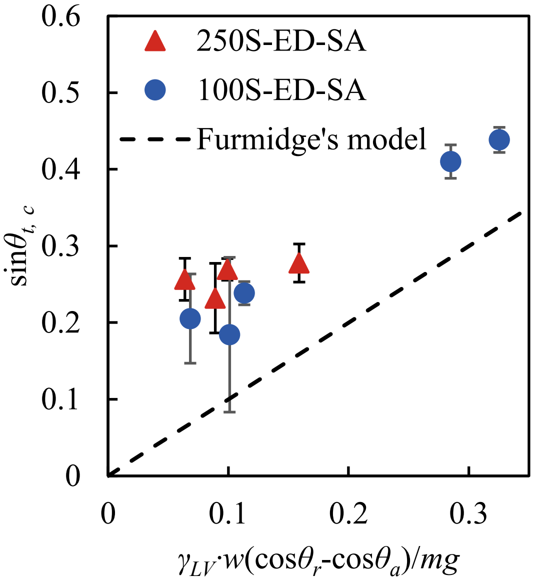

Figure 4-6 Critical tilt angles from experiments were plotted as a function of the predicted values from the Furmidge model, Eq. (4-1), for these two samples.

Here, $\theta_{t,\ c}$ is the critical tilt angle at which the droplet slides, m is the drop mass, g is the acceleration due to gravity, w is the drop width, γ_{LV} is the liquid-vapour surface tension, and θ_r and θ_a are the receding and advancing contact angles, respectively. The combined $mg\cdot\sin(\theta_{t,\,c})$ term is the gravitational force component that causes the drop to move.

Figure 4-6 shows poor agreement between the experimental data and the model. All experimental data shows a higher critical tilt angle than Eq. 5 would predict. There is no significant difference in the results between the two samples, even though they were roughened with different sizes of sandblasting media. Also, the experimental data are approximately parallel to the model.

Furmidge's model is based on the force balance. The along-surface gravity component contributes to the droplet moving, and the surface tension component prevents the droplet from moving. This model did not consider the drag induced by the roughened surface. The differences between the experimental data and the model indicate the other resistance components that prevent the droplet from moving, for example, the friction between the droplet and the roughened surface.

The Furmidge model is straightforward and does not account for any effects due to surface roughness. It is widely known that surface roughness can introduce air pockets in features that are too small for water to wet completely. More nuanced models for the dynamic wettability of a water droplet on the roughened surface do exist. One combines the concept of partial surface wetting due to air pockets (Cassie-Baxter wetting) with the Furmidge model [175]. Other models have been developed to explain the dynamic behaviour of droplets, including sliding/sliding angles and maximum droplet radius while sliding on either rough or smooth surfaces [17,176]. These studies show that surface roughness significantly affects the sliding angles on superhydrophobic surfaces. Even so, none of these models are appropriate if droplets are asymmetric.

Besides, many models correlate wettability with surface roughness [164]. However, surfaces vary depending on the length scale of the measurement area. Quantification of multi-scale roughness is described in the literature. It does not mesh well with wetting models, especially when pinning is the dominant effect (as it is in the case of our samples). This is because it is not clear in the field exactly what features and which length scales ultimately control pinning behaviour. It is particularly challenging on surfaces with irregular roughening where there can be features with high asperities that would not be apparent by using standard spatially averaged surface roughness values.

4.5 Summary

The dynamic contact angle data illustrate common problems inherent to the study of wetting dynamics on randomly roughened surfaces, which is a topic relevant for large-scale industrial applications of wetting that are important over the life cycle of a material.

For droplets on inclined versions of the same irregularly roughened surfaces, nearly all droplets adhered to these surfaces, even though contact angles were in the superhydrophobic regime (~150°). This result could not have been explained by the simple Furmidge model that relates sliding angles to volume-modified contact angles. These difficulties were not limited to the sandblasted and coated steel: the wetting behaviour of other roughened metals and plastics showed similar problems with pinning.

This dynamic wetting study does not propose a more complicated empirical model to fit the experimental data. Instead, the empirical models are not expected to be generalizable or to hold for surfaces with irregular rough features. Moving forward, this is suggested that future studies that involve contact angle assessments on surfaces adopt the following best practices:

(1) Report dynamic advancing and receding contact angles since apparent static contact angles alone are insufficient.

(2) Include images of the droplets and their fits to show how droplet asymmetry was addressed.

As in the present study shown in Section 3.2.2, future researchers can compare wettability studies in a more informed way by reporting these kinds of data together. These findings are relevant not only for metals but also could be applied to studies of other coated solid surfaces. However, the irregularly roughened substrate has not been investigated sufficiently, and the droplet impact dynamics and freezing process in subfreezing environments are not fully understood. Therefore, in the next Chapter, the droplet impact and freezing process on the irregularly roughened metal surface will be examined experimentally.

Chapter 5 Water Droplet Impact and Freezing Delay[5]

5.1 Introduction

Ice can form on a cold surface through two nucleation mechanisms: homogeneous or heterogeneous nucleation [177]. If the ice nucleation is triggered by foreign particles or an ice nucleus generated on an interface, it is named heterogeneous nucleation; otherwise, the ice nucleus is initiated by water molecules clustering, leading to homogeneous nucleation. The formation rate of an ice nucleus on a cold surface can be expressed as [178]:

$$J = K_c \exp\left(\frac{\Delta G^*}{k_B T_w}\right) \tag{5-1}$$

where K_c is the kinetic constant, ΔG^* is the critical Gibbs energy for nucleation, T_w is the surface temperature, and k_B is the Boltzmann constant. The rate is determined mainly by ΔG^*.

The energy barrier for homogeneous and heterogeneous nucleation can be expressed as Eq. (5-2) and (5-3), respectively.

$$\Delta G^*_{Homo} = \frac{16\pi\sigma^3}{3\Delta G_V^2} \tag{5-2}$$

$$\Delta G^*_{Hetero} = \frac{8\pi\sigma^3}{3\Delta G_V^2} f\left(\cos\theta, R\right) \tag{5-3}$$

---

[5] The main content in this chapter is a part of a previously published paper (K. Shi, X. Duan, Freezing delay of water droplets on metallic hydrophobic surfaces in a cold environment, Appl. Therm. Eng. 216 (2022) 119131.) The author of this thesis is the first author of the published paper. The first author conducted an experimental study on the freezing delay of water droplets on metallic hydrophobic surfaces in a cold environment, identified the research topic, analyzed data, prepared the manuscripts and the corresponding revisions. Dr. Xili Duan, as the second author, provided his professional suggestions on this topic and assisted in preparing the manuscript and the corresponding revisions.

where σ is the liquid /or ice-vapour surface energy, and ΔG_V is the Gibbs energy change per volume transformed between ice and water (J/m^3), θ is the contact angle of ice embryo in contact with the solid, f is the geometrical factor related to the contact angle and the contact surface roughness (R). The energy barrier for homogeneous nucleation is much higher than the heterogeneous one. The energy barrier of heterogeneous nucleation relates to the surface wettability and surface roughness of a solid phase (e.g., substrates and dust). The nucleation rate should be decreased to delay or prevent ice growth. The energy barrier of nucleation largely determines the rate. A better strategy is to increase the energy barrier by changing the surface wettability or surface roughness to decrease the heterogeneous nucleation, which can significantly delay ice nucleation.

A promising approach is developing superhydrophobic surfaces, which refer to surfaces with extremely low water wettability with a water static contact angle (CA) above 150° [6,7,49,51,179,180]. Besides, the dynamic (advancing and receding) contact angles and contact angle hysteresis (the difference between the advancing angle and the receding angle) are also important to establish the surface wettability, which involves liquid drops on a tilted surface or an increasing/decreasing droplet volume [181–183]. When a water droplet impacts a supercooled solid surface, its dynamics, heat transfer, and freezing process are all affected by the surface wettability and other factors such as the droplet impact velocity and the surface temperature.

Worthington [184] first investigated the dynamic spreading and splashing of a liquid droplet impact on a horizontal plate. The droplet impact process typically includes four stages: the kinematic phase, the spreading phase, the relaxation phase, and the equilibrium phase. Bahadur et al. [7] developed a predictive model of ice formation on superhydrophobic surfaces. They connected the droplet impact dynamics and heat transfer of ice formation in this model by applying Newton's second law of motion. However, this model did not consider other resistance forces during the dynamic process, such as the viscosity of the liquid, the friction of the impact surfaces, and air drag, which can affect the spreading motion [185].

Although there are some studies regarding the heat transfer between the water droplet and the target surface [186], the heat transfer between the water droplet and the (super)hydrophobic surface during the droplet impact and icing process has not been sufficiently investigated. The effects of contact area (between the liquid droplet and the surface) and surface wettability on the freezing delay on (super)hydrophobic surfaces are still unknown. Some previous studies were conducted at room or higher temperatures [187–189]. In this experiment, the freezing delay of water droplets on cold metallic surfaces was studied at a cold temperature below the freezing point of water. This experimental investigation fills an important gap in the existing literature. It aims to understand the effects of contact area and surface wettability on the freezing delay of water droplets on cold metallic surfaces. Six (super)hydrophobic stainless-steel surfaces are fabricated and examined for passive anti-icing, and the detailed sample preparation and characterization are presented in Chapter 3. Section 5.2 demonstrates the experimental setup for this experiment. Section 5.3 presents the uncertainty analysis. Section 5.4 shows the experimental results. Section 5.5 and section 5.6 presents the heat transfer analysis and dimensional analysis, respectively. Section 5.7 shows the durability of the fabricated sample surfaces. Section 5.8 presents the main conclusions from this experimental study.

5.2 Experimental setup

The setup for single water droplet freezing delay experiments is illustrated in Figure 5-1. A syringe pump with a needle (BD PrecisionGlide™ 26 G × 1/2 in Hypodermic Needles - 305111) generates water droplets of approximately 18.07 ± 0.51 μl. A thermocouple (Type K, Omega Engineering, Inc.) and a thermometer (FLUKE 52 II Thermometer) are used to monitor the initial temperature of the water droplets. A cold plate connected with a thermal bath is used to control the surface temperature of the samples. A high-speed camera (Phantom V611, Vision Research) records the dynamic and freezing process of the water droplet. A PC is connected to a high-speed camera for imaging capture and analysis. A LED light and a diffuser are used to provide light for imaging. The whole setup is placed in a cold room with an ambient temperature of -14.2 ± 2.4 °C to simulate a cold environment. The relative humidity in the cold room is between 80% and 86%, which is monitored by a hand-hold hygrometer (Velocicalc Plus, TSI).

The testing samples were placed in the cold room to decrease the surface temperature before an experiment. The syringe pump generates a water droplet of 18.07 ± 0.51 μl, and the distance between the needle of the syringe pump and a sample surface is 0 ± 0.05 cm (Sessile droplet, h = 0 cm), 4.88 ± 0.15 cm (h = 5 cm) and 9.90 ± 0.07 cm (h = 10 cm). The thermocouple is placed at the connection section between the needle and the syringe pump to monitor the initial temperature of a water droplet before it is released towards the testing surface. The thermal bath and cold plate control the testing surface temperature at -15.0 ± 0.1 °C. The high-speed camera records the whole dynamic and freezing process of the water droplet.

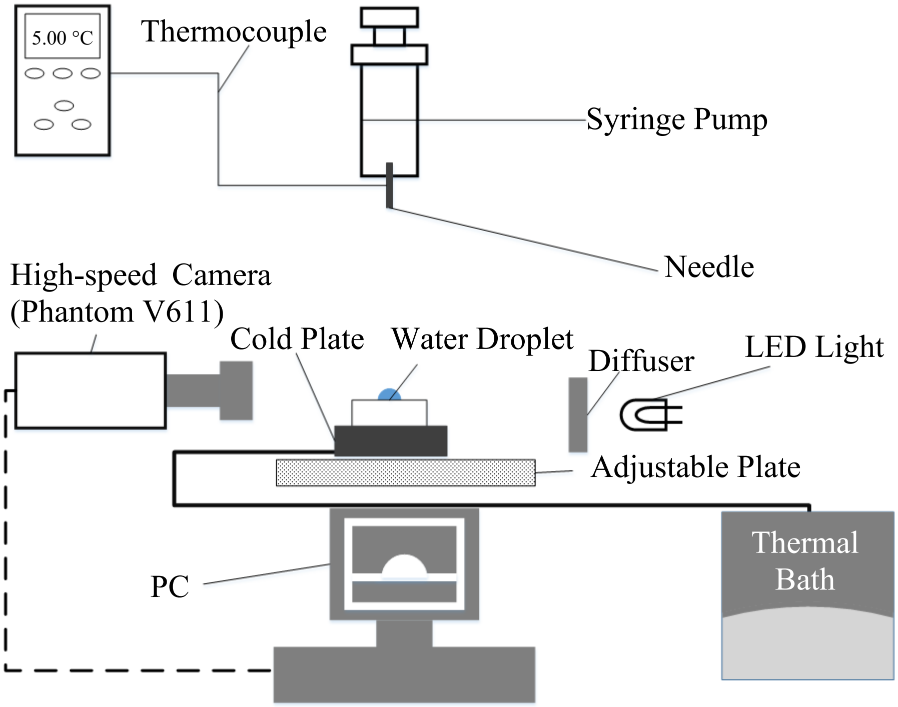

Figure 5-1 Schematic of the experimental setup.

5.3 Uncertainty analysis

The measured parameters include static contact angles θ_s, dynamic contact angles, i.e., advancing angle θ_a and receding angle θ_r, initial droplet diameter D_i, droplet final contact diameter on the surface D_c, icing delay time t, droplet falling distance h, the initial temperature of droplet T_i, the temperature of testing surface T_{sub}, the temperature in the cold room T_∞. The uncertainties of these measured parameters are listed in Table 5-1.

The method of Kline and McClintock [190] is used to determine the uncertainties of the calculated parameters in the heat transfer analysis in the following section. For any calculated parameter, the uncertainty, U_f, can be expressed as Eq. (5-4):

$$U_f = \sqrt{\left(\frac{\partial f}{\partial x_1}\right)^2 U_{x_1}^2 + \left(\frac{\partial f}{\partial x_2}\right)^2 U_{x_2}^2 + \left(\frac{\partial f}{\partial x_3}\right)^2 U_{x_3}^2 + \ldots} \tag{5-4}$$

Table 5-1 Uncertainties of measured parameters (± value)

Sessile drop (h = 0 cm)

Samples	**$U_{\theta s}$ (°)**	**$U_{\theta a}$ (°)**	**$U_{\theta r}$ (°)**	**U_{Dc} (mm)**	**U_t (s)**	**U_{Ti} (°C)**	**U_{Tsub} (°C)**	**$U_{T\infty}$ (°C)**
ON	6	5	5	0.05	4.92	0.30	2.01	0.29
ED-SA	2	2	5	0.14	2.82	0.15	2.02	0.28
100S-ED-SA	2	4	3	0.25	5.22	0.10	2.06	0.56
250S-ED-SA	4	6	9	0.08	2.89	0.13	2.07	0.52
100S	9	5	5	0.18	4.86	0.11	2.01	0.53
250S	6	6	5	0.05	3.30	0.17	2.01	0.76

h = 5 cm

Samples	**U_{Ai} (mm^2)**	**U_{Dc} (mm)**	**U_t (s)**	**U_{Ti} (°C)**	**U_{Tsub} (°C)**	**$U_{T\infty}$ (°C)**
ON	0.64	0.45	1.81	0.12	2.05	0.43
ED-SA	1.23	1.21	2.22	0.14	2.02	1.39
100S-ED-SA	1.13	0.74	1.18	0.17	2.02	1.51
250S-ED-SA	0.72	0.64	5.30	0.11	2.05	1.36
100S	0.70	0.25	1.31	0.11	2.02	1.07
250S	0.71	0.26	0.70	0.12	2.01	0.70

h = 10 cm

Samples	**U_{Ai} (mm^2)**	**U_{Dc} (mm)**	**U_t (s)**	**U_{Ti} (°C)**	**U_{Tsub} (°C)**	**$U_{T\infty}$ (°C)**
ON	0.28	0.17	1.07	0.08	2.00	0.37
ED-SA	0.80	0.44	2.01	0.13	2.04	0.23
100S-ED-SA	0.46	0.25	6.64	0.04	2.05	0.38
250S-ED-SA	0.27	0.15	2.80	0.08	2.02	0.56
100S	0.16	0.10	1.45	0.11	2.04	0.08
250S	0.45	0.12	2.26	0.18	2.02	0.34

Table 5-2 Uncertainties of calculated parameters (± value)

Sessile drop (*h* = 0 cm)

Samples	$U_{\bar{q}m} \times 10^{-4}$ **(W/kg)**	$U_{Ac,\,m}$ **(m^2/kg)**	$U_{t\,freezing,\,m} \times 10^{-6}$ **(s/kg)**
ON	0.11	0.03	0.29
ED-SA	0.12	0.05	0.20
100S-ED-SA	0.19	0.10	1.00
250S-ED-SA	0.07	0.03	0.18
100S	0.17	0.09	0.40
250S	0.09	0.03	0.24

***h* = 5 cm**

Samples	$U_{\bar{q}m} \times 10^{-4}$ **(W/kg)**	$U_{Ac,\,m}$ **(m^2/kg)**	$U_{t\,freezing,\,m} \times 10^{-6}$ **(s/kg)**	U_{t^*}	U_{Ac^*}	U_{We}	U_{Wei}
ON	0.30	0.27	0.10	17.96	0.31	1.53	2.61
ED-SA	0.32	0.39	0.25	22.49	0.38	2.80	2.92
100S-ED-SA	0.20	0.10	0.35	12.17	0.12	2.60	2.72
250S-ED-SA	0.19	0.15	0.33	53.71	0.11	1.71	1.79
100S	0.23	0.20	0.12	13.03	0.30	1.68	2.79
250S	0.20	0.22	0.11	7.02	0.31	1.68	2.61

***h* = 10 cm**

Samples	$U_{\bar{q}m} \times 10^{-4}$ **(W/kg)**	$U_{Ac,\,m}$ **(m^2/kg)**	$U_{t\,freezing,\,m} \times 10^{-6}$ **(s/kg)**	U_{t^*}	U_{Ac^*}	U_{We}	U_{Wei}
ON	0.49	0.21	0.08	7.48	0.34	1.58	2.61
ED-SA	0.67	0.38	0.23	14.16	0.66	4.39	2.92
100S-ED-SA	0.19	0.10	0.55	46.87	0.19	2.53	2.72
250S-ED-SA	0.29	0.05	0.45	19.76	0.10	1.56	1.79
100S	0.50	0.13	0.11	10.17	0.21	0.95	2.79
250S	0.77	0.29	0.18	15.83	0.42	2.52	2.61

where f is the calculated parameter as a function of the measured parameters x_1, x_2, x_3. Table 5-2 lists the uncertainties of the calculated parameters in the heat transfer analysis. Please see the more detailed uncertainty analysis in Appendix C, and all the uncertainties are illustrated with error bars in the figures.

5.4 Droplet impact dynamics and icing delay

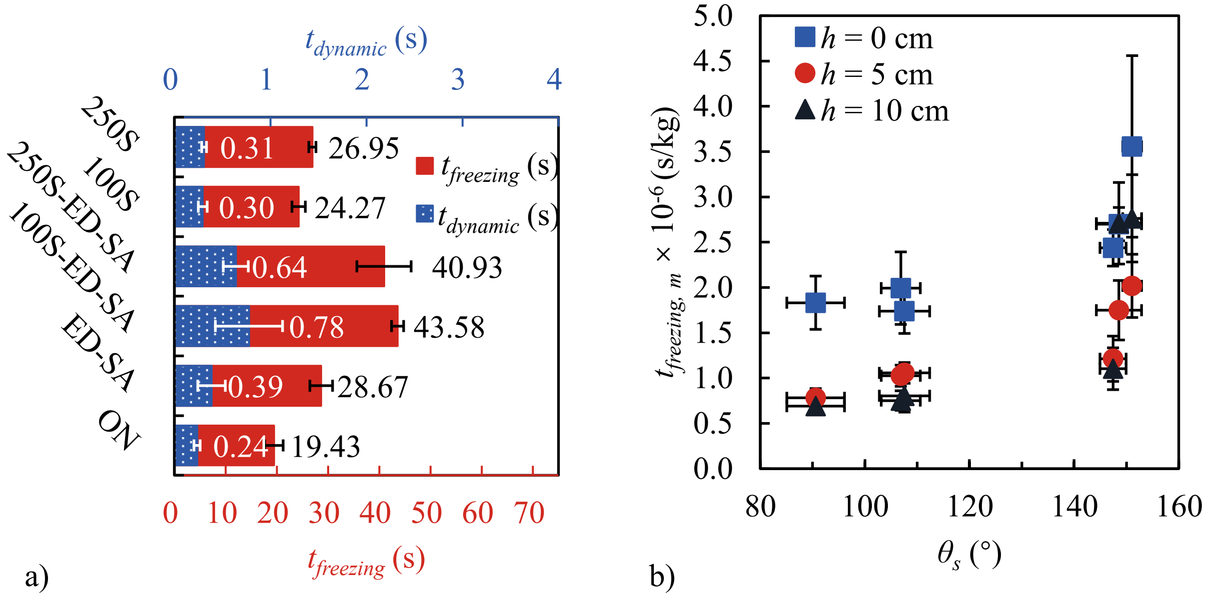

Figure 5-2 a) Representative total freezing delay time $t_{freezing}$ and droplet dynamic time $t_{dynamic}$ for a droplet impact on different surfaces, b) the relations between the static contact angle θ_s of water droplets on target surfaces and the total freezing time per unit mass $t_{freezing,\ m}$. (h is the droplet impact height, and h = 0 cm means sessile drops).

The total freezing delay time ($t_{freezing}$) is the time duration from the water droplet impacting the target surface to its complete freezing. It includes the droplet dynamic time ($t_{dynamic}$), from its initial contact with the surface to the final static state after the impact dynamics. In the experiments, these time instants are determined from the images recorded by the high-speed camera at a capture rate of 500 fps (frame per second). A reliable indicator of the complete freezing of the water droplet is the formation of a sharp tip [90,191,192] on the top, as shown in the last image of Figure 5-3. In this research, the freezing time ends when the high-speed camera captures the formation of this tip.

Figure 5-2a shows the total freezing delay and impact dynamic time of a water droplet on the six sample surfaces when the impact height is 4.88 ± 0.15 cm. The upper axis is for the dynamic time (in the blue, unit: s), while the bottom one is for the total freezing delay time (in the red, unit: s). The measured data indicates that the droplet dynamic time accounts for only approximately 1.15% to 1.56% of the total freezing delay time for all samples. Most of the time (>98% of the total freezing delay time), the droplets are stationary on the surfaces with a fixed contact area between the droplet and the surface. The same observation was reported in earlier studies[91]. Therefore, heat transfer during the droplet dynamic period is neglected in the heat transfer analysis of the freezing process in section 5.5.

In real applications and engineering problems, the droplet sizes would not be identical (for example, raindrops and sea spray droplets). The total freezing time per unit mass can be defined (Eq.(5-5)), with the total freezing time divided by the mass of each water droplet. The results can then be applied to more general scenarios.

$$t_{freezing,\,m} = \frac{t_{freezing}}{m_D} = \frac{t_{freezing}}{\rho V_D} \tag{5-5}$$

Figure 5-2b shows the relationship between the static contact angle θ_s of water droplets on the surfaces and the total freezing time per unit mass $t_{freezing,\,m}$. Overall, a higher static contact angle

θ_s contributes to a longer total freezing time per unit mass (with the same impact height). The 100S-ED-SA surface shows the longest freezing delay time among all the samples. When the impact height is 0 cm, 4.88 ± 0.15 cm and 9.90 ± 0.07 cm, the water droplet will completely freeze on sample 100S-ED-SA after $(4.64 \pm 1.00) \times 10^6$ s/kg, $(2.02 \pm 0.35) \times 10^6$ s/kg and $(2.92 \pm 0.56) \times 10^6$ s/kg, respectively. The freezing delay times of droplets on sample 250S-ED-SA are slightly shorter. However, the result indicates that the $t_{freezing,\ m}$ at $h = 10$ cm is larger than at $h = 5$ cm under superhydrophobic conditions. The reason is that when the impact height is 10 cm, the droplet will partially bounce off the superhydrophobic surface, and that part does not fall back into the original droplet. As a comparison, the droplet will not bounce off the surface at the impact height of 5 cm. As a result, the final contact area (A_c) of the droplet at $h = 10$ cm is smaller than the contact area at $h = 5$ cm (this will be shown in Figure 5-5a). Hence, the total freezing delay time per unit mass is greater at $h = 10$ cm than at $h = 5$ cm due to the reduced final contact area. Overall, the data suggest the best anti-freezing (longest freezing delay time) properties of surfaces with the lowest wettability (highest contact angles). Higher impact also leads to shorter freezing delay time. The shorter freezing time indicates higher freezing (heat transfer) rate, which can be explained by the increased contact area between the droplet and the surface, as will be further analyzed in the next section.

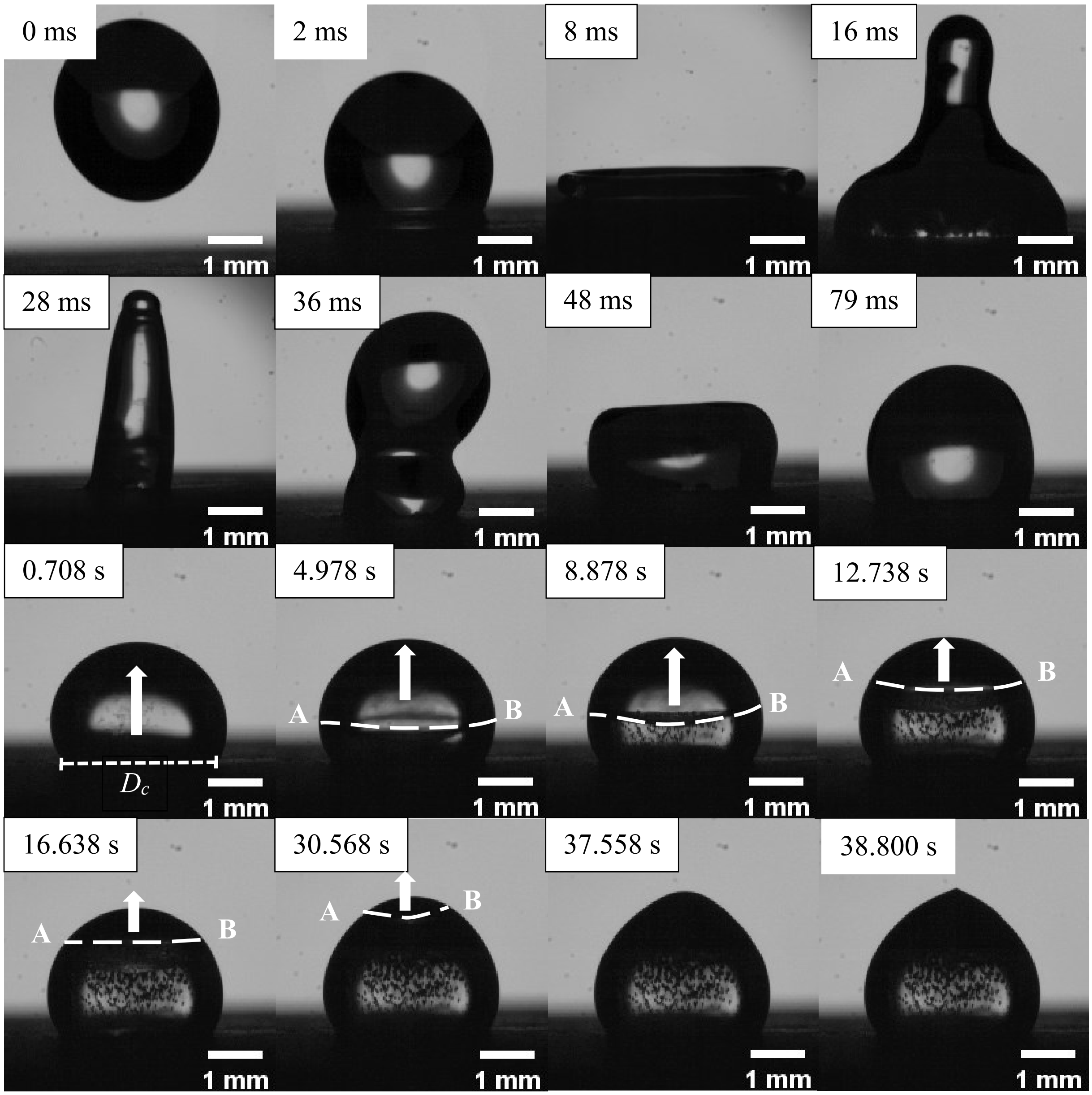

Figure 5-3 Representative process of a water droplet (D_i = 3.55 ± 0.07 mm, T_d = 5.04 ± 0.17 °C) impact on the 100S-ED-SA surface (T_{sub} = -14.86 ± 2.02 °C) in the cold environment (T_∞ = -12.55 ± 1.49 °C). (The scale bar is only applicable to Figure 5-3.)

Figure 5-3 illustrates a water droplet (D_i = 3.55 ± 0.07 mm, T_d = 5.04 ± 0.17 °C) impact on the 100S-ED-SA surface (T_{sub} = -14.86 ± 2.02 °C) in the cold room (T_∞ = -12.55 ± 1.49 °C). Upon impact on the surface, the droplet starts to expand and quickly reaches the maximum spreading diameter. The droplet does not bounce off from the surface in the retracting phase, while it can bounce off the surface at room temperature at the same impact velocity. This phenomenon suggests a competition between the droplet dynamics and heat transfer to the cold surface. Due to the lower temperature, the contact line may be partially frozen in the droplet dynamic process, and the droplet would not rebound but stay on the cold surface. This confirms that temperature can significantly affect the water droplet dynamics on superhydrophobic surfaces, which has been reported in the literature [179,193,194]. In about 0.78 s, the oscillation of the water droplet stops while it is still in the liquid phase. This observation confirms the existence of a fixed "contact area" for heat transfer analysis in the freezing process. After several seconds, a solid-liquid interface plane AB can be observed, which moves upwards from the droplet-surface contact plane to the top of the droplet. In the end, a tip is formed on the top of the cap-shaped water drop upon complete freezing, which agrees with findings from other studies [192].

5.5 Heat transfer analysis of the icing process

The target surface temperature was measured by an infrared thermometer (Rosewill, RTMT-11001) with an accuracy of ± 2°C. The initial droplet diameter D_i is 3.26 ± 0.41 mm, and and the impact speed is 0 m/s, 0.98 ± 0.01 m/s, and 1.39 ± 0.01 m/s. The initial temperatures of the water droplet and temperatures in the cold room are listed in Table 5-3.

The temperature difference between the cold room environment and the initial temperature of the droplet is significant. Therefore, convective heat transfer is considered for the droplet falling process. Figure 5-4a illustrates the heat transfer from a water droplet to the surrounding cold air. This analysis assumes spherical droplets, and the Nusselt number in Eq. (5-6) [195] is applied to the falling droplet.

$$\overline{Nu_D} = \frac{\overline{h_D} D_i}{k} = 2 + 0.6 Re_D^{\frac{1}{2}} Pr^{\frac{1}{3}} \tag{5-6}$$

where Re_D is the Reynolds number, Pr is the Prandtl number, $\overline{h_D}$ is the average convective heat transfer coefficient, D_i is the initial diameter of the water droplet, and k is the thermal conductivity of air.

The Reynolds number for the droplet can be expressed as follow:

$$Re_D = \frac{u D_i}{\upsilon} \tag{5-7}$$

where u is the air velocity, D_i is the initial diameter of the drop, and υ is the kinematic viscosity of air.

The average convective heat transfer coefficient $\overline{h_D}$ can be obtained from Eq. (5-8), and is calculated to be 12.6 ± 0.55 W/m^2·K, which is approximately the same for all the droplets.

$$\overline{h_D} = \frac{\overline{Nu_D} k}{D_i} = \frac{k(2 + 0.6 Re_D^{1/2} Pr^{1/3})}{D_i} \tag{5-8}$$

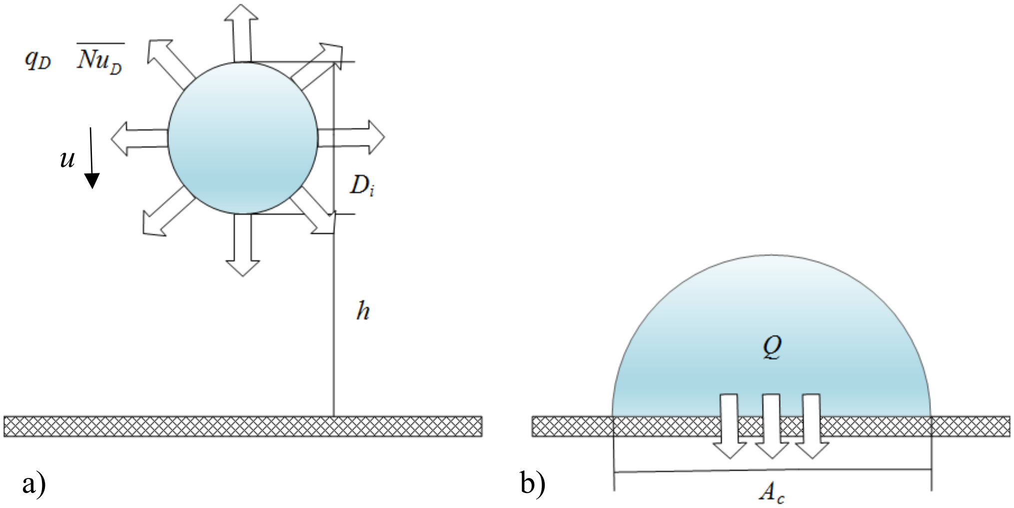

Figure 5-4 Schematic of heat transfer of the water droplet on the target surface

Table 5-3 The initial temperature T_i of the droplets and the temperature T_∞ of the cold room

Samples	**Sessile drop (*h* = 0 cm)**		***h* = 5 cm**		***h* = 10 cm**	
	T_i (°C)	**T_∞ (°C)**	**T_i (°C)**	**T_∞ (°C)**	**T_i (°C)**	**T_∞ (°C)**
ON	4.75 ± 0.30	-16.42 ± 0.29	5.12 ± 0.06	-11.26 ± 0.37	4.98 ± 0.08	-16.20 ± 0.37
ED-SA	4.94 ± 0.15	-16.40 ± 0.28	5.04 ± 0.14	-12.00 ± 1.37	4.98 ± 0.13	-16.26 ± 0.23
100S-ED-SA	5.00 ± 0.10	-16.46 ± 0.56	5.04 ± 0.14	-12.55 ± 1.49	4.99 ± 0.04	-16.21 ± 0.38
250S-ED-SA	4.98 ± 0.13	-16.22 ± 0.52	5.08 ± 0.04	-12.02 ± 1.33	4.98 ± 0.08	-16.10 ± 0.56
100S	5.03 ± 0.11	-16.51 ± 0.53	5.08 ± 0.04	-11.32 ± 1.05	5.00 ± 0.11	-16.27 ± 0.08
250S	5.06 ± 0.17	-15.84 ± 0.76	5.14 ± 0.05	-11.21 ± 0.66	4.94 ± 0.34	-16.12 ± 0.34

The Biot number, $Bi = \frac{\overline{h_D}}{k_{water}}$, can also be calculated to be 0.08, where k_{water} is the thermal conductivity of water. The amount of heat transfer, $\overline{Q}_D$, during the droplet falling process can be calculated with Eq. (5-9) by applying the lumped capacitance method (considering Bi < 0.1). The amount of heat transfer, $\overline{Q}_D$, during the droplet falling process can be calculated with Eq. (5-9) by applying the lumped capacitance method.

$$\overline{Q_D} = \overline{h_D} A_D (T_i - T_\infty) = \rho V_D \cdot c_p \frac{dT}{dt} \tag{5-9}$$

where A_D is the surface area of the water droplet, T_i is the initial temperature of the water droplet, T_∞ is the temperature of the air, T is the temperature of the drop during the falling process. Integration of Eq. (5-9) and solving for the falling time leads to

$$t = \frac{\rho V_D \cdot c_p}{\overline{h_D} A_D} \ln\left(\frac{T_i - T_\infty}{T - T_\infty} \right) \tag{5-10}$$

where t is the droplet falling time. T is the droplet temperature during the falling at time t. Also, ρ is the density of water, V_D is the volume of the water droplet, and c_p is the specific heat capacity of water.

Assuming free-fall, the total falling time before the drop impact can be expressed as:

$$t_{falling} = \sqrt{\frac{2h}{g}} = \frac{\rho V_D \cdot c_p}{\overline{h_D} A_D} \ln\left(\frac{T_i - T_\infty}{T_{impact} - T_\infty} \right) \tag{5-11}$$

where $t_{falling}$ is the total falling time of the droplet falling from a distance h, and T_{impact} is the droplet temperature at the time just before its impact on the target surface. Solving Eq. (5-11), T_{impact} can be expressed as

$$T_{impact} = \left(T_i - T_\infty\right) \cdot \exp\left[-\left(\frac{\overline{h_D} A_D}{\rho V_D c_p} \right) \cdot \sqrt{\frac{2h}{g}} \right] + T_\infty \tag{5-12}$$

Table 5-4 shows the droplet impact temperatures, T_{impact}, before touching the target surfaces.

Table 5-4 Droplet impact temperatures.

Samples	**Sessile drop** T_{impact} **(°C)**	h **= 5 cm** T_{impact} **(°C)**	h **= 10 cm** T_{impact} **(°C)**
ON	4.75 ± 0.30	5.11 ± 0.07	4.98 ± 0.08
ED-SA	4.94 ± 0.15	5.02 ± 0.10	4.98 ± 0.13
100S-ED-SA	5.00 ± 0.10	5.03 ± 0.14	4.98 ± 0.04
250S-ED-SA	4.98 ± 0.13	5.07 ± 0.05	4.96 ± 0.09
100S	5.03 ± 0.11	5.07 ± 0.05	4.98 ± 0.11
250S	5.06 ± 0.17	5.13 ± 0.05	4.88 ± 0.18

As mentioned in 3.1, the total icing delay time can be analyzed from the images recorded by the high-speed camera. The freezing (heat transfer) rate of the water droplet on the target surfaces is expressed as follows:

$$q = \frac{dQ}{dt} \tag{5-13}$$

where q is the freezing heat transfer rate.

The total heat transfer in the whole freezing process can be calculated by:

$$Q = Q_v \cdot V_D = -\rho V_D c_p (T_f - T_{impact}) + \rho V_D H_{ls} \tag{5-14}$$

where Q is the amount of heat transferred during the icing process, Q_V is the heat transferred per unit of volume, H_{ls} is the latent heat of freezing, and T_f is the final temperature of the droplet. Therefore, the average freezing rate $\overline{q}$ can be calculated by:

$$\bar{q} = \frac{Q}{t_{freezing}} = \frac{Q_v \cdot V_D}{t_{freezing}} = \frac{-\rho V_D c_p (T_f - T_{\text{impact}}) + \rho V_D H_{ls}}{t_{freezing}} \tag{5-15}$$

where $t_{freezing}$ is the total freezing delay time of the water droplet on the target surface.

Also, referring to section 5.3.1, the average freezing rate $\bar{q}$ will be divided by the mass of each water droplet.

$$\overline{q_m} = \frac{\bar{q}}{m_D} = \frac{\bar{q}}{\rho V_D} \tag{5-16}$$

As shown in Figure 5-5a, surface wettability affects the final contact area between the water droplet and the target surface. The experimental results show that poorer surface wettability (more hydrophobic) leads to a smaller final contact area per unit mass $A_{c,\,m}$ between the water droplet and the target surface. The impact height also affects the final contact areas. Higher impact distance leads to a larger final contact area on the same target sample surface. In addition, the final contact area differences due to impact heights are smaller for a more hydrophobic surface. These results are important for engineering applications - the droplet impact height (kinetic energy) has less effect on the final contact area of a droplet on a more superhydrophobic surface. The mechanism behind these results might be that the more hydrophobic surfaces induce less drag force for the lateral motion of the droplet during its dynamic process. This makes the impact speed (kinetic energy) less important than heat transfer (thermal energy) in determining the expansion and retraction of the droplets.

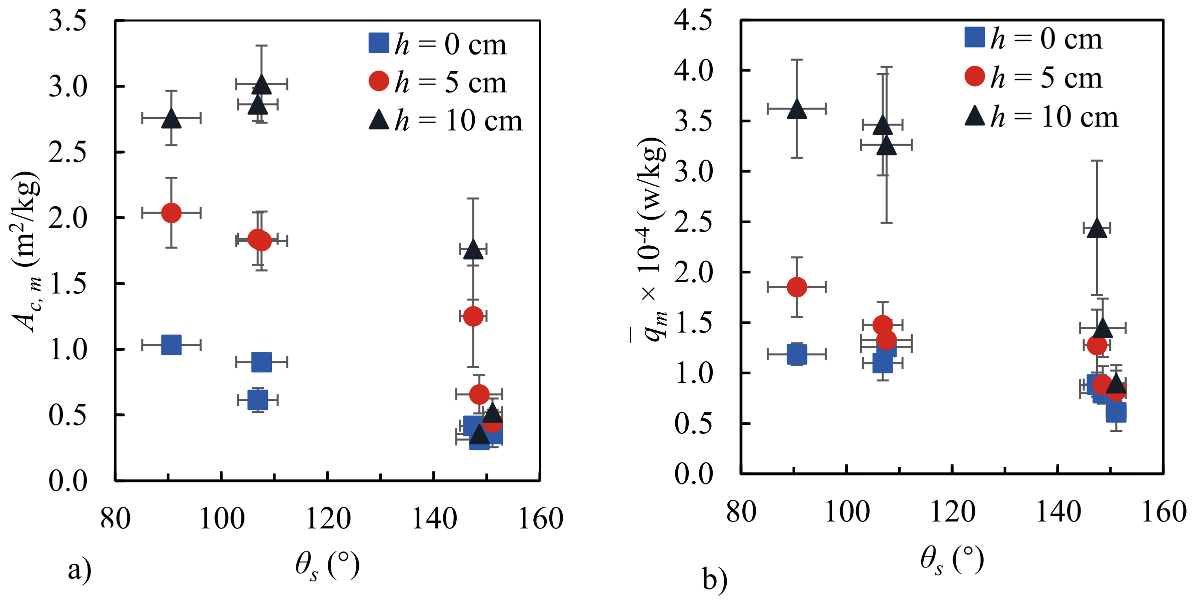

Figure 5-5 Representative relationship between the static contact angle θ_s of water droplets on the surfaces and a) the final contact area per unit mass $A_{c,\mathrm{m}}$, and b) the average freezing rate per unit mass $\bar{q}_m$. (h is the droplet impact height.)

Figure 5-5b illustrates the relationship between the average freezing rate per unit mass $\bar{q}_m$, and the surface wettability (static contact angles). It is clear that the average freezing rate per unit mass $\bar{q}_m$ decreases when the static contact angle θ_s increases (more hydrophobic surfaces). Also, if the impact distance increases, the average freezing rate per unit mass $\bar{q}_m$ increases, which means that a water droplet will freeze faster when the impact distance increases on the same target surface. In addition, when the static contact angle is higher, the differences in the average freezing rate per unit mass $\bar{q}_m$ due to differences in impact heights are smaller – a similar trend as in the final contact area results.

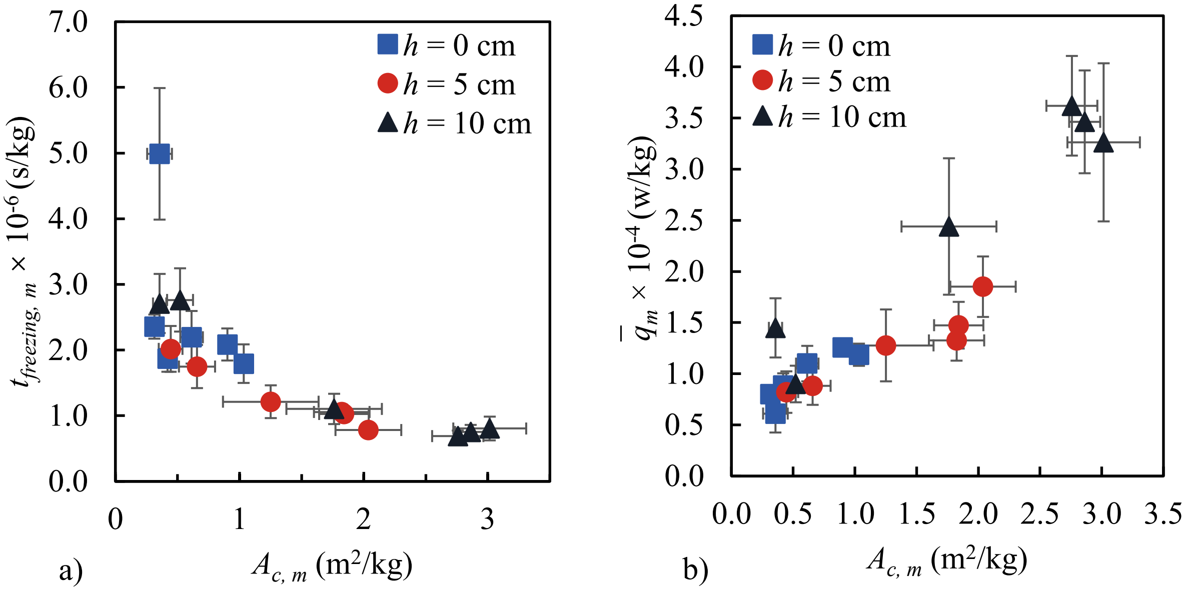

Figure 5-6 Representative relationship between the final contact area per unit mass $A_{c,\,m}$ of the water droplet and a) the total freezing time per unit mass $t_{freezing,\,\mathrm{m}}$, b) the average freezing rate per unit mass $\bar{q}_m$. (h is the droplet impact height.)

As shown in Eq. (5-13), The contact area between the droplet and the surface is important for controlling heat transfer between the liquid and the surface, i.e., the freezing rate. Data in Figure 5-6 confirm the relationship between the freezing delay time per unit mass $t_{freezing,\,m}$, the average freezing rate per unit mass $\bar{q}_m$ and the final contact area per unit mass of the water droplet on the tested surfaces. The freezing delay time per unit mass $t_{freezing,\,m}$ decreases when the final contact area per unit mass $A_{c,m}$ increases, while the average freezing rate per unit mass $\bar{q}_m$ increases when the final contact area $A_{c,\,m}$ increases. Also, Figure 5-6a illustrates that the freezing delay time per unit mass $t_{freezing,\,m}$ is approximately inversely proportional to the final contact area per unit mass $A_{c,m}$. Similarly, Figure 5-6b shows that the average freezing rate per unit mass $\bar{q}_m$ is approximately proportional to the final contact area per unit mass ($A_{c,m}$) as in Eq. (5-13). Overall, the experimental results agree with Newton's law of cooling. This analysis demonstrates that poor surface wettability contributes to the lower final contact area of the water droplet on the sample surface, leading to a lower freezing rate and longer freezing delay time. Higher impact distance also leads to a larger final contact area of the water droplet on the sample surface, contributing to a higher freezing rate and shorter freezing delay time.

5.6 Dimensional analysis of the icing process

The Weber number (We) has been used to indicate whether the kinetic energy or the surface tension is dominant in the droplet impact process. It is expressed as follows:

$$\mathrm{We} = \frac{\rho u^2 D_i}{\gamma_{LV}} \tag{5-17}$$

where ρ is the density of water (kg/m^3), u is the impact velocity (m/s) of a water droplet, related to the impact distance h. Also, D_i is the initial droplet diameter (m), and σ is the surface tension of water in the air (N/m). If the surface wettability is considered, the impact Weber number (We_i) is introduced [90] as

$$\mathrm{We}_i = \frac{\mathrm{We}}{0.5(1-\cos\theta_a)} = \frac{2\rho u^2 D_i}{\gamma_{LV}(1-\cos\theta_a)} \tag{5-18}$$

where θ_a is the advancing contact angle of the water droplet on a surface.

The dimensionless final contact diameter D_c^*, final contact area A_c^* and the dimensionless freezing delay time are introduced as follows.

$$D_c^* = \frac{D_c}{D_i} \tag{5-19}$$

$$A_c^* = \frac{A_c}{A_i} \tag{5-20}$$

$$t^{*} = \frac{t_{freezing} \cdot \sqrt{2gh}}{D_i} \tag{5-21}$$

where D_c, A_c and $t_{freezing}$ are the final contact diameter, final contact area, and total freezing delay time, respectively. Also, D_i, A_i and $t_{falling}$ are the initial diameter, cross-sectional area of the water droplet and the falling time before it impacts the surface, respectively. The experiments of sessile droplets will not be included in the dimensional analysis from the above definition.

Figure 5-7 and Figure 5-8 show the dimensional analysis results of water droplet freezing delay on the three zinc electrodeposited stainless steel surfaces. Also, the values of contact angles are transferred from degrees to radians.

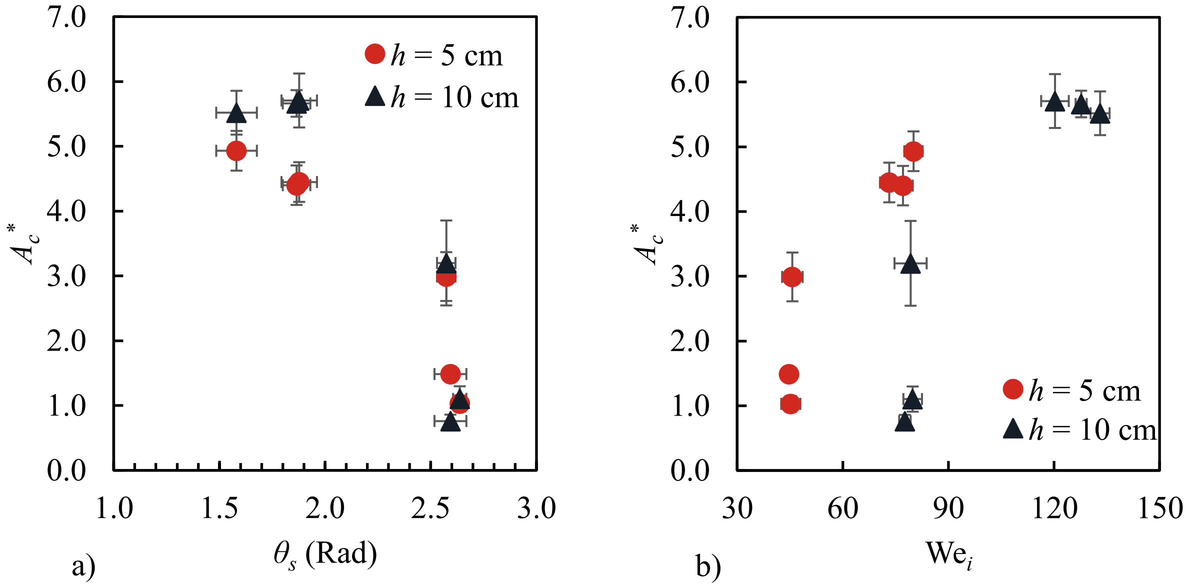

Figure 5-7 Representative relationship between the dimensionless final contact areas A_c^* and a) the static contact angle θ_s of water on the surfaces; b) the impact Weber number We_i. (h is the droplet impact height.)

Figure 5-7 shows that the dimensionless final contact areas A_c^* decreases when the static contact angle θ_s (Rad) increases (Figure 5-7a) or the impact Weber number We_i decreases (Figure 5-7b). These results further indicate that A_c^* is affected by surface wettability. Poor wettability (higher contact angle) leads to lower A_c^*, which means a smaller final contact area. Also, a higher impact height also leads to a higher dimensionless final contact area A_c^*. As discussed earlier, the final contact area is a critical factor in the freezing delay of the water droplet.

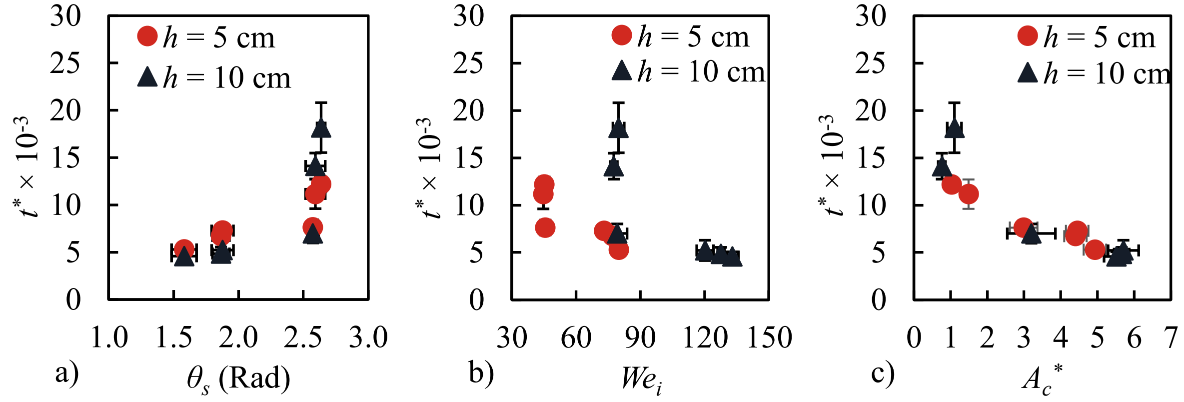

Figure 5-8 Representative relationship between the dimensionless freezing delay time t^* and a) the static contact angle θ_s of water on the surfaces; b) the dimensionless final contact areas A_c^*; c) the impact Weber number We_i. (h is the droplet impact height.)

Figure 5-8a shows that the dimensionless freezing delay time t^* increases when the static contact angle θ_s (Rad) increases. However, t^* decreases when the dimensionless final contact areas A_c^* increase (Figure 5-8b) or when the impact Weber number We_i increases (Figure 5-8c). Poor wetting leads to a higher static contact angle, contributing to a small final contact area. This final contact area determines the heat transfer between the water droplet and the targeted surface. Therefore, a more hydrophobic surface can further delay the freezing of water droplets due to the smaller final contact area. Also, the impact distance can affect the dimensionless freezing delay time. For the same static contact angle in Figure 5-8a or the same dimensionless final contact area, A_c^* in Figure 5-8c, the dimensionless time t^* is smaller when the impact distance increases. Figure 5-8b illustrates that the dimensionless freezing time t^* is approximately inversely proportional to the impact Weber number We_i.

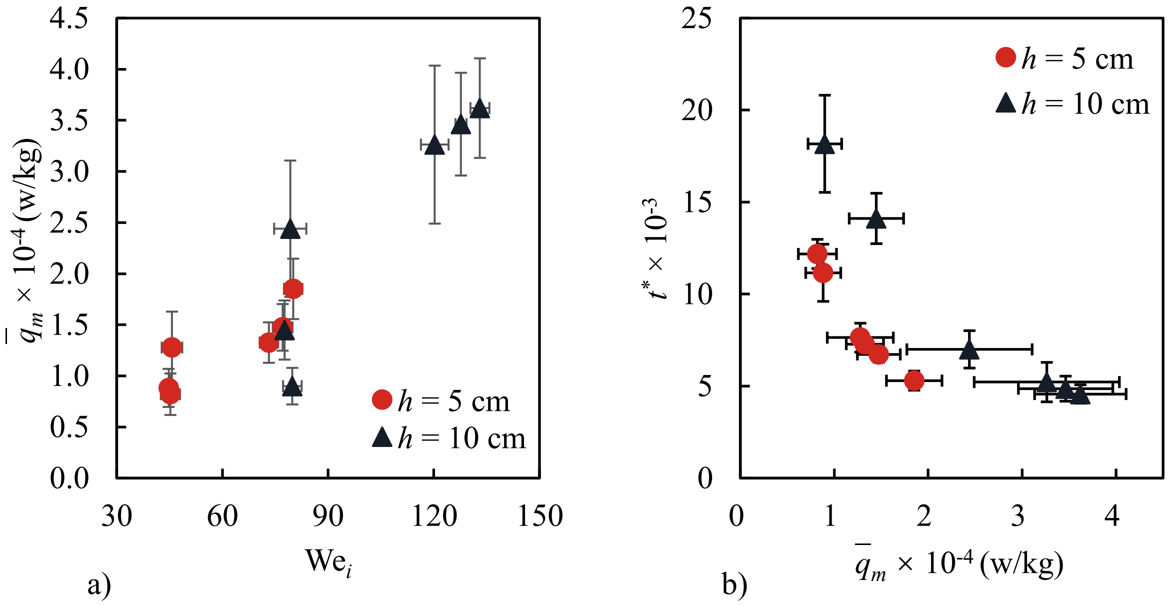

Figure 5-9 Representative relationship between the average freezing rate per unit mass $\bar{q}_m$ and a) the impact Weber number We$_i$, b) the dimensionless freezing delay time t^*. (h is the droplet impact height.)

The approximately inversely proportional relationship between the impact Weber number We$_i$ and the dimensionless freezing delay time t^* indicates that the average freezing rate per unit mass $\bar{q}_m$ should approximately be proportional to the impact Weber number We$_i$. Data in Figure 5-9a prove that the heat transfer rate per unit mass is proportional to the impact Weber number.

Due to higher impact velocity or a better wetting surface, the higher impact Weber number will contribute to a higher average freezing rate per unit mass; thus, the water droplet will be freezing faster. This trend is further demonstrated by Figure 5-9b, in which the average freezing rate per unit mass $\overline{q}_m$ is approximately inversely proportional to the dimensionless freezing delay time t^*.

To summarize, a more hydrophobic surface will have a smaller final contact area for droplets with the same impact velocity, contributing to a longer freezing delay and a lower average freezing rate per unit mass. At the same time, the impact height can also affect the dimensionless final contact area A_c^* and the dimensionless freezing delay time t^*. The higher impact distance can contribute to a larger dimensionless final contact area A_c^* and a higher average freezing rate per unit mass, leading to worse anti-freezing (smaller t^*) properties.

5.7 The durability of the irregularly roughened stainless-steel tiles

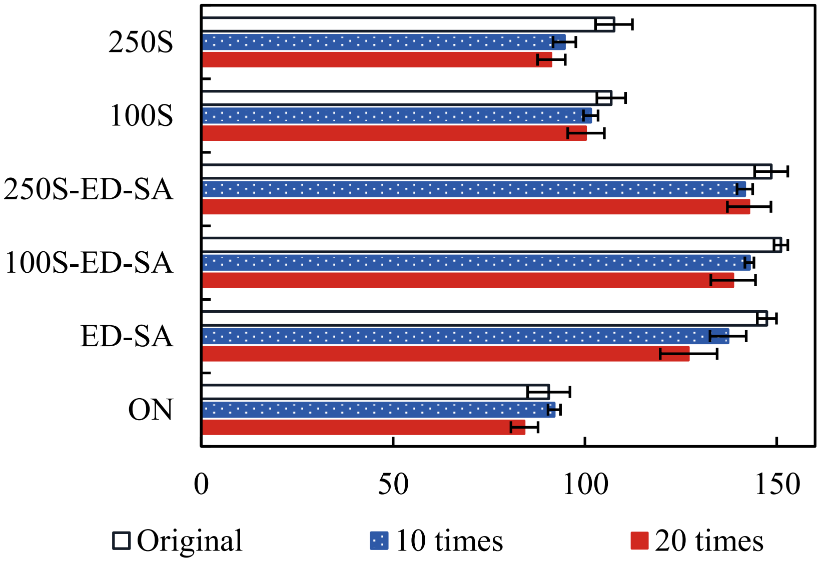

Figure 5-10 The static contact angles θ_s of six samples before and after multiple freezing and melting cycles.

In addition to the icing test, the durability of the samples was also examined. The results seem pretty reasonable. After 10 and 20 freezing and melting cycles, the static contact angles θ_s of the six tested samples were measured using the Dataphysics Contact Angle Instrument OCA 15 EC. Each measurement placed a water droplet with the same volume (20 µl) on the target sample surface. The "plynom fitting" method was used in the contact angle measurement because this method is proven effective for the asymmetrical water droplet on irregularly roughened stainless-steel surfaces. The measurement uncertainties are shown in Figure 5-10. The results show that the static contact angles θ_s of the samples only decrease slightly (by ~10%) after 10 cycles and decrease approximately by 15% after 20 cycles. Considering the measurement uncertainty, the untreated surface showed no significant change in wettability.

5.8 Summary

In previous studies [90], this has been tested that stainless steel surfaces with regular textures and different wettability at room temperature. However, none of those surfaces were *superhydrophobic*. Also, the earlier experiments were carried out at room temperature, which led to significant condensation on the target surfaces. In this study, (super)hydrophobic stainless-steel surfaces with zinc electrodeposition and stearic acid coating are developed and examined for their freezing delay properties. Experiments in the cold room (-14.2 ± 2.4 °C) help reduce condensation by maintaining a minimum temperature difference between the sample surface and the environment. The results of water droplet freezing on the target surfaces indicate that a further reduced wettability leads to a longer freezing delay. The sample 100S-ED-SA (sandblasting pre-treatment by 100 µm Al_2O_3 blasting media and zinc-electrodeposited, was finalized with the stearic acids coating, following the steps described in section 2.1) performed the best among all six samplers in terms of freezing delay with all impact heights. Also, the freezing delay performance of sandblasted samples is better than the one without sandblasting pre-treatment. The experimental investigation and heat transfer analysis lead to the following conclusions:

1. For most of the time (>98% of the total freezing delay time), the droplets are stationary on the surfaces with a fixed contact area between the droplet and the surface. This result leads to a crucial assumption that a fixed final contact area can be used in the heat transfer analysis.
2. The heat transfer analysis demonstrates that poor surface wettability contributes to the lower final contact area of the water droplet on the sample surface, leading to a lower freezing rate and longer freezing delay time. The higher impact distance will also lead to a larger final contact area of the water droplet on the sample surface, contributing to a higher freezing rate and shorter freezing delay time.
3. The dimensional analysis shows that a lower We_i (due to lower impact velocity or a poorer wetting surface) results in smaller A_c^* of water droplets (smaller final contact area A_c) and a lower average freezing rate per unit mass. Thus, a more hydrophobic surface will have a smaller final contact area for droplets with the same impact velocity, contributing to a longer freezing delay and a lower average freezing rate per unit mass. At the same time, the higher impact distance can contribute to a larger dimensionless final contact area A_c^* and a higher average freezing rate per unit mass, leading to faster freezing (smaller t^*).
4. The droplet impact height has less effects on the final contact area per unit mass $A_{c,m}$ and the average heat transfer rate per unit mass $\overline{q}_m$ of a droplet on a more hydrophobic surface. In other words, the superhydrophobic surfaces have better icephobic performance, even

for a droplet falling from a higher distance. This finding is significant in addressing engineering icing problems.

Although there are some limitations to the experiments, for example, the impact heights are relatively small (low Weber number), the same sample materials, and fixed room and cold plate temperatures. The droplet freezing delay experiment connects the droplet impact dynamics and freezing delay process, which fills the gap in the literature for experiments conducted on metal surfaces in subfreezing environments. Also, other researchers or engineers in the applications can use the critical effects of the final contact area and the assumption of a fixed droplet-substrate contact area. Due to the limitations of this study, more investigation is required for future studies.

The water droplet impact and freezing process on the irregularly roughened metal surface have been fully investigated experimentally. A more profound theoretical analysis is needed to understand the above experimental observation and conclusions. An analytical model will be developed in detail in Chapter 6.

Chapter 6 A Semi-analytical Framework for Single Water Droplet Impact and Freezing on Hydrophobic Surfaces

6.1 Introduction

The effects of icing problems on engineering structures are discussed in detail in Chapter 1. The ability of superhydrophobic surfaces to retard surface icing has been confirmed by many investigations [90,91,94,107,133,196–200], and the process has been analyzed theoretically and numerically by many researchers [185,191,201–215]. However, hydrophobic surfaces are not always icephobic [48,50]. The droplet impact dynamics and freezing process on irregularly roughened metal surfaces have not been fully understood. Previous modelling investigations are limited to separately studying droplet impingement and freezing processes. Therefore, it is essential to understand the mechanism of water droplet impact and freezing on these surfaces and explore the relationship between surface wettability and icing delay that occurred on (super)hydrophobic surfaces.

While a water drop impacts a surface in a cold environment, this droplet will experience six stages: *dynamic stage*, *supercooling stage*, *nucleation stage, recalescence/dendritic stage*, *equilibrium solidification stage* and *solid subcooling stage* [7,185,192,203,211,216–219]. The droplet dynamic stage can be further divided into four sub-stages: *before impact*, *maximum spread*, *maximum recoil/rebound*, and *equilibrium* [7,184,185,199,215,220–226]. On the one hand, many theoretical approaches assume known velocity profiles in a droplet upon impact and apply mass and energy conservation between the point of impact and the maximum spread to solve for the maximum spread diameter [7,185,215,226]. Mao et al. investigated the spread and rebound of liquid droplets impacting flat surfaces by applying energy conservation [185]. They developed a semi-empirical model to predict the maximum spread as a function of the Reynolds number (Re), the Weber number (We), and the static contact angle. In contrast, Bahadur et al. carried out a force balance analysis of the droplet to predict the maximum spreading radius of the droplet. However, they did not include in their analysis the resistance to the droplet other than surface tension [7]. Du et al. proposed an analytical model for the maximum spreading factor. This model extends the previous models to the viscous regime and presents a more precise model to predict the maximum spreading of the liquid drop [215]. Also, some research investigates the droplet dynamics in various temperatures [159,193,227,228]. Alizadeh et al. find that viscous dissipation and friction are significant at subzero temperatures, especially for droplet impact on hydrophilic surfaces. However, the temperature has less influence on the impact dynamics of droplets on (super)hydrophobic surfaces [159].

Numerical approaches are also used to simulate the transient flow field during the droplet dynamic stage using computational fluid dynamics [228–233]. Shin et al. simulate the three-dimensional impact of a droplet onto a solid surface using the level contour reconstruction method [234] Sidik et al. applied the lattice Boltzmann method (LBM) to investigate the spreading dynamics of drops on solid surfaces [225]. Guo et al. used the volume of fluid (VOF) approach to investigate the impact of droplet dynamics on the heated flat solid surface [228]. Wu et al. present an atomistic–continuum hybrid method to investigate the spreading dynamics of drops on solid surfaces [233]. From analytical or numerical considerations, the spreading of an impacting droplet on the maximum spreading radius or factor has been investigated comprehensively. In Chapter 5, the freezing delay experiments prove that the droplet dynamic stage is relatively short compared to the whole freezing delay process (including the dynamic stage), as illustrated in Figure 5-2a. Also, this has been proved by other researchers in earlier studies [91]. In other words, the final contact radius (area) will be a crucial point for the heat transfer analysis in the water droplet freezing process. Therefore, determining the droplet final contact conditions (final contact diameters D_c or areas A_c) is the main objective during the droplet dynamic stage.

The droplet will continue to be cooled to a specific temperature, i.e., the nucleation temperature, T_n, after the relatively short dynamic stage. This period is defined as the droplet supercooling stage. Ice nucleation is a process starting with forming a critical size nucleus, which has to overcome a specific energy barrier. If the ice nucleus is initiated by water molecules clustering, this is defined as homogeneous nucleation. In contrast, if the ice nucleation is triggered by foreign particles or an ice nucleus generated on an interface, it is named heterogeneous nucleation [235]. Homogeneous nucleation has the highest energy barrier, leading to a lower nucleation temperature. For example, the nucleation of a droplet of purified water with no contaminants happens at approximately -35 °C [236–241].

In contrast, the energy barrier for heterogeneous nucleation is smaller than that of the homogeneous one. The nucleation time (t_n) is determined by the nucleation rate, J, which is determined by the energy barrier that needs to be overcome. The nucleation rate can be estimated using the Monte Carlo method, molecular dynamics simulation, Lattice Boltzmann Method (LBM) and the classical nucleation theory [235,242–248]. The classical nucleation theory is a simplified but reliable theory that has been proven effective for providing excellent quantitative nucleation rate predictions without extensive computational cost [235,246]. However, the accuracy of the classical theory depends on identifying the precise values of the chemical potential during the phase transition, the interfacial surface tension [246,249], the attachment rate of the critical nuclei [208,243] and the Zeldovich factor [208,250].

In addition, the formation of critical ice nuclei indicates the start of the droplet's freezing process. Before the equilibrium solidification, the water droplet goes through another stage called the recalescence/dendritic stage, and the nucleation is also the start point of this period. At this stage, the nuclei continue to grow and release heat from the phase change process. The mixture of water and ice embryos is maintained at the freezing/melting point, $T_m = 0$ °C, after this specific time. This rapid increase in temperature, due to the release of latent heat of water, occurs instantaneously (in less than 0.1 s) [121,191–193,208,218,247]. Most analytical and numerical models did consider the effect of the recalescence stage and proposed an effective latent heat of fusion H_{eff}, but did not consider the time consumed during this stage [191–193,208,246,251]. The experimental research from Meng et al. also indicates that the time for the recalescence stage of a droplet with 1.4 mm and 2.0 mm diameters are 0.017 s and 0.023 s, respectively, which is less than 0.1 s [208]. Chaudhary et al. found that the temperature increased dramatically to the melting point in less than 60 milliseconds during the recalescence stage [247]. Kim et al. proved that recalescence takes only 0.1 s, and the temperature of the freezing droplet jumps to 0 °C [252]. In this study, to simplify the analysis of the freezing process, the time for the recalescence stage is assumed to be zero, $t_r \approx 0$ s.

The Stefan problem has been widely applied to analyze the equilibrium solidification stage [191–193,205,246,251,253–255]. Many analytical methods address the freezing problem by assuming the solid phase initially at the melting/freezing point, also known as the one-region Stefan problem. Similarity solutions often exist by solving the Stefan problem in semi-infinite domains[204,256]. The following assumptions are required before addressing the problem analytically: (1) the temperature distribution and heat transfer are described by the heat conduction equation (neglect natural convection in the liquid phase); (2) an explicit interface (or phase change boundary) between the two phases can be considered; (3) the temperature of the interface is prior known; (4) the liquid water domain in the droplet is considered as semi-infinite; (5) any volume change due to the phase change is negligible; (6) the densities of both phases are the same and kept at constant [257]. J. Madejski used the Stefan problem to compute the thickness of the solidified layer in the droplet [211]. Other researchers also solved the one-phase Stefan problem analytically or numerically to track the interface movement [191,192], compute the temperature distribution [216,247], and estimate the solidification time [246,257] for a spherical droplet [205,246], or a sessile droplet lying on a supercooled solid surface (either hydrophilic or (super)hydrophobic) [216,247]. However, none of these analytical approaches considered the droplet impact and dynamic process. In the presented analytical framework, the droplet impact will be considered as a result of the final contact diameter, which is a critical factor for heat transfer during the impact and freezing processes. Hence, the previous modelling work can be extended to a falling droplet. Some models combine the dynamic process with the freezing period. For example, Bahadur et al. proposed a model for ice formation on superhydrophobic surfaces that predicted the retraction position of the droplet as a function of time [7]. However, this model is relatively simple and does not consider the drags during the droplet dynamic process and has limited the analysis within the dynamic process. Also, the model cannot provide a detailed analysis of the freezing process, and as mentioned previously, the dynamic process is relatively shorter than the whole freezing period. Hence, the outcome has limited benefits for engineering applications. In addition, Zhang et al. developed a numerical model for the dynamics of a supercooled water droplet to understand the relationship between droplet rebound, adhesion and wettability under supercooled conditions. However, only the droplet dynamic period is considered without further analysis of the freezing process [193].

In this chapter, an analytical model for droplet dynamics and freezing on solid substrate surfaces is developed to fill the gaps discussed above. Section 6.2 presents the objectives and methodology for this analytical framework, and the following section 6.3 and section 6.4 present a detailed analysis of this model. The results and discussion are represented in section 6.5.

6.2 Objectives and methodology

The objective of the analytical framework is to find the total freezing delay time per unit of mass, $t_{freezing,\ m}$, for a water droplet impacting and freezing on irregularly roughened stainless-steel surfaces with various wettability. The starting time (t = 0) is set when the droplet impacts the substrate surface. The nucleation time, solidification time and total freezing delay time are based on this starting time. Results in Figure 5-2a show that the time required to freeze a droplet entirely is longer than the dynamic period. The time difference between these two processes is almost two orders of magnitude. Also, this finding agrees well with other research in the literature [91,257]. Hence, this chapter will investigate these two processes separately, i.e., the droplet dynamic and freezing processes. In addition, the heat transfer during the dynamic process is negligible since the droplet dynamic period is relatively short compared to the whole freezing process, as discussed previously.

According to the different stages of the droplet impact and freezing on surfaces, the methodology to develop the analytical framework in this chapter is illustrated in Figure 6-1 and follows the steps below:

1. calculate the final contact diameter D_c of the droplet impact on the target surface as a function of contact angle (θ), Weber number (We), Reynolds number (Re) and initial droplet diameter (D_i) by applying energy conservation;

2. calculate the droplet-substrate interface temperature profile for the supercooled water drop by solving the 1-D transient heat conduction;
3. compute the nucleation rate as a function of the droplet-substrate interface temperature, $J\,(T_{int})$, by applying the classic nucleation theory;
4. calculate the number of critical nuclei, N, and mark the time and temperature when $N \approx 1$ as nucleation time t_n and temperature T_n;
5. using the nucleation temperature as the initial temperature of the droplet, find an approximate analytical solution to a one-phase Stephen problem at the equilibrium solidification stage;
6. estimate the equilibrium freezing time t_s;
7. calculate the total freezing delay time per unit of mass $t_{freezing,\,m} = (t_n + t_s)\,/\,m$.

The following sections present a detailed analysis of each droplet impact and freezing stage.

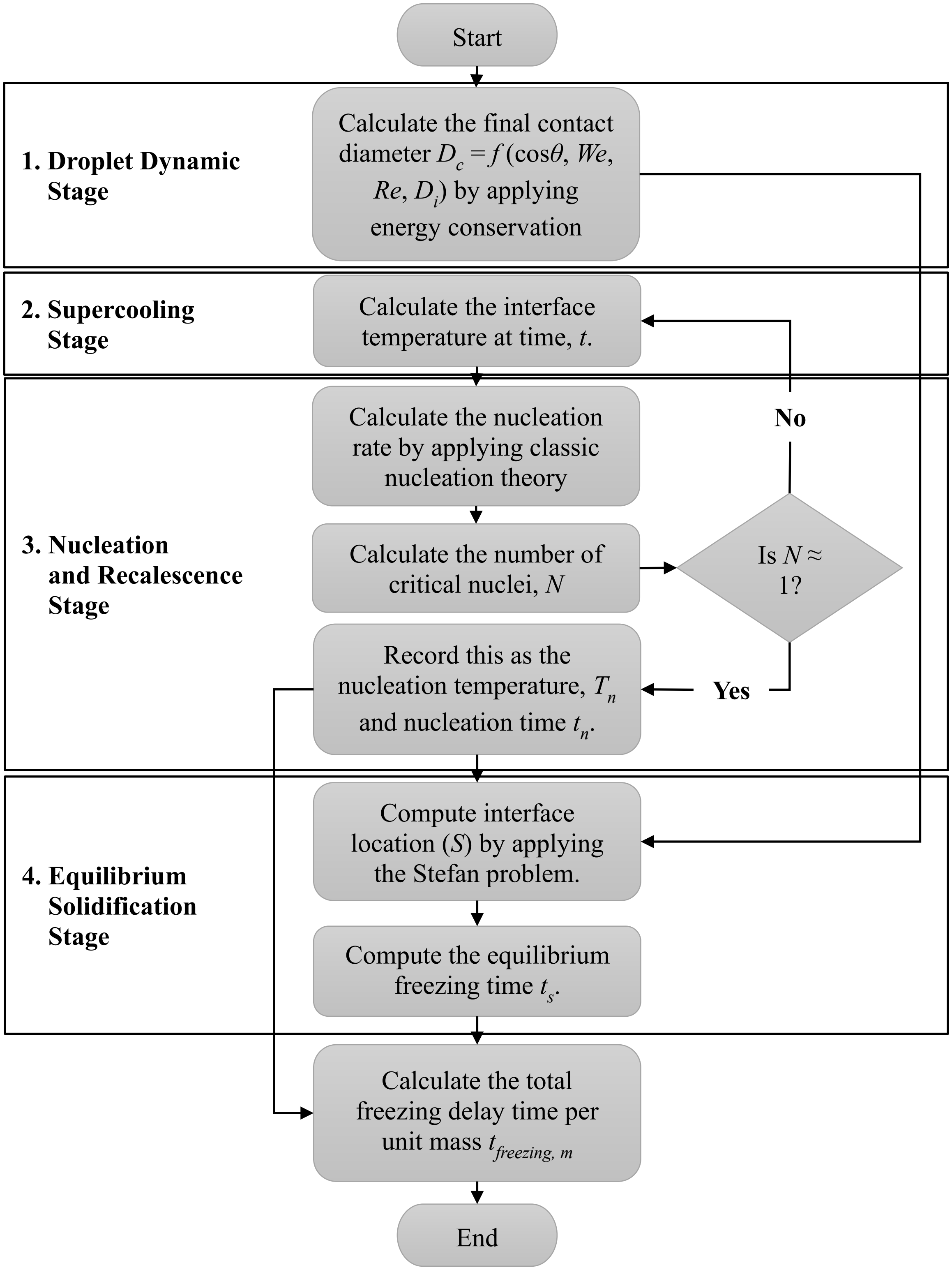

Figure 6-1 Flow chart outlining the analytical framework

6.3 Analysis based on energy conservation during the droplet dynamic stage

From the energy conservation perspective, the energy before impact equals the final state surface energy and energy dissipation during the impact and oscillation period of droplet impact on the cold metallic surface. The energy analysis neglects the heat transfer during the droplet oscillation since this period is relatively short compared to the freezing time interval [198,214]. Mao et al. divided the impact stage into four different stages and other researchers: *before impact*, *maximum spread*, *maximum recoil/rebound*, and *equilibrium* [185,222,258,259]. The maximum spread and maximum recoil/rebound are related to the dynamic behaviour of the droplet while impacting surfaces. However, the maximum spread and recoil/rebound is not required to analyze the mechanism of droplet icing on cold metallic surfaces. The dynamic period can be neglected compared to the whole freezing process [198,214]. Therefore, the critical element for this analysis is to find the final contact diameter D_c (area A_c). The stages *before impact* and *equilibrium* are considered and analyzed for preparing the future heat transfer model.

For the first stage, assuming the potential energy reference is set at the metallic surface, when the droplet falls from the syringe pump needle and just upon impacting the cold metallic surface ($t = 0$), it contains initial kinetic energy, E_{ki} and the initial surface energy, E_{Si}. Therefore, the total energy, E_i, of the droplet before impact can be expressed as:

$$E_i = E_{k_i} + E_{s_i} \tag{6-1}$$

where the kinetic energy, E_{ki} and the surface energy, E_{Si} can be expressed as:

$$E_{k_i} = \frac{1}{2}mu^2 = \frac{1}{2}(\rho V)u^2 \tag{6-2}$$

$$E_{s_i} = A_i\gamma_{LV} = \left(\pi D_i^2\right)\gamma_{LV} \tag{6-3}$$

For the (final) equilibrium stage, after the oscillations during the dynamic period, the energy has been dissipated, E_{diss}, by the viscosity of the droplet and friction between the droplet and the surface. Therefore, the only energy component for droplets is the surface energy, E_{sf} and can be expressed as:

$$E_{s_f} = E_{s_{f,LV}} + E_{s_{f,SL}} - E_{s_{f,SV}} \tag{6-4}$$

where the surface energy components between liquid, substrate and air can be expressed as:

$$E_{s_{f,LV}} = A_{LV}\gamma_{LV} \tag{6-5}$$

$$E_{s_{f,SL}} = A_{SL}\gamma_{SL} = \frac{\pi}{4}D_c^2\gamma_{SL} \tag{6-6}$$

$$E_{s_{f,SV}} = A_{SV}\gamma_{SV} = \frac{\pi}{4}D_c^2\gamma_{SV} \tag{6-7}$$

According to Eq. (6-8)Young's equation, the ($E_{sf,\,SL}$ - $E_{sf,\,SV}$) can be simplified as:

$$\gamma_{SL} - \gamma_{SV} = \gamma_{LV}\cos\theta \tag{6-8}$$

$$E_{s_{f,SL}} - E_{s_{f,SV}} = \frac{\pi}{4}D_c^2\left(\gamma_{SL} - \gamma_{SV}\right) = \frac{\pi}{4}D_c^2\gamma_{LV}\cos\theta \tag{6-9}$$

The droplet on the substrate surface is assumed to be a spherical cap with a surface area in the air A_{LV}. When the contact angle θ is smaller than 90°, the surface area of the spherical cap can be expressed as:

$$A_{LV,\ \theta\le 90^\circ} = \frac{2\pi D_c^2\left(1-\cos\theta\right)}{4\sin^2\theta} \tag{6-10}$$

If the contact angle θ is more significant than 90°, the area of the spherical cap is as follow:

$$A_{LV,\ \theta\ge 90^\circ} = \frac{2\pi D_c^2\left(1+\cos\theta\right)}{4\sin^2\theta} \tag{6-11}$$

Hence, the surface energy at the equilibrium stage, E_{sf} and can be rearranged as follows:

$$E_{s_f} = \begin{cases} \dfrac{\pi D_c^2 \gamma_{LV} \cdot \left(\cos^2\theta + \cos\theta + 2\right)}{4 \cdot \left(\cos\theta + 1\right)}, \text{ when } \theta \le 90^\circ; \\ \dfrac{\pi D_c^2 \gamma_{LV} \cdot \left(\cos^2\theta - \cos\theta - 2\right)}{4 \cdot \left(\cos\theta - 1\right)}, \text{ when } \theta \ge 90^\circ. \end{cases} \tag{6-12}$$

The energy conservation can be established between the before impact stage and equilibrium stage as:

$$E_i = E_f + E_{diss} \tag{6-13}$$

or,

$$E_{k_i} + E_{s_i} = E_{s_f} + E_{diss} \tag{6-14}$$

where E_{diss} is the energy dissipated due to liquid viscosity and the friction between the droplet and the roughened metallic surface. To find the E_{diss}, Eq. (6-14) is divided by E_{si}, and the original equation can be non-dimensionalized as:

$$E_{k_i}^* + 1 = E_{s_f}^* + E_{diss}^* \tag{6-15}$$

where E^*_{ki}, $E^*_{sf,}$ and E^*_{diss} are showing as follows:

$$E_{k_i}^* = \frac{E_{k_i}}{E_{s_i}} = \frac{{}^1\!/_2\,\rho u^2 \cdot \left({}^1\!/_6\,\pi D_i^3\right)}{\pi D_i^2 \gamma_{LV}} = \frac{\rho u^2 D_i}{12\gamma_{LV}} = \frac{\mathrm{We}}{12} \tag{6-16}$$

$$E_{s_f}^* = \begin{cases} \dfrac{\left(\cos^2\theta + \cos\theta + 2\right)}{4\left(\cos\theta + 1\right)} \cdot \left(\dfrac{D_c}{D_i}\right)^2, \text{ when } \theta \le 90^\circ; \\ \dfrac{\left(\cos^2\theta - \cos\theta - 2\right)}{4\left(\cos\theta - 1\right)} \cdot \left(\dfrac{D_c}{D_i}\right)^2, \text{ when } \theta \ge 90^\circ. \end{cases} \tag{6-17}$$

$$E_{diss}^* = \frac{E_{diss}}{\pi D_i^2 \gamma_{LV}} \tag{6-18}$$

Many studies demonstrated that this dimensionless energy dissipation, E_{diss}^*, could not be solved analytically during the droplet oscillation period [185,259]. However, the E_{diss}^* is a function of Reynolds number (Re), Weber number (We) or impact Weber number (We$_i$), and dimensionless contact diameter (D_c^*), which is defined in this thesis as:

$$D_c^* = \frac{D_c}{D_i} \tag{6-19}$$

With experimental results of the droplet freezing on a metallic surface presented in chapter 5, a correlation for E_{diss}^* is developed using the least square data regression (R^2 = 0.96) as shown in Eq. 6-20:

$$E_{diss}^* = f\left(\mathrm{Re}, \mathrm{We}, \mathrm{D}_c^*\right) = \frac{e^{25.26}\mathrm{We}^{2.80}}{\mathrm{Re}^{4.53}} D_c^{*-0.50} \tag{6-20}$$

By substituting Eq. (6-16), (6-17), (6-18), (6-19), and (6-20) into Eq. (6-15), the original equation can be simplified and rearranged as:

$$C_3 = C_2 \cdot \left(D_c^*\right)^2 + \mathrm{C}_1 \cdot \left(D_c^*\right)^{-0.50} \tag{6-21}$$

where C_1, C_2, and C_3 can be expressed as:

$$C_1 = \frac{e^{25.26}\mathrm{We}^{2.80}}{\mathrm{Re}^{4.53}} \tag{6-22}$$

$$C_2 = \begin{cases} \dfrac{\left(\cos^2\theta + \cos\theta + 2\right)}{4\left(\cos\theta + 1\right)}, \text{ when } \theta \leq 90^\circ; \\ \dfrac{\left(\cos^2\theta - \cos\theta - 2\right)}{4\left(\cos\theta - 1\right)}, \text{ when } \theta \geq 90^\circ. \end{cases} \tag{6-23}$$

$$C_3 = \frac{\mathrm{We}}{12} + 1 \tag{6-24}$$

Therefore, the D_c^* can be calculated from Eq. (6-21). Figure 6-2 represents predictions of the dimensionless final contact diameter of the water droplet with the experimental measurements. A good agreement within 0.1% is observed. As mentioned previously, the final contact diameter is a critical factor which can connect the droplet impact and freezing process. By solving Eq. (6-21) and substituting the dimensionless final contact diameter in Eq. (6-19), the droplet final contact diameter can be predicted, which can also be used to address the solidification time in section 6.4.3.

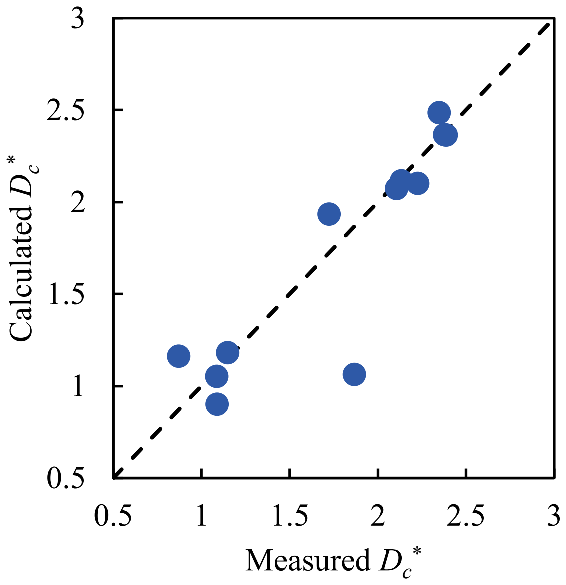

Figure 6-2 The comparison of calculated dimensionless droplet contact diameters from Eq. (6-21) with the experimental data

6.4 Analytical consideration of the droplet freezing on substrate surfaces

The droplet dynamic process has been analyzed in section 6.3. This section will focus on the freezing process of the droplet. The freezing process can also be divided into the supercooling stage, recalescence/dendritic stage, equilibrium solidification stage and solid subcooling stage. The objective of this step is to compute the total freezing delay time per unit of mass, $t_{freezing,\,m}$:

$$t_{freezing,\,m} = \frac{t_{freezing}}{m} = \frac{t_n + t_r + t_s}{m} \tag{6-25}$$

where m is the mass of the droplet, t_n is the nucleation time, t_r is the recalescence time, and t_s is the time of equilibrium solidification.

6.4.1 Liquid supercooling stage

As previously mentioned, the dynamic period is two orders of magnitude shorter than the total freezing delay time. Hence, the heat transfer during the dynamic process is negligible. After the water droplet impact and dynamic process (i.e., once the droplet becomes stationary on the surface), it starts to be cooled in contact with the subfreezing substrate and the cold environment. The initial temperature of the droplet is assumed to be the impact temperature, T_{impact}, which is higher than the melting/freezing point of water $T_m = 0$ °C, while the temperature of the subfreezing substrate, contacted with the cold plate, is fixed at T_{cp}, which is lower than T_m. The water drop will stay in the liquid phase even at a temperature below the melting/freezing point, and this phenomenon is defined as supercooling. Heat transfer in the liquid and solid phases is governed by the 1-D transient heat conduction equation. In this stage, a simplified 1-D transient model tracks the interface temperature at the time, t. The model neglects fluid convection effects due to the small size of the droplet. The interface temperature profile T_{int} (t) can be estimated by solving the heat conduction equations in the substrate and droplet domain, respectively, as shown in Figure 6-3.

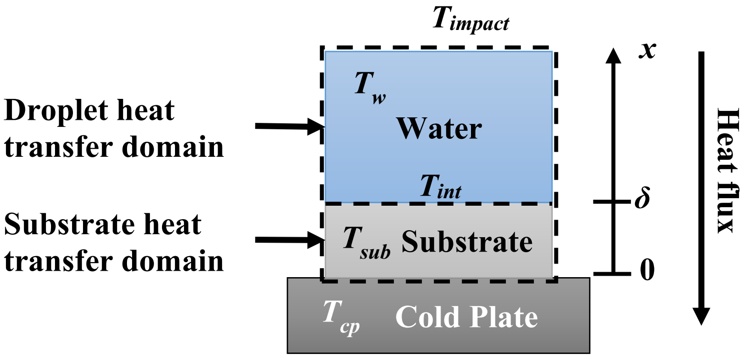

Figure 6-3 Schematic of the 1-D transient model in the liquid supercooling stage

The 1-D transient conduction equations for the droplet and substrate heat transfer domain are as follows:

$$\frac{\partial^2 T_{sub}}{\partial x^2} = \frac{1}{\alpha_{sub}} \cdot \frac{\partial T_{sub}}{\partial t} \text{ in the substate domain } 0 < x \leq \delta \quad (6\text{-}26)$$

$$\frac{\partial^2 T_w}{\partial x^2} = \frac{1}{\alpha_w} \cdot \frac{\partial T_w}{\partial t} \text{ in the substate domain } x \geq \delta \quad (6\text{-}27)$$

where T_{sub} is the temperature of the substrate, T_w is the droplet temperature, δ is the thickness of the substrate, α_{sub} and α_w are the thermal diffusivities of substrate and water, respectively. These heat conduction equations are subject to the following initial and boundary conditions.

$$\begin{cases} T_{sub}(0,t) = T_{cp} \\ T_w(\delta,t) = T_{sub}(\delta,t) \\ T_w(\infty,t) = T_{impcat} \\ T_{sub}(\delta,0) = T_w(x,0) = T_{impact} \text{ at } x \geq \delta \end{cases} \quad (6\text{-}28)$$

The droplet falls from a certain height, *h*, and impacts the target surface. As discussed in section 6.1, the dynamic process and time are neglected when analyzing the freezing process. Hence, the initial temperature of the droplet can be assumed as $T_w(x,0) = T_{impact}$. The first boundary condition assumes that the temperature of the cold plate is constant and independent of time. This is because the cold plate is connected to a thermal bath in the experiment, and the thermal mass of the cold plate is much larger than the droplet. The droplet in contact with the substrate will not significantly change the temperature of the cold plate.

Additionally, the two heat conduction equations share the same interface, where the temperature is assumed to be the same at $T_{int}(t)$ at $x = \delta$. Also, before the equilibrium solidification stage, the interface location is fixed at the substrate and droplet contact line ($x = \delta$). The third boundary condition is that the temperature of the droplet at the position far away from the substrate equals the temperature when it impacts the surface, T_{impact}. The governing equations can be solved by applying the similarity method. The analytical solutions can show the temperature profile in the substrate and water liquid domains, which are always valid during the droplet supercooling stage in this model. The detailed solutions are presented in Appendix D, and the solutions of these equations are shown as follows:

$$T_{sub}\left(x,t\right)=T_d+\left(T_{cp}-T_d\right)erfc\left(\frac{x}{2\sqrt{\alpha_{sub}t}}\right)\ \left(0<x\leq\delta\right) \tag{6-29}$$

$$T_w\left(x,t\right)=T_d+\left(T_{cp}-T_d\right)\frac{erfc\left(\frac{\delta}{2\sqrt{\alpha_{sub}t}}\right)}{erfc\left(\frac{x}{2\sqrt{\alpha_w t}}\right)}erfc\left(\frac{x}{2\sqrt{\alpha_w t}}\right)\ \left(x\geq\delta\right) \tag{6-30}$$

where *erfc*(x) is the complementary error function and *erfc*(x) = 1- *erf*(x), and *erf*(x) is the error function.

In this stage, the main objective is to find the interface temperature at time t, T_{int} (δ, t) as an input for the nucleation stage. By substituting $x = \delta$ into any one of the Eq. (6-29) or Eq. (6-30), the interface temperature of the droplet in contact with the solid substrate can be estimated as:

$$T_{\text{int}}\left(t\right)=T_d+\left(T_{cp}-T_d\right)erfc\left(\frac{\delta}{2\sqrt{\alpha_{sub}t}}\right) \tag{6-31}$$

6.4.2 Nucleation and recalescence stages

Ice nucleation is the formation of critical nuclei. An energy barrier, ΔGv, must be overcome to start this process. Many approaches are used to analyze this process, as discussed in section 6.1, for example, Monte Carlo, molecular dynamics, Lattice Boltzmann Method (LBM) and the classical nucleation theory [235,242–248]. In this study, the classical nucleation theory is used to analyze and compute the nucleation rate of the formation of the nuclei in the droplet on various surfaces with different wettability since this technique is straightforward, implemented easily, requires less computing power, explicates the fundamental physics of the nucleation, and is well established by P. V. Hobbs [235]. Homogeneous nucleation requires completely pure material and no interference from external particles, which is generally not possible in the scope of engineering applications. Therefore, heterogeneous nucleation will be the primary nucleation mechanism in this study. Also, most research assumes that heterogenous nucleation occurs on the contact surface between the droplet and the solid substrate [7,208–210,214,246,247,257,260]. Hence, this assumption is also adopted in the cases in this study.

According to the macroscopic theory of heterogeneous nucleation, the nucleation rate can be expressed as follows [178,235,246,250,261].

$$J = n_L Z_{hete} F_D \exp\left(-\frac{\Delta G^*_{hete}}{k_B T_{int}} \right) \tag{6-32}$$

where n_L is the number density of molecules in the liquid, Z_{hete} is the heterogeneous Zeldovich factor [250], F_D is the net rate of attachment to the critical nuclei, while the factors in the exponential function are the energy barrier for the nucleation ($\Delta G_{hete}{}^*$) that controls the rate of heterogeneous nucleation rate, the Boltzmann constant $k_B = 1.38064 \times 10^{-23}$ J/K [262], and the interface temperature T_{int} in Kelvin (K). The interface temperature can be calculated in the liquid supercooling stage and coupled with Eq. (6-32). Hence, the other factors are required to be addressed in the following parts.

In the classic heterogeneous nucleation theory, ice embryo formation contributes to the change in Gibbs energy, ΔG. The ice nuclei are generated on the substrate surface (interface) [208,209,246,257]. This consideration is based on thermodynamic energy balance; that is, the nucleus will continue to grow when the sum of the bulk free energy of the nucleating phase and the surface free energy between the nucleus and the liquid phase decreases as the size of the nucleus increases. Consequently, depending on the size of the nucleus, the sum of the free energies may increase as its radius increases. When the size reaches a threshold value, nucleation occurs. Assuming the nucleus is a sphere, the threshold size is defined as the critical nucleation radius, r^*.

$$r^* = \frac{-2\gamma_{SL}}{\Delta G_V} \tag{6-33}$$

where γ_{SL} is the interfacial tension between the solid (ice) and liquid (water) phase. ΔG_V is the volumetric Gibbs energy change between the bulk ice nucleus and the bulk liquid water phase, which can be estimated as follows [245].

$$\Delta G_V = \frac{T_{int} - T_m}{T_m} \Delta H_{SL} \tag{6-34}$$

where T_m is the melting/freezing temperature of water at 1 atm in Kelvin, i.e., 273.15 K. T_{int} is the interface temperature between the subcooled droplet and the substrate surface, ΔH_{SL} is the volumetric enthalpy of fusion of water, which is 3.34×10^{-8} J/m^3 [262]. The free energy barrier (ΔG_{hete}^*) for heterogeneous nucleation be estimated as [178,235]:

$$\Delta G^*_{hete} = \frac{8\pi\gamma_{SL}}{3\left(\Delta G_V\right)^2} f\left(\cos\left(\theta\right), X\right) \tag{6-35}$$

where $f(\cos(\theta), X)$ is the geometrical factor as a function of X for different contact angles [178], which is expressed as:

$$\begin{aligned}
&f\left(\cos(\theta_{IW}), X\right) = 1 + m + X^3\left(2 - 3n + n^3\right) + 3X^2\cos(\theta_{IW})\left(n-1\right)\\
&m = \frac{1 - X\cos(\theta_{IW})}{g}\\
&n = \frac{X - \cos(\theta_{IW})}{g}\\
&g = \sqrt{1 - 2X\cos(\theta_{IW}) + X^2}
\end{aligned} \tag{6-36}$$

where θ_{IW} is the contact angle of the ice nucleus in the supercooled liquid water on the substrate surface in contact with a nucleating particle with radius R_p, and the X is the ratio between the radius of the nucleating particle R_p and the critical nucleation radius r^*. The ice nucleating particle is a particle which acts as the nucleus for the formation of an ice embryo. It can be dust or surface defects in contact with the droplet.

$$X = \frac{R_p}{r^*} \tag{6-37}$$

The $\cos(\theta_{IW})$ can be estimated by applying Young's equation of the droplet on the substrate surface in the air and the ice on the substrate surface in the subcooled liquid water droplet.

$$\begin{aligned} \gamma_{SA} - \gamma_{SW} &= \gamma_{WA} \cos\theta \\ \gamma_{SA} - \gamma_{SI} &= \gamma_{IA} \cos\theta_I \\ \gamma_{SW} - \gamma_{SI} &= \gamma_{IW} \cos\theta_{IW} \end{aligned} \tag{6-38}$$

where S, A, W, and I denote substrate surface, air, liquid water and ice. Eq. (6-38) can be solved and lead to the following.

$$\gamma_{IW} \cos\theta_{IW} = \gamma_{IA} \cos\theta_I - \gamma_{WA} \cos\theta \tag{6-39}$$

Also, the contact angles of θ_I and θ for a sessile droplet [209] showed no apparent difference, as proved by Yamada et al. Therefore, the $\cos(\theta_{IW})$ can be estimated as:

$$\cos\theta_{IW} = \frac{\gamma_{IA} - \gamma_{WA}}{\gamma_{IW}} \cos\theta \tag{6-40}$$

where γ_{IA} and γ_{WA} are assumed to be 0.106 and 0.077 N/m [255,263].

In summary, the factors in the exponential function can be estimated by Eqs. (6-35), (6-36), and (6-37). n_L is the number density of molecules in the liquid and can be expressed as:

$$n_L = \frac{N_A \rho_L}{M_L} \tag{6-41}$$

where N_A is the Avogadro's constant, which equals 6.022 × 10^{23} mol^{-1}, M_L is the molar mass of water and equals 1.805 × 10^{-2} kg/mol, ρ_L is the density of water, and equals 999.8 kg/m^3 at 273 K [262].

The heterogeneous Zeldovich factor, Z_{hete}, is derived by Vehkamäki et al. [250] and can be estimated as follows.

$$Z_{hete} = \frac{\sqrt{A\gamma_{IW} / \left(\pi k_B T_{int}\right)}}{3 i^{*\frac{2}{3}}} \cdot \sqrt{\frac{4}{2+\zeta}} \tag{6-42}$$

where i^* is the critical embryo size, A is the surface area of a water molecule, and ζ is defined as:

$$\zeta = \frac{\left(1 - X\cos\theta\right)\left[2 - 4X\cos\theta - \left(X^2\cos^2\theta - 3\right)\right]}{\left(1 - 2X\cos\theta + X^2\right)^{\frac{3}{2}}} \tag{6-43}$$

The critical embryo size i^* can be estimated as:

$$i^* = \left(\frac{r^* n_S}{3} \cdot A\right)^3 \tag{6-44}$$

where n_S is the number density of molecules in the solid and can be expressed as:

$$n_S = \frac{N_A \rho_S}{M_L} \tag{6-45}$$

where ρ_S is the density of ice and equals 916.2 kg/m^3 at 273 K [262]. The surface area of a water molecule, A_m, can be estimated by assuming the water molecule is spherical.

$$A_m = 4\pi r_{mean}^2 \tag{6-46}$$

where r_{mean} is the mean particle separation distance, which is related to n_S, and can be expressed as:

$$r_{mean} = \left(\frac{3}{4\pi n_S}\right)^{\frac{1}{3}} \tag{6-47}$$

Then the other factor in computing the nucleation rate J is F_D, which is the net rate of attachment to the critical nucleus. This rate can be estimated as [246]:

$$F_D = \left(A \cdot i^{*\frac{2}{3}} \cdot n_L^{\frac{2}{3}} \right) \cdot \left(D \cdot n_L^{\frac{2}{3}} \right) \tag{6-48}$$

where the term in the bracket is the number of surface molecules of the critical nuclei, and the other term in the second bracket is the impact rate of liquid molecules per surface molecule of the embryo. In the second term, D is the self-diffusion coefficient of water and can be estimated as [264]:

$$D = D_0 \exp\left[\frac{-1}{T_B \left(T_{int} - T_0 \right)} \right] \tag{6-49}$$

where $D_0 = 4$ m^2/s, $T_B = 2.07 \times 10^{-3}$ K, $T_0 = 169.7$ K.

By substituting Eqs. (6-35), (6-42), and (6-48) in Eq. (6-32), the nucleation rate J can be rewritten as:

$$J = n_L^{\frac{7}{3}} \cdot \frac{\sqrt{A\gamma_{IW} / \left(\pi k_B T_{int} \right)}}{3} \cdot \sqrt{\frac{4}{2+\zeta}} \cdot A \cdot D \cdot \exp\left[-\frac{\frac{8\pi\gamma_{SL}}{3\left(\Delta G_V\right)^2} f\left(\cos\left(\theta\right), X \right)}{k_B T_{int}} \right] \tag{6-50}$$

Hence, the nucleation starts when the number of critical nuclei N reaches 1 in the subcooled droplet, and for a low cooling rate, N can be estimated as [235,251]:

$$N = \int_0^{t_n} \left(V_D - V_c \right) \cdot J dt \tag{6-51}$$

where V_D is the initial droplet volume, J is the nucleation rate, V_c is the size of the critical nucleus. If it assumes that the nucleus is spherical, it can be estimated as follows:

$$V_c = \frac{4}{3} \pi r^{*3} \tag{6-52}$$

In summary, both J and V_c are related to the interface temperature T_{int} (t) calculated in the liquid supercooling stage and a function of t. The time from droplet impact on the substrate surface to the time when N approximately reaches 1, is defined as nucleation t_n, which means that the liquid droplet takes time t_n to start freezing, and T_n is defined as T_{int} (t_n) at time t_n. In this study, the droplet size is about 18.07 ± 0.51 µl. The assumption of a single critical nucleus formed as the sign of the beginning of nucleation is reasonable and is also approved by others [208,260].

After the critical nucleus is formed, the ice embryo starts to crystalline growth at a very short time scale (less than 0.1 s) [121,191–193,208,218,247], which is also known as the recalescence stage. As discussed in section 6.1, to simplify the analysis of the freezing process, the time for the recalescence stage is assumed to be zero, $t_r \approx 0$ s. During this process, the temperature of the droplet increases dramatically to the equilibrium freezing temperature T_m. The equilibrium solidification stage begins after the temperature jumps back from the nucleation temperature to the melting/freezing temperature, which is discussed in section 6.4.3.

6.4.3 Equilibrium solidification stage

The droplet will become opaque at some point, indicating the beginning of the equilibrium solidification stage [90]. This phenomenon was also observed in previous experiments in this study. Other researchers in the literature have also reported the same phenomenon and marked this as the end of the nucleation and recalescence stage [208,265,266]. The classical freezing and melting problems are discussed by applying the Stefan problem [256]. In this analysis, the droplet impact temperature is higher than the melting/freezing temperature. The 1-D Stefan problem is used to address the solidification time t_s during the equilibrium solidification stage, which can also simplify the analysis process and decrease the computing power consumed. The following assumptions are adopted to tackle the problem:

1. The densities of both phases are the same and keep at constant, which also means that the volume change due to the solidification is neglected.
2. The heat conduction equation governs the temperature distribution and heat transfer.
3. The temperature of the interface is known, which is the nucleation temperature T_n calculated in section 6.4.2.
4. A clear interface between the two phases can be considered, which can also be observed in the previous experimental study in Figure 5-3.

After the recalescence stage, the initial temperature of the droplet is assumed to be the same as the melting/freezing temperature T_m. Hence, the Stefan problem is a one-region problem that focuses on solving the temperature distribution in the solid phase, and this treatment can also be found in the literature [246].

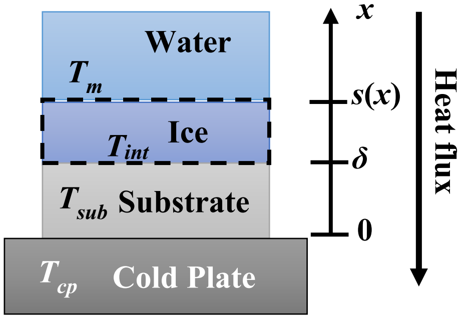

Figure 6-4 Schematic of the 1-D one-region Stefan problem in the equilibrium solidification stage

In this one-region Stefan problem, the temperature distribution in the solid phase is controlled by heat conduction, as shown in Figure 6-4. The interface moved upwards, the location of which is a function of time, $s(t)$. The governing equation is as follows.

$$\frac{\partial^2 T}{\partial x^2} = \frac{1}{\alpha_s} \cdot \frac{\partial T}{\partial t} \tag{6-53}$$

where α_s is the thermal diffusivity of the solid phase. The interface locates initially at the interface between the substrate surface and the droplet, where it is set as the position $x = 0$. Therefore, the initial conditions are as follows.

$$\begin{aligned} &T(x,0) = T_m \\ &s(0) = 0 \end{aligned} \tag{6-54}$$

The corresponding boundary conditions are:

$$\begin{aligned} &T(0,t) = T_{int} \\ &T(x,t) = T_m \text{ , at } x = s(t), t > 0 \\ &k_S \frac{\partial T}{\partial x} = \rho H_{SL} \frac{ds}{dt} \text{ , at } x = s(t), t > 0 \end{aligned} \tag{6-55}$$

where H_{SL} is the latent heat of fusion, ρ is the density of water, k_S is the thermal conductivity of the solid phase (ice). An exact solution can be derived by introducing a similarity variable $x/\sqrt{t}$ into the governing equation. The movement of the solid-liquid phase change interface can be estimated as follows:

$$s(t) = 2\lambda\sqrt{\alpha_s t} \tag{6-56}$$

where λ is a constant determined by the temperature difference between T_{int} and T_m, and can be obtained by solving the following equation iteratively.

$$\frac{Ste_S}{\sqrt{\pi}} = \lambda \cdot \exp\left(\lambda^2\right) \cdot erf\left(\lambda\right) \tag{6-57}$$

where Ste_S is the Stefan number for the solid phase and is expressed as:

$$Ste_S = \frac{c_{p,s}\left(T_m - T_{\mathrm{int}}\right)}{H_{SL}} \tag{6-58}$$

where $c_{p,\,s}$ is the specific heat capacity of the solid phase (ice). After solving the interface movement, the temperature profile in the solid phase is expressed as:

$$T\left(x,t\right)=T_{\text{int}}+\frac{erf\left(\dfrac{x}{2\sqrt{t}}\right)}{erf\left(\lambda\right)} \tag{6-59}$$

The interface location function s(t) describes the movement of the interface. In order to find the solidification time at the equilibrium solidification stage, the freezing depth, *s*, is introduced, which is defined as when the interface moved to the location of the freezing depth, the liquid droplet is completely solidified. The freezing depth is not the height of the droplet on a substrate surface but the projected area (A_p) of the droplet on the plane, which is normal to the substrate surface, divided by the final contact diameter (D_c) of the droplet. The freezing depth can be expressed as follows.

$$s=\frac{A_p}{D_c} \tag{6-60}$$

Hence, the solidification time t_s can be estimated as:

$$t_s=\frac{\left[A_p/\left(2\lambda D_c\right)\right]^2}{\alpha_s} \tag{6-61}$$

where the final contact diameter (D_c) can be estimated in section 6.3.

In summary, the solidification time (t_s) is given by Eq. (6-56). The total freezing delay time per unit of mass can be estimated by adding the time during each stage discussed above and then dividing it by the mass of the droplet.

$$t_{freezing,m}=\frac{t_{freezing}}{m}=\frac{t_n+t_r+t_s}{m}=\frac{t_n+t_s}{m} \tag{6-62}$$

6.4.4 Solid subcooling stage

Suppose the ice droplet is still attached to the substrate surface after the whole droplet is completely solidified. In that case, the droplet will continue to be cooled to a state until it reaches equilibrium with the substrate surface temperature. The heat conduction equation controls this stage, and

$$\frac{\partial^2 T_{sub}}{\partial x^2} = \frac{1}{\alpha_{sub}} \cdot \frac{\partial T_{sub}}{\partial t} \text{ in the substate domain } 0 < x \le \delta \quad (6\text{-}63)$$

$$\frac{\partial^2 T_I}{\partial x^2} = \frac{1}{\alpha_I} \cdot \frac{\partial T_I}{\partial t} \text{ in the substate domain } x \ge \delta \quad (6\text{-}64)$$

subject to the boundary conditions as follows.

$$\begin{cases} T_{sub}\left(0,t\right) = T_{cp} \\ T_I\left(\delta,t\right) = T_{sub}\left(\delta,t\right) \\ T_I\left(\infty,t\right) = T_m \\ T_{sub}\left(\delta,0\right) = T_I\left(x,0\right) = T_m \text{ at } x \ge \delta \end{cases} \quad (6\text{-}65)$$

By solving the governing equation, the temperature profile in the substrate and ice droplet can be expressed as:

$$T_{sub}\left(x,t\right) = T_m + \left(T_{cp} - T_m\right) erfc\left(\frac{x}{2\sqrt{\alpha_{sub} t}}\right) \quad \left(0 < x \le \delta\right) \quad (6\text{-}66)$$

$$T_I\left(x,t\right) = T_m + \left(T_{cp} - T_m\right) \frac{erfc\left(\frac{\delta}{2\sqrt{\alpha_{sub} t}}\right)}{erfc\left(\frac{x}{2\sqrt{\alpha_I t}}\right)} erfc\left(\frac{x}{2\sqrt{\alpha_I t}}\right) \quad \left(x \ge \delta\right) \quad (6\text{-}67)$$

6.5 Results and discussion

When the analytical results are compared with the experimental results, the critical energy barrier required for nucleation on hydrophobic surfaces is overestimated. The shape factor *f* in Eq. (6-35) is insufficient to predict the critical Gibbs free energy change for heterogeneous ice nucleation. Other factors may influence the critical energy barrier, such as contact angle, surface material and roughness, and environmental conditions (e.g., dust size and humidity). Due to the overestimated critical free energy change, the nucleation rate is reduced, resulting in a relatively longer nucleation time than the experimental results from Chapter 5. In order to correct the critical Gibbs free energy change, a coefficient is introduced to modify the critical energy barrier. It is a function of the apparent static contact angles of the water droplets on a solid surface by fitting the experimental results with the analytical model. This coefficient is defined as C_A and expressed as follows.

$$C_A = 0.32 + 0.2 \cdot e^{3.8 \cdot \cos(\theta)} \tag{6-68}$$

Therefore, the nucleation rate J can be rewritten by substituting Eq. (6-68) into Eq. (6-32) as follows.

$$J = n_L Z_{hete} F_D \exp\left(-\frac{C_A \Delta G^*_{hete}}{k_B T_{int}} \right) \tag{6-69}$$

Table 6-1 The physical, molecular and thermal properties of water and ice at 273 K [262,264].

Property		Unit	Water	Ice
Density	ρ	[kg/m^3]	999.8	916.2
Thermal conductivity	k	[W/(m·K)]	0.555	2.22
Specific heat	c_p	[J/(kg·K)]	4200	2100
Interfacial surface tension	γ_{SL}	[J/m^2]	$0.028 + 0.00025 \times (T - 273.15)$	
Latent heat of fusion	H_{SL}	[J/kg]	3.34×10^5	

This coefficient depends on the applications and may vary due to environmental and experimental conditions. Also, this coefficient is not only related to the contact angle, but may also be related to different circumstances, such as surface material and roughness and environmental conditions (e.g., dust, humidity).

Since the surface defects can be used as the nucleating particles, the sizes of the nucleating particles used in this model are adopted for the surface roughness and listed in Table 6-2. By substituting the properties in Table 6-1, Table 6-2 and the experimental conditions in Table 5-3, and Table 5-4, the total freezing delay time per unit mass can be obtained and illustrated with experimental results in Figure 6-5. It shows that the analytical prediction has good agreement with the experimental results, which verifies the feasibility of the methods and assumptions used in this study. The analytical consideration not only provides a straightforward and effective solution but also simplifies the rather complicated mechanism of the phase change heat transfer process for droplet impact and freezing on metal surfaces and provides a direct estimate of the freezing delay time for the corresponding conditions (impact conditions, temperature, wettability, surface roughness), which is beneficial for engineering applications. This model reduces the requirement for extensive and complex computations, resulting in a fast and effective method for understanding and estimating the droplet impact and freezing process.

Table 6-2 The sizes of nucleating particles adopted for the surface roughness [267].

Sample	R_p [m]
ON	4.62×10^{-6}
100S	8.27×10^{-6}
250S	11.93×10^{-6}
ED-SA	19.89×10^{-6}
100S-ED-SA	21.64×10^{-6}
250S-ED-SA	23.38×10^{-6}

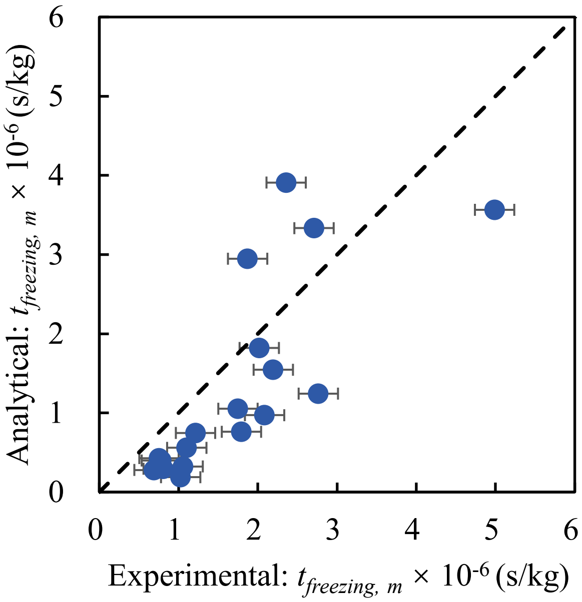

Figure 6-5 The comparison of calculated total freezing delay time per unit mass with the experimental results.

The droplet impact temperature is set at 5 °C, and the cooling plate is connected to a thermal bath, the circulating temperature of which is set at -15 °C. The droplet sizes are adopted from the experiments. The droplet experiences five freezing stages: the liquid supercooling stage, the nucleation stage, the recalescence stage and the solid subcooling stage. The time from the end of the recalescence stage to the droplet frozen completely is defined as the solidification time, t_s. The freezing delay time is the sum of the nucleation and solidification time. Figure 6-6 illustrates the temperature profiles of the ice-water interface of a sessile droplet on the six samples tested in Chapter 5.

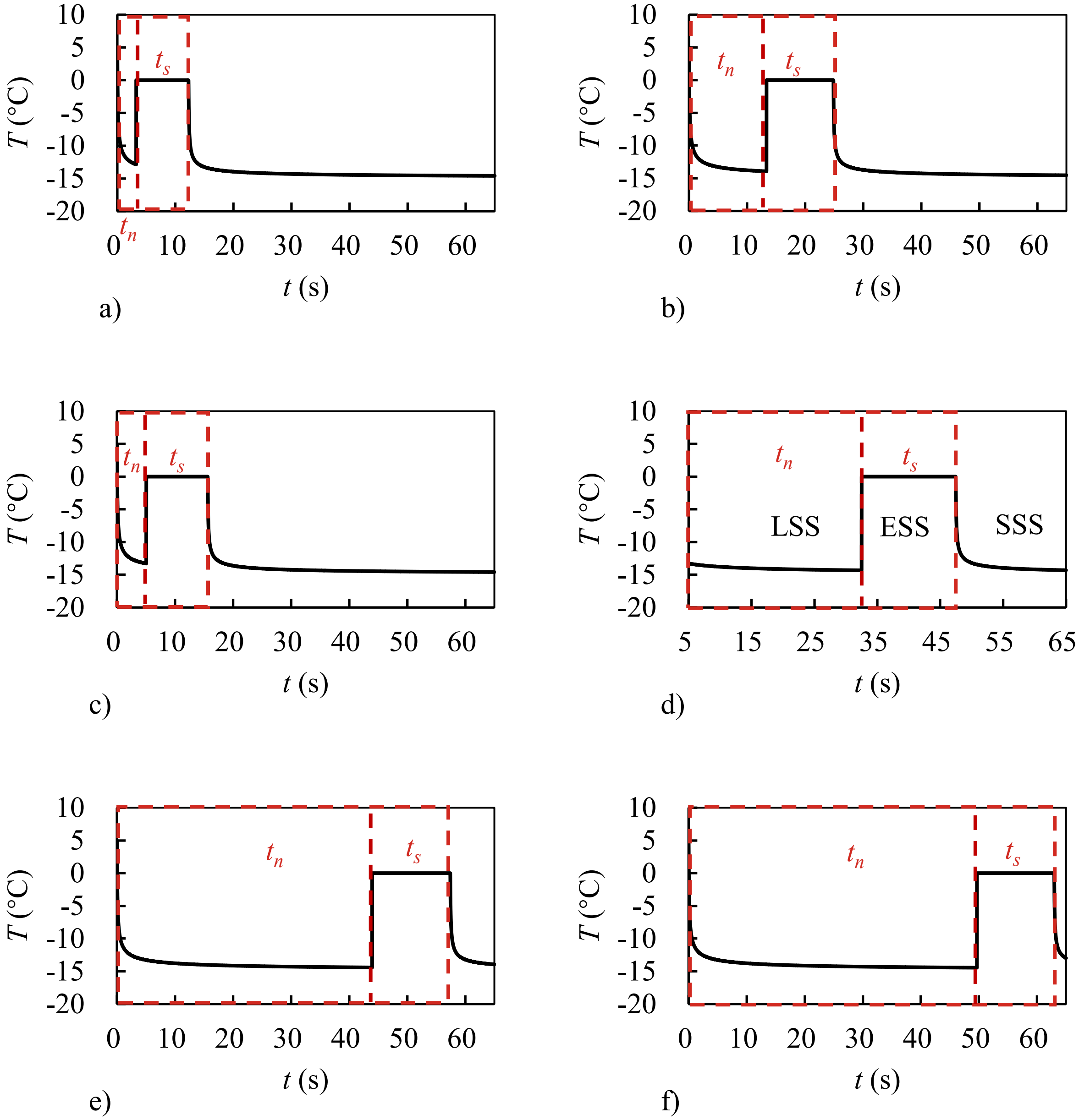

Figure 6-6 The temperature profile of the ice-water interface (when the impact height h = 0 cm, the T_{impact} = 5 °C, T_{cp} = -15 °C): a) ON, b) 100S, c) 250S, d) ED-SA, e) 100S-ED-SA, f) 250S-ED-SA, where t_n is the nucleation time, t_s is the solidification time, and LSS, ESS, SSS stands for liquid supercooling stage, equilibrium solidification stage and solid subcooling stage, respectively. The red dashed boxes indicate the equilibrium solidification stage, and the left boundary represents the nucleation and the recalescence stage.

Besides the sessile droplet freezing process, Figure 6-7 illustrates the temperature profiles of the ice-water interface at different impact heights. The nucleation time is affected by the impact height, and a higher impact height contributes to faster ice nucleation in the droplet. In comparison, it has less influence on the solidification time. However, the droplet size still is the most significant factor in the solidification time since the droplet size for h = 10 cm is the largest among the other two cases.

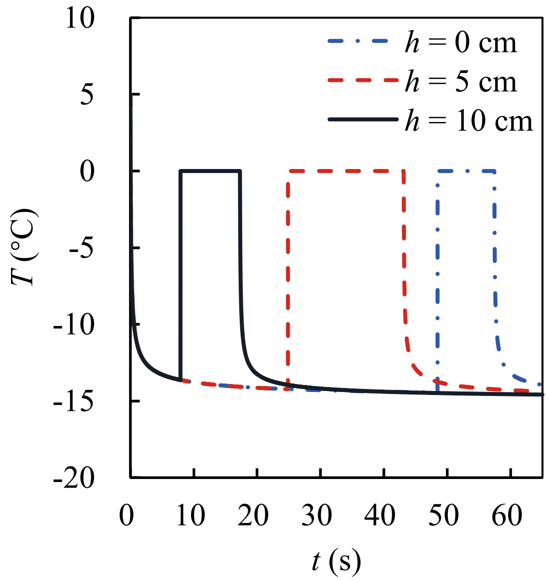

Figure 6-7 The temperature profile of the ice-water interface of a water droplet on the 100S-ED-SA surface with different impact heights, when the T_{impact} = 5 °C, T_{cp} = -15 °C, $R_p = 21.64 \times 10^{-6}$ m, $D_{c,\, h = 0\text{ cm}} = 2.38 \times 10^{-3}$ m, $V_{D,\, h = 0\text{ cm}} = 1.29 \times 10^{-8}$ m^3, $D_{c,\, h = 5\text{ cm}} = 3.79 \times 10^{-3}$ m, $V_{D,\, h = 5\text{ cm}} = 2.22 \times 10^{-8}$ m^3, $D_{c,\, h = 10\text{ cm}} = 3.24 \times 10^{-3}$ m, $V_{D,\, h = 10\text{ cm}} = 1.39 \times 10^{-8}$ m^3.

Also, as mentioned in 5.4, when the impact height is 10 cm, the droplet will partially bounce off the superhydrophobic surface. That part does not fall back into the original droplet, which contributes to an even smaller droplet size when it freezes on the surface. Therefore, the analytical results show that the solidification time $t_{s,\,h\,=\,10\text{ cm}} < t_{s,\,h\,=\,0\text{ cm}} < t_{s,\,h\,=\,5\text{ cm}}$ for sample 100S-ED-SA.

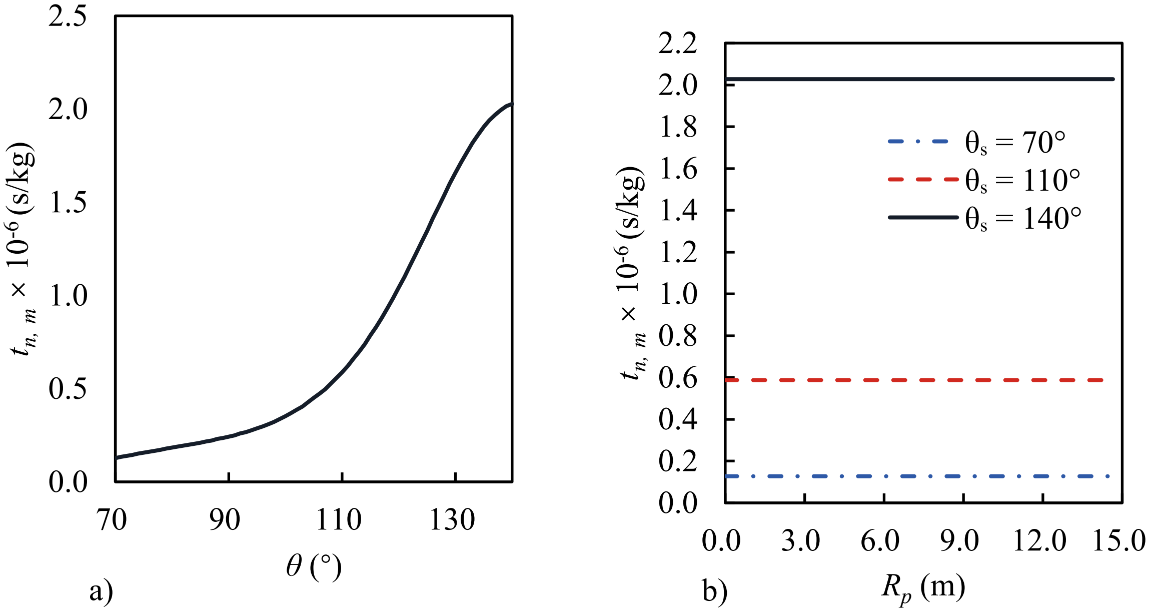

Figure 6-8 The effects on the nucleation time per unit of mass of a 20 μl water droplet impact on a substrate surface: a) the contact angle θ_s, when the T_{impact} = 5 °C, T_{cp} = -15 °C, $R_p = 14.96 \times 10^{-6}$ m, b) the size of nucleating particles, when the T_{impact} = 5 °C, T_{cp} = -15 °C.

In summary, surface wettability affects the nucleation time. A hydrophobic surface contributes to a much longer freezing delay, and the results are represented in Figure 6-8a. For hydrophobic surfaces ($\theta_s > 90°$), the nucleation time per unit mass increases significantly when the contact angle increases. In contrast, for hydrophilic surfaces ($\theta_s < 90°$), the nucleation time per unit mass slightly increases when the contact angle increases. While in the analytical model, the size of the nucleating particle is another factor that can influence the nucleation rate. However, this effect is negligible for nucleation time per unit mass, as shown in Figure 6-8b. The nucleation time per unit of mass does not change in the condition of three different droplet-substrate contact angle surfaces (70°, 110°, 140°).

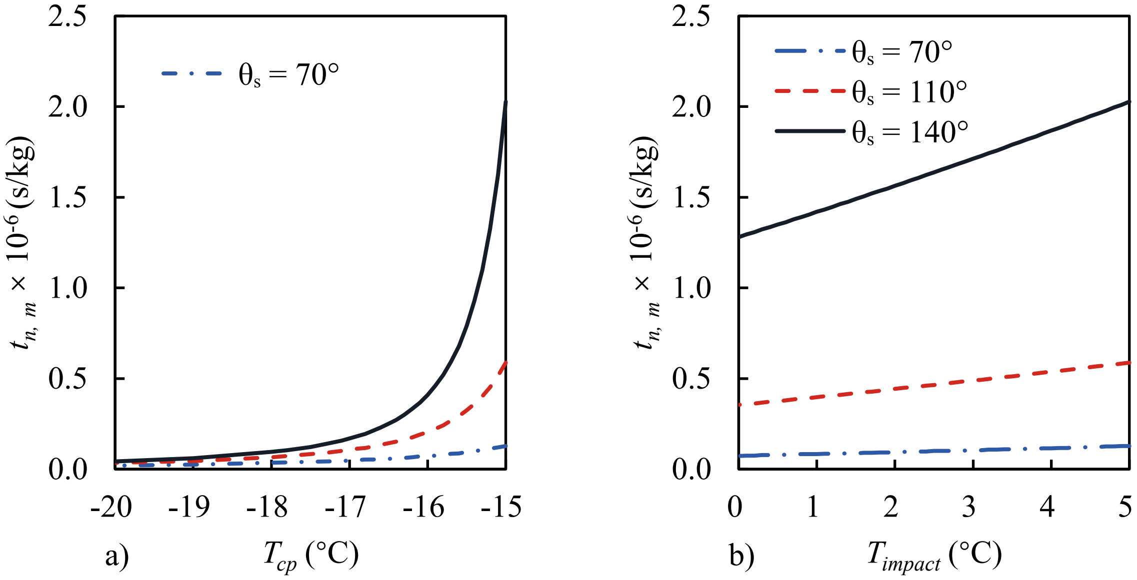

Figure 6-9 The effects on the nucleation time per unit of mass of a 20 μL water droplet impact on a substrate surface: a) the temperature of the cold plate, when the T_{impact} = 5 °C, $R_p = 14.96 \times 10^{-6}$ m; b) the droplet impact temperature, when T_{cp} = -15 °C, $R_p = 14.96 \times 10^{-6}$ m.

Other factors that influence the droplet nucleation time per unit mass are also investigated, such as the temperature of the droplet when it impacts the surface and the temperature of the substrate (or ambient temperature). The variation of nucleation time per unit mass, along with the droplet impact temperature and the cold plate temperature, is shown in Figure 6-9. On the one hand, the cold plate temperature decreases, leading to a shorter nucleation time per unit mass for both hydrophilic and hydrophobic surfaces. Especially within the temperature between -15 °C and -17 °C, the effect of cold plate temperature on nucleation time per unit mass becomes weaker as the temperature decreases. In addition, the nucleation time per unit mass is higher when the droplet-substrate contact angle is larger. On the other hand, the droplet impact temperature decreases, leading to quicker nucleation of the droplet, and this effect is also more significant for surfaces with higher contact angles.

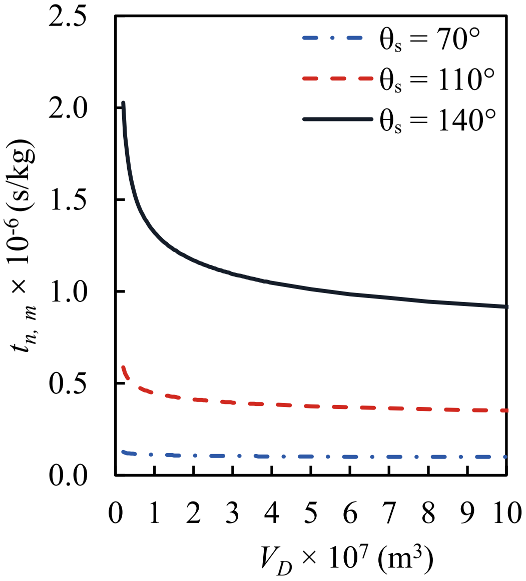

Figure 6-10 The effect of the volume of the droplet V_D on the nucleation time per unit mass of a droplet impact on a substrate surface when the T_{impact} = 5 °C, T_{sub} = -15 °C, $R_p = 14.96 \times 10^{-6}$ m.

In addition, the nucleation time per unit mass is also influenced by droplet volume (V_D), as shown in Figure 6-10. When the water-solid surface contact angle is 140°, $t_{n,\ m}$ decreases dramatically as V_D increases in the region where droplet volume is less than 3.0×10^{-8} m^3. However, as droplet volume continues to increase, the change in $t_{n,\ m}$ tends to level off, and the effect strength of the droplet volume becomes weaker as the contact angle decreases.

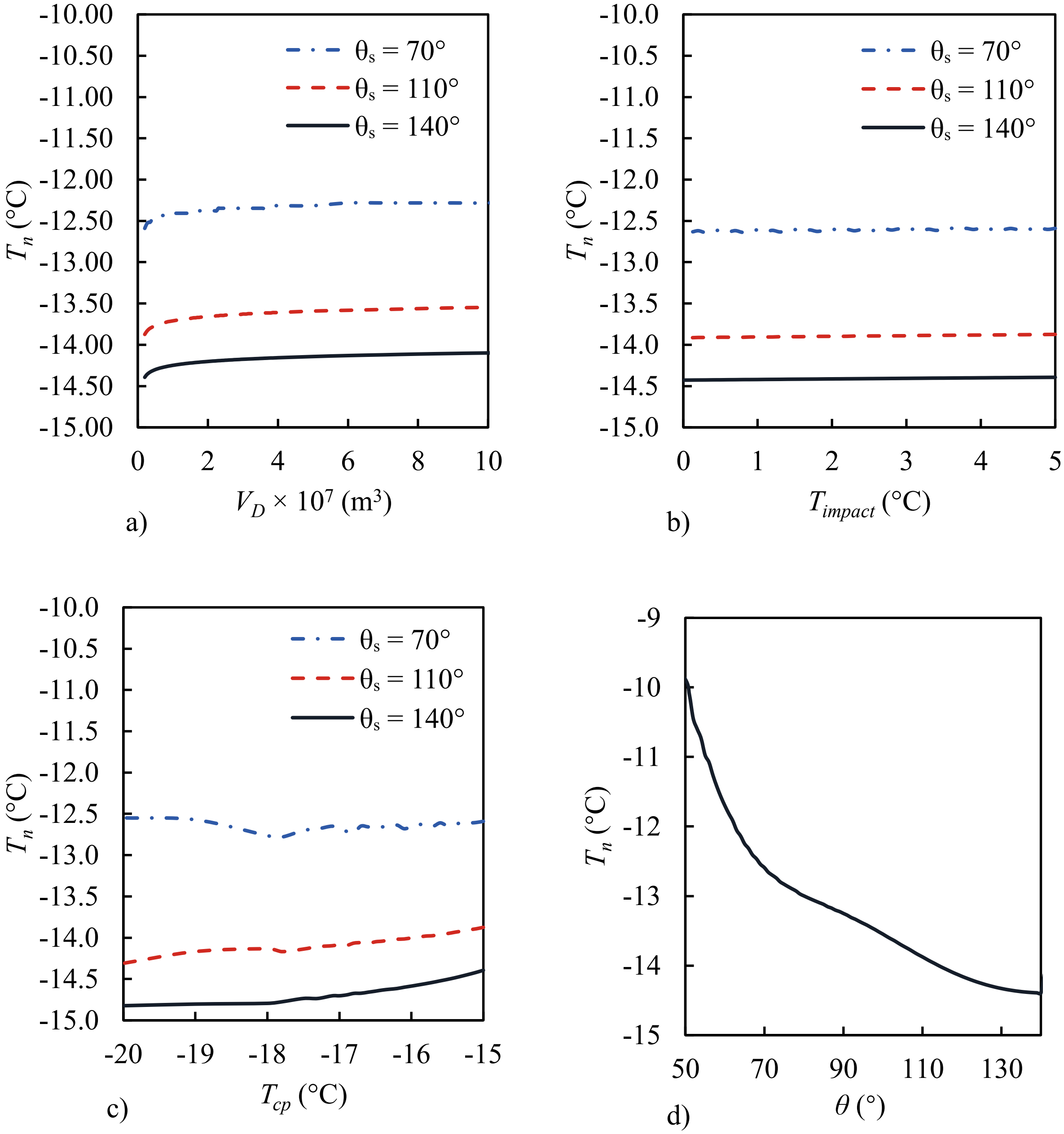

Figure 6-11 a) The effect of the droplet volume V_D on the nucleation temperature when the droplet impacts a substrate surface, when the T_{impact} = 5 °C, T_{cp} = -15 °C, $R_p = 14.96 \times 10^{-6}$ m. The effects on the nucleation temperature of a 20 µl water droplet impact on a substrate: b) the cold plate temperature (T_{impact} = 5 °C, $R_p = 14.96 \times 10^{-6}$ m); c) the droplet impact temperature (T_{cp} = -15 °C, $R_p = 14.96 \times 10^{-6}$ m), and d) the contact angle θ_s (T_{impact} = 5 °C, T_{cp} = -15 °C, $R_p = 14.96 \times 10^{-6}$ m.)

Furthermore, the nucleation temperature is defined as the droplet-substrate interface temperature at the time of nucleation, which can be estimated by substituting the nucleation time, t_n, into Eq. (6-31). In comparison, the nucleation temperature is affected by the contact angle, the cold plate temperature, the droplet impact temperature, and the droplet volume. The relationship between these factors and the nucleation temperature is illustrated in Figure 6-11. The factors of droplet impact temperature, cold plate temperature and droplet volume have relatively insignificant effects on the nucleation temperature. Except for very small droplets ($\sim 10^{-8}$ m^3), changes in droplet volume will slightly affect the nucleation temperature of the droplet. However, this effect is only in the range of approximately 0.10 °C to 0.20 °C, which is negligible. The nucleation temperatures for different droplet volumes in the range between 2.00×10^{-8} m^3 to 1.00×10^{-5} m^3 are approximate at -12.36 °C ± 0.09 °C, -13.64 ± 0.09 °C and -14.19 ± 0.08 °C for the contact angle at 70°, 110° and 140°, respectively as shown in Figure 6-11a. Also, for a 20 µl water droplet impact on a substrate surface, the nucleation temperature for different impact temperatures in the range between 5 °C to 0 °C are approximate -12.61 °C ± 0.01 °C, -13.89 ± 0.01 °C and -14.41 ± 0.01 °C for the contact angle at 70°, 110° and 140°, respectively as shown in Figure 6-11b. At the same time, the nucleation temperatures for a 20 µl water droplet impact on substrates having different temperatures in the range between -15 °C to -20 °C are approximate -12.65 °C ± 0.05 °C, -14.04 ± 0.10 °C and -14.62 ± 0.12 °C for the contact angle at 70°, 110° and 140°, respectively as represented in Figure 6-11c. In summary, these three factors have insignificant effects on the nucleation temperature, while the contact angle is the main factor that governs the nucleation temperature, which is illustrated in Figure 6-11d. The nucleation temperature gradually decreases as the contact angle increases.

6.6 Summary

In this study, the droplet impact and freezing process have been investigated analytically. When a water drop impacts a surface in a cold environment, this droplet will experience six stages: dynamic stage, supercooling stage, nucleation stage, recalescence/dendritic stage, equilibrium solidification stage and solid subcooling stage. The dissipation in the droplet dynamic stage was analyzed based on the energy conservation, which results in a solution for droplet final contact diameter (D_c) as a function of initial droplet diameter (D_i), the Weber number We, the Reynolds number Re, and contact angle θ. The final contact diameter (D_c) is critical for heat transfer and droplet solidification time.

The droplet freezing process has been divided into the liquid supercooling stage, the nucleation and recalescence stage, the equilibrium solidification stage and the solid subcooling stage. The liquid supercooling and solid subcooling stages are based on the 1-D transient heat conduction theory to obtain the interface temperature as a function of time. When the number of ice nuclei reaches one, nucleation occurs, and the recalescence stage begins by coupling the liquid supercooling 1-D transient heat conduction with the classical nucleation theory. The time consumed is recorded as the nucleation time, and the corresponding temperature is the nucleation temperature. After the recalescence stage, the droplet temperature increases to the melting/freezing temperature due to the latent heat release.

By coupling the droplet dynamic results, D_c, with the one-region Stefan problem, the model estimates the solidification time for the equilibrium solidification stage. Then the solid subcooling stage begins.

The experimental results validate the analytical predictions, which verify the feasibility of the methods and assumptions used in this study. The analytical consideration not only provides a straightforward and valid solution but also simplifies the rather complicated mechanism of the droplet dynamic and freezing process on metal surfaces and provides a directly estimated total freezing delay time under the different conditions (impact conditions, temperature, wettability, surface roughness), which is beneficial for engineers and reduces the requirement for extensive and sophisticated computations, resulting in a fast and effective method for understanding and estimating the droplet impact and freezing process, which has also filled the gap in this research.

From this analytical consideration, the following conclusion can be obtained:

1. The final contact diameter (D_c) in the droplet dynamic stage is related to the initial droplet diameter (D_i), the Weber number We, the Reynolds number Re, and the contact angle θ.
2. The solidification time (t_s) in the equilibrium solidification stage depends on the final contact diameters (D_c), the droplet sizes (V_d) and the nucleation temperature (T_n).
3. The effect on nucleation time (t_n) of the size of nucleating particles is negligible.
4. The impact height affects nucleation time (t_n). In other words, a higher impact height contributes to slower ice nucleation in the droplet.
5. The nucleation time (t_n) increases significantly for hydrophobic surfaces, while it slightly increases for hydrophilic surfaces when the contact angle increases.
6. The lower cold plate temperature leads to a shorter nucleation time (t_n) for both hydrophilic and hydrophobic surfaces. However, the effect becomes weaker as the temperature decreases. Also, the nucleation time (t_n) is higher when the droplet-substrate contact angle is more significant at the same cold plate temperature
7. The lower droplet impact temperature contributes to quicker nucleation of the droplet, which is more significant for surfaces with higher contact angles.

8. The contact angle is the main factor that governs the nucleation temperature compared with the effects of droplet impact temperature, cold plate temperature and droplet volume.

Chapter 7 Conclusion and Recommendations for Future Work

7.1 Conclusions

A surface with low surface energy to repel water and prevent icing is a passive ice protection technique. This study comprehensively investigates the droplet wetting behaviour, impact dynamics and freezing process on irregularly roughened stainless steel surfaces with various wettability. The combination of electrodeposition and sandblasting significantly increases the static contact angle, from 91 ± 6° (ON) to 151 ± 2 (100S-ED-SA), and both techniques can be used on an industrial scale. This comprehensive investigation contributes to the following critical conclusions:

1. The droplet dynamic experimental results illustrate the common problems involved in studying wetting dynamics on random rough surfaces, a topic of great relevance to large-scale industrial wetting applications and great importance in the life cycle of materials. For droplets on inclined experiments of the same irregular rough surface, almost all droplets adhered to these surfaces even though the contact angle was in a superhydrophobic state (~150°). This result could not have been explained by the simple Furmidge model that relates sliding angles to volume-modified contact angles. These difficulties were not limited to the sandblasted and coated steel: the wetting behaviour of other roughened metals and plastics showed similar problems with pinning.
2. The results of water droplet freezing on the target surfaces indicate that a further reduced wettability leads to a longer freezing delay. The freezing delay performance of sandblasted samples is better than the one without sandblasting pre-treatment. Also, the

surface treated by the hybrid technique (sandblasting and electrodeposition) presents a longer freezing delay than those treated with only one technique.

3. Most of the time (>98% of the total freezing delay time) in the freezing delay experiments, the droplet is stationary on the surface, and there is a fixed droplet-substrate contact area, which results in a fundamental assumption that a fixed final contact area can be assumed for the freezing process.
4. The heat transfer analysis for the freezing delay experiments demonstrates that a higher water contact angle contributes to a lower droplet-substrate final contact area resulting in a lower freezing rate and longer freezing delay time. The higher impact distance will also lead to a larger final contact area of the water droplet on the sample surface, contributing to a higher freezing rate and shorter freezing delay time.
5. The dimensional analysis indicates that lower We_i (due to lower impact velocity or a poorer wetting surface) leads to smaller A_c^* (smaller final contact area A_c) and a lower average freezing rate per unit mass. In other words, for droplets with the same impact velocity, a more hydrophobic surface will have a smaller final contact area, contributing to a longer freezing delay and a lower average freezing rate per unit mass. At the same time, the higher impact distance will result in a larger dimensionless final contact area A_c^* and a higher average freezing rate per unit mass, which leads to faster freezing (smaller t^*).
6. The droplet impact height has less influence on the final contact area per unit mass $A_{c,\,m}$ and the average heat transfer rate per unit mass $\overline{q}_m$ of a droplet on a more hydrophobic surface. In other words, the superhydrophobic surfaces have better icephobic performance,

even for a droplet falling from a higher distance. This finding is significant in addressing engineering icing problems.

7. From this analytical consideration, the following conclusion can be obtained: (1) the final contact diameter (D_c) in the droplet dynamic stage is related to the initial droplet diameter (D_i), the Weber number We, the Reynolds number Re, and contact angle θ and the solidification time (t_s) in the equilibrium solidification stage depend on the final contact diameters (D_c), the droplet sizes (V_D) and the nucleation temperature (T_n); (2) the nucleation time (t_n) depends on droplet-substrate contact angles (θ_s), impact heights, cold plate temperature (T_{cp}), droplet impact temperature (T_{impact}), and droplet volume (V_D), while the effect of the nucleating particle sizes (R_p) is negligible; (3) the droplet-substrate contact angle (θ_s) is the main factor that governs the nucleation temperature (T_n) compared with the effects of droplet impact temperature (T_{impact}), cold plate temperature (T_{cp}) and droplet volume (V_D).

7.2 Contributions

This comprehensive study on wettability, droplet impact dynamics and the freezing processes have built the relationship between surface wettability and icephobicity. The droplet impact and freezing process have been investigated, which benefit the research in this field:

1. The hybrid fabrication method (sandblasting and electrodeposition) can be applied to a large-scale industrial surface treatment. The treated surface presents superhydrophobicity and good wetting durability after multiple icing and melting cycles.
2. The droplet wetting behaviour on random rough surfaces proposes the problems involved in studying wetting dynamics on large-scale industrial irregularly roughened surfaces. Some recommendations for future study have been listed in section 7.3.

3. The droplet freezing delay experiment connects droplet impact dynamics and the freezing delay process, which fills the gap in the literature for experiments conducted on metal surfaces in subfreezing environments. Also, the critical effects of the final contact area and the assumption of a fixed droplet-substrate contact area can be used by other researchers or engineering in the applications.
4. The analytical framework not only provides a straightforward and effective solution but also simplifies the rather complicated mechanism of the phase-change heat transfer process for droplet impact and freezing on metal surfaces and provides a direct estimate of the freezing delay time for the corresponding conditions (impact conditions, temperature, wettability, surface roughness), which is beneficial for engineering applications.

7.3 Recommendations for future work

This study is a fundamental investigation of surface wettability, droplet impact dynamics and the freezing process on randomly roughened metal surfaces, which can improve understanding of the relationship between surface wettability and retarded icing. However, there are some inadequacies and limitations, so the following recommendations are proposed to guide future work.

1. The following best practices are recommended for future studies involving the assessment of surface contact angles: (1) report dynamic advancing and receding contact angles since apparent static contact angles are insufficient; (2) include images of the droplets and their fits to show how droplet asymmetry was addressed. By reporting the data mentioned above, future researchers can compare wettability studies in a more informed way. These conclusions are relevant not only for metals but also could be applied to studies of other coated solid surfaces.

2. This research has not investigated the surface roughness for surface wettability since the target surface was roughened irregularly. Therefore, more investigation can be done to evaluate the effects of surface roughness on surface wettability.
3. Ice adhesion has not been considered and investigated in this research, which can be investigated in future studies.
4. Similar droplet impact and freezing delay experiments have been conducted at room temperature, presented in Appendix A. Both investigations lead to similar conclusions. The ambient temperature can be controlled in this study. However, the effects of other environmental conditions on the droplet impact dynamics and freezing process require future investigation, for example, the ambient air velocity and humidity.
5. Another comprehensive investigation related to ice protection techniques has been presented in Appendix B. It is difficult to achieve adequate ice protection in harsh environments with a single active or passive technique based on extensive studies. The cost of implementation and maintenance for active anti/de-icing approaches is too high for long-term use. Some passive ice protection techniques can delay icing, but they cannot prevent long-term ice formation completely, which leads to the eventual rapid accumulation of ice. The hybrid techniques combine multiple active and passive methods to take advantage of both techniques; for example, the electrothermal air film isolating surfaces and electrothermal SLIPS. Still, the application of these techniques is limited due to the potential of electrical shock hazards in offshore environments. There are more options for combining active and passive techniques or passive and passive techniques; for example, PCMs/PSLs integrated with SLIPS, where the combination of two passive anti/de-icing approaches presents excellent anti-icing performance. The photothermal

technique integrated with air/ oil film isolating surfaces is promising but with limitations for different applications. Further investigation is required for the development and application of hybrid techniques.

6. The analytical model not only provides a straightforward and valid solution but also simplifies the rather complicated mechanism of the droplet dynamic and freezing process on metal surfaces and provides a directly estimated total freezing delay time under the different conditions (impact conditions, temperature, wettability, surface roughness), which is beneficial for engineers and reduces the requirement for extensive and sophisticated computations, resulting in a fast and effective method for understanding and estimating the droplet impact and freezing process, which has also filled the gap in this research. However, the framework still has some limitations for contact angles higher than 150 ° or below 40°, and the estimated coefficient C_A requires more investigation to obtain a more precise prediction. In the future, a more comprehensive model framework can be developed to address the abovementioned limitations.

References

[1]G. Fortin, J. Perron, Wind Turbine Icing and De-Icing, in: 47th AIAA Aerospace Sciences Meeting Including The New Horizons Forum and Aerospace Exposition, American Institute of Aeronautics and Astronautics, Reston, Virigina, 2009: p. 274. https://doi.org/10.2514/6.2009-274.

[2]Civil Aviation Authority, Aircraft Icing Handbook, Lower Hutt, New Zealand, 2000. https://www.skybrary.aero/bookshelf/books/659.pdf (accessed July 8, 2021).

[3]Lasse. Makkonen, Atmospheric icing on sea structures, Reston, Virginia, 1987. http://hdl.handle.net/2027/mdp.39015032254453.

[4]O. Fakorede, Z. Feger, H. Ibrahim, A. Ilinca, J. Perron, C. Masson, Ice protection systems for wind turbines in cold climate: characteristics, comparisons and analysis, Renewable and Sustainable Energy Reviews. 65 (2016) 662–675. https://doi.org/10.1016/j.rser.2016.06.080.

[5]C.C. Ryerson, Assessment of Superstructure Ice Protection as Applied to Offshore Oil Operations Safety: Problems, Hazards, Needs, and Potential Transfer Technologies, Erdc/Crrel Tr-08-14. (2008) 156. http://digitalcommons.unl.edu/usarmyresearch.

[6]H. Sojoudi, M. Wang, N.D. Boscher, G.H. McKinley, K.K. Gleason, Durable and scalable icephobic surfaces: Similarities and distinctions from superhydrophobic surfaces, Soft Matter. 12 (2016) 1938–1963. https://doi.org/10.1039/c5sm02295a.

[7]V. Bahadur, L. Mishchenko, B. Hatton, J.A. Taylor, J. Aizenberg, T. Krupenkin, Predictive model for ice formation on superhydrophobic surfaces, Langmuir. 27 (2011) 14143–14150. https://doi.org/10.1021/la200816f.

[8]Y. Yamada, T. Ikuta, T. Nishiyama, K. Takahashi, Y. Takata, Droplet nucleation on a well-defined hydrophilic-hydrophobic surface of 10 nm order resolution, Langmuir. 30 (2014) 14532–14537. https://doi.org/10.1021/la503615a.

[9]F. Khan, S. Ahmed, M. Yang, S.J. Hashemi, S. Caines, S. Rathnayaka, D. Oldford, Safety challenges in harsh environments: Lessons learned, Process Safety Progress. 34 (2015) 191–195. https://doi.org/10.1002/prs.11704.

[10]Loring Chien, Regarding offshore oil rigs, what does “harsh environment” mean and why is it important? - Quora, (2016). https://www.quora.com/Regarding-offshore-oil-rigs-what-does-harsh-environment-mean-and-why-is-it-important (accessed March 12, 2018).

[11]W. Maslow, E.R. de Jong, R.L.M. Demmer, Deicing composition, (2015).

[12]A. Gornik, K. Yosef, Mechanical vibration deicing system, 8517313, 2013.

[13]A.E. Charola, B. Rousset, C. Bläuer, Deicing Salts: An Overview, SWBSS 2017. (2017) 16.

[14]K. Nilssen, Ice Melting Capacity of Deicing Chemicals in Cold, NTNU, 2017.

[15]T. Rashid, H.A. Khawaja, K. Edvardsen, Review of marine icing and anti-/de-icing systems, Journal of Marine Engineering & Technology. 15 (2016) 79–87. https://doi.org/10.1080/20464177.2016.1216734.

[16]A. Gupta, M.R. Joshi, N. Mahato, K. Balani, Superhydrophobic Surfaces, in: Biosurfaces: A Materials Science and Engineering Perspective, 2015: pp. 170–200. https://doi.org/10.1002/9781118950623.ch6.

[17]M. Ran, C. Yang, Y. Fang, K. Zhao, Y. Ruan, J. Wu, H. Yang, Y. Liu, Model for rolling angle, Journal of Physical Chemistry C. 116 (2012) 8449–8455. https://doi.org/10.1021/jp210261b.

[18]A.R. Dehghani-Sanij, S.R. Dehghani, G.F. Naterer, Y.S. Muzychka, Sea spray icing phenomena on marine vessels and offshore structures: Review and formulation, Ocean Engineering. 132 (2017) 25–39. https://doi.org/10.1016/j.oceaneng.2017.01.016.

[19]T.S. Jorgensen, Influence of ice accretion on activity in the northern part of the Norwegian Continental Shelf, Offshore Technology Testing and Research Group, 1982.

[20]E.M. Samuelsen, K. Edvardsen, R. Grand Graversen, Modelled and observed sea-spray icing in Arctic-Norwegian waters, Cold Reg Sci Technol. 134 (2017) 54–81. https://doi.org/10.1016/j.coldregions.2016.11.002.

[21]K. Shi, X. Duan, A Review of Ice Protection Techniques for Structures in the Arctic and Offshore Harsh Environments, Journal of Offshore Mechanics and Arctic Engineering. 143 (2021). https://doi.org/10.1115/1.4050893.

[22]K.F. Jones, E.L. Andreas, Sea spray concentrations and the icing of fixed offshore structures, Quarterly Journal of the Royal Meteorological Society. 138 (2012) 131–144. https://doi.org/10.1002/qj.897.

[23]C.C. Ryerson, Ice protection of offshore platforms, Cold Reg Sci Technol. 65 (2011) 97–110. https://doi.org/10.1016/j.coldregions.2010.02.006.

[24]T. Tabata, Studies on the ice accumulation on ships III, Low Temperature Science, Series A, Physical Sciences. 27 (1969) 339–349.

[25]H.C. Shellard, The Meteorological Aspects of ice accretion on ships, Geneva, Switzerland, 1974. https://library.wmo.int/pmb_ged/wmo_397_en.pdf (accessed June 20, 2018).

[26]W.P. Zakrzewski, Icing of Fishing Vessels. Part I: Splashing a Ship With Spray., in: 8th IAHR Symposium on Ice, Iowa City, 1986: pp. 179–194.

[27]W.P. Zakrzewski, Splashing a ship with collision-generated spray, Cold Reg Sci Technol. 14 (1987) 65–83. https://doi.org/10.1016/0165-232X(87)90045-0.

[28]R. Kato, Modelling of Ship Superstructure Icing - Application to Ice Bridge Simulators, Institutt for marin teknikk, 2012.

[29]A. Dehghani-Sanij, Y.S. Muzychka, G.F. Naterer, Predicted ice accretion on horizontal surfaces of marine vessels and offshore structures in Arctic regions, in: Proceedings of the International Conference on Offshore Mechanics and Arctic Engineering - OMAE, 2016: p. V007T06A056--V007T06A056. https://doi.org/10.1115/OMAE2016-54054.

[30]L.D. Minsk, Assessment of ice accretion on offshore structures., (1984). https://apps.dtic.mil/dtic/tr/fulltext/u2/a141996.pdf (accessed January 24, 2019).

[31]J. Shpund, J.A. Zhang, M. Pinsky, A. Khain, Microphysical structure of the marine boundary layer under strong wind and sea spray formation as seen from a 2D explicit microphysical model. Part III: Parameterization of height-dependent droplet size distribution, J Atmos Sci. 71 (2014) 1914–1934.

[32]S.R. Dehghani, G.F. Naterer, Y.S. Muzychka, Droplet size and velocity distributions of wave-impact sea spray over a marine vessel, Cold Reg Sci Technol. 132 (2016) 60–67.

[33]I. Horjen, S. Vefsnmo, A Kinematic and Thermodynamic Analysis of Sea Spray (in Norwegian), Offshore Icing—Phase II. STF60 F85014, Norwegian Hydrodynamic Laboratory (NHL), Norway. (1985).

[34]K.A. Emanuel, Sensitivity of tropical cyclones to surface exchange coefficients and revised steady-state model incorporating eye dynamics, J Atmos Sci. 52 (1995) 3969–3976. https://doi.org/10.1175/1520-0469(1995)052<3969:SOTCTS>2.0.CO;2.

[35]E.L. Andreas, A new sea spray generation function for wind speeds up to 32 m s-1, J Phys Oceanogr. 28 (1998) 2175–2184. https://doi.org/10.1175/1520-0485(1998)028<2175:ANSSGF>2.0.CO;2.

[36]M.A. Donelan, B.K. Haus, N. Reul, W.J. Plant, M. Stiassnie, H.C. Graber, O.B. Brown, E.S. Saltzman, On the limiting aerodynamic roughness of the ocean in very strong winds, Geophys Res Lett. 31 (2004). https://doi.org/10.1029/2004GL019460.

[37]F. Veron, C. Hopkins, E.L. Harrison, J.A. Mueller, Sea spray spume droplet production in high wind speeds, Geophys Res Lett. 39 (2012). https://doi.org/10.1029/2012GL052603.

[38]Lasse. Makkonen, M. Farzaneh, C. Volat, A. Leblond, J.-E. Lundqvist, I. Udin, G. Madras, B.J. McCoy, T.S. Jorgensen, P. v Hobbs, Ice accretion on ships with special emphasis on Baltic conditions, in: Ice Physics, Offshore Technology Testing and Research Group, Dordrecht, 1982: pp. 461–523. https://doi.org/10.1002/ejoc.201200111.

[39]G. Cammaert, Impact of marine icing on Arctic offshore operations, Arctic Marine Operations Challenges & Recommendations. Ville Miettinen. (2013).

[40]A. Kulyakhtin, O. Shipilova, M. Muskulus, Numerical simulation of droplet impingement and flow around a cylinder using RANS and LES models, J Fluids Struct. 48 (2014) 280–294. https://doi.org/10.1016/j.jfluidstructs.2014.03.007.

[41]T. Rashid, H.A. Khawaja, K. Edvardsen, Review of marine icing and anti-/de-icing systems, Journal of Marine Engineering & Technology. 15 (2016) 79–87. https://doi.org/10.1080/20464177.2016.1216734.

[42]R. Berr, U.S. Navy, Cold Weather Handbook for Surface Ships, Chief of Naval Operations, Surface Ship Survivability Office, 1988.

[43]A.N. Shekhtman, The Probability and Intensity of the Icing-Up of Ocean-Going Vessels, (1971).

[44]V. v. Panov, Icing of ships, Polar Geography. 2 (1978) 166–186. https://doi.org/10.1080/10889377809388652.

[45]R.D. Brown, P. Roebber, The ice accretion problem in Canadian waters related to offshore energy and transportation, Atmospheric Environment Service, Climatological Services Division, Ontario, Canada, 1985.

[46]L. Battisti, R. Fedrizzi, A. Brighenti, Sea Ice and Icing Risk for Offshore Wind Turbines, in: Owemes 2006, 20-22 April. Citavecchia, Italy, 2006: pp. 20–22.

[47]E. Madi, K. Pope, W. Huang, T. Iqbal, A review of integrating ice detection and mitigation for wind turbine blades, Renewable and Sustainable Energy Reviews. 103 (2019) 269–281. https://doi.org/10.1016/j.rser.2018.12.019.

[48]M. Nosonovsky, V. Hejazi, Why Superhydrophobic Surfaces Are Not Always Icephobic, ACS Nano. 6 (2012) 8488–8491. https://doi.org/10.1021/nn302138r.

[49]S.A. Kulinich, S. Farhadi, K. Nose, X.W. Du, Superhydrophobic Surfaces: Are They Really Ice-Repellent?, Langmuir. 27 (2011) 25–29. https://doi.org/10.1021/la104277q.

[50]S. Jung, M. Dorrestijn, D. Raps, A. Das, C.M. Megaridis, D. Poulikakos, Are superhydrophobic surfaces best for icephobicity?, Langmuir. 27 (2011) 3059–3066. https://doi.org/10.1021/la104762g.

[51]V. Hejazi, K. Sobolev, M. Nosonovsky, From superhydrophobicity to icephobicity: Forces and interaction analysis, Sci Rep. 3 (2013) 2194. https://doi.org/10.1038/srep02194.

[52]J.D. Crowley, Cold water effects upon marine operations, in: OCEANS'88. A Partnership of Marine Interests. Proceedings, 1988: pp. 543–548.

[53]Z. Wang, Recent progress on ultrasonic de-icing technique used for wind power generation, high-voltage transmission line and aircraft, Energy Build. 140 (2017) 42–49. https://doi.org/10.1016/j.enbuild.2017.01.072.

[54]S. Ramanathan, V. v Varadan, V.K. Varadan, Deicing of helicopter blades using piezoelectric actuators, in: Smart Structures and Materials 2000: Smart Electronics and MEMS, 2000: pp. 281–293.

[55]J.L. Palacios, E.C. Smith, H. Gao, J.L. Rose, Ultrasonic shear wave anti-icing system for helicopter rotor blades, in: Annual Forum Proceedings - AHS International, 2006: pp. 1483–1493.

[56]S. v. Venna, Y.J. Lin, G. Botura, Piezoelectric transducer actuated leading edge De-icing with simultaneous shear and impulse forces, J Aircr. 44 (2007) 509–515. https://doi.org/10.2514/1.23996.

[57]C. Yin, Z. Zhang, Z. Wang, H. Guo, Numerical simulation and experimental validation of ultrasonic de-icing system for wind turbine blade, Applied Acoustics. 114 (2016) 19–26. https://doi.org/10.1016/j.apacoust.2016.07.004.

[58]L. Makkonen, Ice Adhesion —Theory, Measurements and Countermeasures, J Adhes Sci Technol. 26 (2012) 413–445. https://doi.org/10.1163/016942411X574583.

[59]R. Lanoie, D. Bouchard, M. Lessard, Y. Turcotte, M. Roy, Using steam to de-ice energized substation disconnect switch, Montreal, 2005.

[60]H. Brazil, R. Conachey, G. Savage, P. Baen, Electrical Heat Tracing for Surface Heating on Arctic Vessels and Structures to Prevent Snow and Ice Accumulation, IEEE Trans Ind Appl. 49 (2013) 2466–2470. https://doi.org/10.1109/TIA.2013.2263372.

[61]Z. Zhao, H. Chen, X. Liu, H. Liu, D. Zhang, Development of high-efficient synthetic electric heating coating for anti-icing/de-icing, Surf Coat Technol. 349 (2018) 340–346. https://doi.org/10.1016/j.surfcoat.2018.06.011.

[62]M. Mohseni, A. Amirfazli, A novel electro-thermal anti-icing system for fiber-reinforced polymer composite airfoils, Cold Reg Sci Technol. 87 (2013) 47–58. https://doi.org/10.1016/j.coldregions.2012.12.003.

[63]X. Liu, H. Chen, Z. Zhao, Y. Yan, D. Zhang, Slippery liquid-infused porous electric heating coating for anti-icing and de-icing applications, Surf Coat Technol. 374 (2019) 889–896. https://doi.org/10.1016/j.surfcoat.2019.06.077.

[64]V.F. Petrenko, C.R. Sullivan, V. Kozlyuk, F. v. Petrenko, V. Veerasamy, Pulse electro-thermal de-icer (PETD), Cold Reg Sci Technol. 65 (2011) 70–78. https://doi.org/10.1016/j.coldregions.2010.06.002.

[65]S. Chavan, T. Foulkes, Y. Gurumukhi, K. Boyina, K.F. Rabbi, N. Miljkovic, Pulse interfacial defrosting, Appl Phys Lett. 115 (2019) 71601. https://doi.org/10.1063/1.5113845.

[66]E.A. Strouse, Development of Deicing Techniques for Dielectric Windows, 1975.

[67]J. Liu, J. Xu, S. Lu, H. Chen, Investigation on dielectric properties and microwave heating efficiencies of various concrete pavements during microwave deicing, Constr Build Mater. 225 (2019) 55–66. https://doi.org/10.1016/j.conbuildmat.2019.07.249.

[68]G.G. Koenig, C.C. Ryerson, An investigation of infrared deicing through experimentation, Cold Reg Sci Technol. 65 (2011) 79–87. https://doi.org/10.1016/j.coldregions.2010.03.009.

[69]L. Berntsson, S. Chandra, Damage of concrete sleepers by calcium chloride, Cem Concr Res. 12 (1982) 87–92. https://doi.org/10.1016/0008-8846(82)90102-8.

[70]N. Cui, L. Fay, X. Shi, Review on the Toxicological Effects of Chloride-Based Deicers: Impacted Environments and Assessment Methods, in: Environmental Sustainability in Transportation Infrastructure - Selected Papers from the International Symposium on Systematic Approaches to Environmental Sustainability in Transportation, 2015: pp. 256–271. https://doi.org/10.1061/9780784479285.021.

[71]D.M. Ramakrishna, T. Viraraghavan, Environmental impact of chemical deicers - A review, Water Air Soil Pollut. 166 (2005) 49–63. https://doi.org/10.1007/s11270-005-8265-9.

[72]Y. Farnam, S. Dick, A. Wiese, J. Davis, D. Bentz, J. Weiss, The influence of calcium chloride deicing salt on phase changes and damage development in cementitious

materials, Cem Concr Compos. 64 (2015) 1–15. https://doi.org/10.1016/j.cemconcomp.2015.09.006.

[73]M. V. Achkeeva, N. V. Romanyuk, E.A. Frolova, D.F. Kondakov, D.M. Khomyakov, V.P. Danilov, Deicing properties of sodium, potassium, magnesium, and calcium chlorides, sodium formate and salt compositions on their basis, Theoretical Foundations of Chemical Engineering. 49 (2015) 481–484. https://doi.org/10.1134/S0040579515040028.

[74]L. Greenawalt, Ice melt: a scientific primer on de-icers. sanitary maintenance, Cleanlink. (2006). https://www.cleanlink.com/sm/article/Ice-Melt-A-Scientific-Primer-On-Deicers--4896.

[75]N. Xie, X. Shi, Y. Zhang, Impacts of Potassium Acetate and Sodium-Chloride Deicers on Concrete, Journal of Materials in Civil Engineering. 29 (2017) 04016229. https://doi.org/10.1061/(asce)mt.1943-5533.0001754.

[76]N. Xie, A. Muthumani, Y. Dang, X. Shi, Deicer impacts on concrete bridge decks: A comparative study of field cores from potassium acetate and sodium chloride environments, in: Innovative Materials and Design for Sustainable Transportation Infrastructure - Selected Papers from the International Symposium on Systematic Approaches to Environmental Sustainability in Transportation, 2015: pp. 42–57. https://doi.org/10.1061/9780784479278.005.

[77]H. Alizadeh, K.A. Berglund, Comparison Of Corrosion Effects Of Potassium Succinate, Road Salt, And Calcium Magnesium Acetate On Aluminum And Steel, International Journal of Research in Engineering & Advanced Technology. 3 (2015) 129–138.

[78]M. Fischel, Evaluation of selected deicers based on a review of the literature, (2001) 1–273. q:%5Ceuras%5CLiterature%5CPdf (accessed June 20, 2018).

[79]M. Simonot, G. Mischka, N. Holland, J. Fieandt, J. Pontinen, A. Gerritsen, H. Krause, W. Bedrzycki, H.E. Bostrom, R. Buhler, Recommedations for De-icing/Anti-icing of aircraft on the ground, (2004).

[80]C. Murphy, S. Wallace, R. Knight, D. Cooper, T. Sellers, Treatment performance of an aerated constructed wetland treating glycol from de-icing operations at a UK airport, Ecol Eng. 80 (2015) 117–124. https://doi.org/10.1016/j.ecoleng.2014.05.032.

[81]X. Shi, M. Beutel, T. Long, A. Hellenthal, C. Bristoll-Groll, Green Stormwater Infrastructure Strategies for Airports: Challenges and Opportunities, in: Environmental Sustainability in Transportation Infrastructure - Selected Papers from the International Symposium on Systematic Approaches to Environmental Sustainability in Transportation, 2015: pp. 1–13. https://doi.org/10.1061/9780784479285.001.

[82]A. Mohiley, J. Franzaring, O.C. Calvo, A. Fangmeier, Potential toxic effects of aircraft de-icers and wastewater samples containing these compounds, Environmental Science and Pollution Research. 22 (2015) 13094–13101. https://doi.org/10.1007/s11356-015-4358-1.

[83]S.J. Reeves, M.G. Evans, M.H. Burtwell, Evaluation of frost, ice and snow precautions at stations, (2005).

[84]A. McConnell, De-icer and/or anti-icer compositions and methods, US9434868B2, 2016. https://patents.google.com/patent/US9434868B2/en (accessed May 13, 2021).

[85]R.A. Hartley, D.H. Wood, De-icing solution, US6582622B1, 2002. https://patents.google.com/patent/US6582622B1/en.

[86]A. Muthumani, X. Shi, Effectiveness of liquid agricultural by-products and solid complex chlorides for snow and ice control, Journal of Cold Regions Engineering. 31 (2016) 4016006.

[87]S. Bengaluru Subramanyam, V. Kondrashov, J. Rühe, K.K. Varanasi, Low Ice Adhesion on Nano-Textured Superhydrophobic Surfaces under Supersaturated Conditions, ACS Appl Mater Interfaces. 8 (2016) 12583–12587. https://doi.org/10.1021/acsami.6b01133.

[88]A.M. Coclite, R.M. Howden, D.C. Borrelli, C.D. Petruczok, R. Yang, J.L. Yagüe, A. Ugur, N. Chen, S. Lee, W.J. Jo, A. Liu, X. Wang, K.K. Gleason, 25th Anniversary Article: CVD polymers: A new paradigm for surface modification and device fabrication, Advanced Materials. 25 (2013) 5392–5423. https://doi.org/10.1002/adma.201301878.

[89]K. Golovin, S.P.R. Kobaku, D.H. Lee, E.T. DiLoreto, J.M. Mabry, A. Tuteja, Designing durable icephobic surfaces, Sci Adv. 2 (2016) e1501496. https://doi.org/10.1126/sciadv.1501496.

[90]Y. Pan, K. Shi, X. Duan, G.F. Naterer, Experimental investigation of water droplet impact and freezing on micropatterned stainless steel surfaces with varying wettabilities, Int J Heat Mass Transf. 129 (2019) 953–964. https://doi.org/10.1016/J.IJHEATMASSTRANSFER.2018.10.032.

[91]K. Shi, X. Duan, Heat Transfer Analysis of Icing Process on Metallic Surfaces of Different Wettabilities, in: H. Okada, S.N. Atluri (Eds.), Computational and

Experimental Simulations in Engineering, Springer, Cham, 2020: pp. 201–206. https://doi.org/10.1007/978-3-030-27053-7_19.

[92]J.D. Brassard, J.L. Laforte, C. Blackburn, J. Perron, D.K. Sarkar, Silicone based superhydrophobic coating efficient to reduce ice adhesion and accumulation on aluminum under offshore arctic conditions, Ocean Engineering. 144 (2017) 135–141. https://doi.org/10.1016/j.oceaneng.2017.08.022.

[93]M.J. Coady, M. Wood, G.Q. Wallace, K.E. Nielsen, A.-M. Kietzig, F. Lagugné-Labarthet, P.J. Ragogna, Icephobic Behavior of UV-Cured Polymer Networks Incorporated into Slippery Lubricant-Infused Porous Surfaces: Improving SLIPS Durability, ACS Appl Mater Interfaces. 10 (2018) 2890–2896. https://doi.org/10.1021/acsami.7b14433.

[94]W. Tong, D. Xiong, N. Wang, Z. Wu, H. Zhou, Mechanically robust superhydrophobic coating for aeronautical composite against ice accretion and ice adhesion, Compos B Eng. 176 (2019) 107267. https://doi.org/10.1016/j.compositesb.2019.107267.

[95]S. Zheng, D.A. Bellido-Aguilar, X. Wu, X. Zhan, Y. Huang, X. Zeng, Q. Zhang, Z. Chen, Durable Waterborne Hydrophobic Bio-Epoxy Coating with Improved Anti-Icing and Self-Cleaning Performance, ACS Sustain Chem Eng. 7 (2019) 641–649. https://doi.org/10.1021/acssuschemeng.8b04203.

[96]B. Liu, K. Zhang, C. Tao, Y. Zhao, X. Li, K. Zhu, X. Yuan, Strategies for anti-icing: Low surface energy or liquid-infused?, RSC Adv. 6 (2016) 70251–70260. https://doi.org/10.1039/c6ra11383d.

[97]M.J. Kreder, J. Alvarenga, P. Kim, J. Aizenberg, Design of anti-icing surfaces: Smooth, textured or slippery?, Nat Rev Mater. 1 (2016) 1–15. https://doi.org/10.1038/natrevmats.2015.3.

[98]S. Farhadi, M. Farzaneh, S.A. Kulinich, Anti-icing performance of superhydrophobic surfaces, Appl Surf Sci. 257 (2011) 6264–6269. https://doi.org/10.1016/j.apsusc.2011.02.057.

[99]P. Kim, T.S. Wong, J. Alvarenga, M.J. Kreder, W.E. Adorno-Martinez, J. Aizenberg, Liquid-infused nanostructured surfaces with extreme anti-ice and anti-frost performance, ACS Nano. 6 (2012) 6569–6577. https://doi.org/10.1021/nn302310q.

[100]T.S. Wong, S.H. Kang, S.K.Y. Tang, E.J. Smythe, B.D. Hatton, A. Grinthal, J. Aizenberg, Bioinspired self-repairing slippery surfaces with pressure-stable omniphobicity, Nature. 477 (2011) 443–447. https://doi.org/10.1038/nature10447.

[101]J.D. Smith, R. Dhiman, S. Anand, E. Reza-Garduno, R.E. Cohen, G.H. Mckinley, K.K. Varanasi, S.L. Zhang, J.D. Smith, R. Dhiman, S. Anand, E. Reza-Garduno, R.E. Cohen, G.H. Mckinley, K.K. Varanasi, Droplet mobility on lubricant-impregnated surfaces, Soft Matter. 9 (2013) 1772–1780. https://doi.org/10.1039/C2SM27032C.

[102]K. Rykaczewski, S. Anand, S.B. Subramanyam, K.K. Varanasi, Mechanism of frost formation on lubricant-impregnated surfaces, Langmuir. 29 (2013) 5230–5238. https://doi.org/10.1021/la400801s.

[103]J. Lv, Y. Song, L. Jiang, J. Wang, Bio-inspired strategies for anti-icing, ACS Nano. 8 (2014) 3152–3169. https://doi.org/10.1021/nn406522n.

[104]Q. Liu, Y. Yang, M. Huang, Y. Zhou, Y. Liu, X. Liang, Durability of a lubricant-infused Electrospray Silicon Rubber surface as an anti-icing coating, Appl Surf Sci. 346 (2015) 68–76. https://doi.org/10.1016/j.apsusc.2015.02.051.

[105]J. Chen, Z. Luo, Q. Fan, J. Lv, J. Wang, Anti-Ice Coating Inspired by Ice Skating, Small. 10 (2014) 4693–4699. https://doi.org/10.1002/smll.201401557.

[106]J. Chen, R. Dou, D. Cui, Q. Zhang, Y. Zhang, F. Xu, X. Zhou, J. Wang, Y. Song, L. Jiang, Robust prototypical anti-icing coatings with a self-lubricating liquid water layer between ice and substrate, ACS Appl Mater Interfaces. 5 (2013) 4026–4030. https://doi.org/10.1021/am401004t.

[107]D. Chen, M.D. Gelenter, M. Hong, R.E. Cohen, G.H. McKinley, Icephobic surfaces induced by interfacial nonfrozen water, ACS Appl Mater Interfaces. 9 (2017) 4202–4214. https://doi.org/10.1021/acsami.6b13773.

[108]R. Dou, J. Chen, Y. Zhang, X. Wang, D. Cui, Y. Song, L. Jiang, J. Wang, Anti-icing coating with an aqueous lubricating layer, ACS Appl Mater Interfaces. 6 (2014) 6998–7003. https://doi.org/10.1021/am501252u.

[109]R. Li, Y. Zhou, X. Duan, A novel composite phase change material with paraffin wax in tailings porous ceramics, Appl Therm Eng. 151 (2019) 115–123. https://doi.org/10.1016/j.applthermaleng.2019.01.104.

[110]M. Parsazadeh, X. Duan, Numerical study on the effects of fins and nanoparticles in a shell and tube phase change thermal energy storage unit, Appl Energy. 216 (2018) 142–156. https://doi.org/10.1016/j.apenergy.2018.02.052.

[111]V. Saydam, M. Parsazadeh, M. Radeef, X. Duan, Design and experimental analysis of a helical coil phase change heat exchanger for thermal energy storage, J Energy Storage. 21 (2019) 9–17. https://doi.org/10.1016/j.est.2018.11.006.

[112]M. Parsazadeh, X. Duan, Numerical and statistical study on melting of nanoparticle enhanced phase change material in a shell-and-tube thermal energy storage system, Appl Therm Eng. 111 (2017) 950–960. https://doi.org/10.1016/j.applthermaleng.2016.09.133.

[113]X. Duan, Subsea Pipeline Hybrid Thermal Insulation with Phase Change Material and Aerogel – Analysis and Experiments, in: A. Vasel-Be-Hagh, DK. Ting (Eds.), Springer Proceedings in Energy, Springer International Publishing, Cham, 2020: pp. 36–48. https://doi.org/10.1007/978-3-030-38804-1_2.

[114]X. Cocu, D. Nicaise, S. Rachidi, The use of phase change materials to delay pavement freezing, in: Transport Research Arena (TRA), Québec (Canada), 2010: pp. 1–25. http://www.brrc.be/pdf/15/IP4_Cocu_EF.pdf (accessed May 10, 2020).

[115]F. Wang, W. Ding, J. He, Z. Zhang, Phase transition enabled durable anti-icing surfaces and its DIY design, Chemical Engineering Journal. 360 (2019) 243–249. https://doi.org/10.1016/j.cej.2018.11.224.

[116]K. Zhu, X. Li, J. Su, H. Li, Y. Zhao, X. Yuan, Improvement of anti-icing properties of low surface energy coatings by introducing phase-change microcapsules, Polym Eng Sci. 58 (2018) 973–979. https://doi.org/10.1002/pen.24654.

[117]R. Chatterjee, D. Beysens, S. Anand, Delaying Ice and Frost Formation Using Phase-Switching Liquids, Advanced Materials. 31 (2019) 1807812. https://doi.org/10.1002/adma.201807812.

[118]X. Duan, G.F. Naterer, Thermal protection of a ground layer with phase change materials, J Heat Transfer. 132 (2010) 1–9. https://doi.org/10.1115/1.3194764.

[119]T. Cheng, R. He, Q. Zhang, X. Zhan, F. Chen, Magnetic particle-based super-hydrophobic coatings with excellent anti-icing and thermoresponsive deicing performance, J Mater Chem A Mater. 3 (2015) 21637–21646. https://doi.org/10.1039/c5ta05277g.

[120]X. Yin, Y. Zhang, D. Wang, Z. Liu, Y. Liu, X. Pei, B. Yu, F. Zhou, Integration of Self-Lubrication and Near-Infrared Photothermogenesis for Excellent Anti-Icing/Deicing Performance, Adv Funct Mater. 25 (2015) 4237–4245. https://doi.org/10.1002/adfm.201501101.

[121]S. Dash, J. de Ruiter, K.K. Varanasi, Photothermal trap utilizing solar illumination for ice mitigation, Sci Adv. 4 (2018) eaat0127. https://doi.org/10.1126/sciadv.aat0127.

[122]E. Mitridis, T.M. Schutzius, A. Sicher, C.U. Hail, H. Eghlidi, D. Poulikakos, Metasurfaces Leveraging Solar Energy for Icephobicity, ACS Nano. 12 (2018) 7009–7013. https://doi.org/10.1021/acsnano.8b02719.

[123]K. Golovin, A. Dhyani, M.D. Thouless, A. Tuteja, Low–interfacial toughness materials for effective large-scale deicing, Science (1979). 364 (2019) 371–375. https://doi.org/10.1126/science.aav1266.

[124]N. Wang, D. Xiong, Y. Deng, Y. Shi, K. Wang, Mechanically robust superhydrophobic steel surface with anti-icing, UV-durability, and corrosion resistance properties, ACS Appl Mater Interfaces. 7 (2015) 6260–6272. https://doi.org/10.1021/acsami.5b00558.

[125]L. Li, V. Breedveld, D.W. Hess, Creation of superhydrophobic stainless steel surfaces by acid treatments and hydrophobic film deposition, ACS Appl Mater Interfaces. 4 (2012) 4549–4556. https://doi.org/10.1021/am301666c.

[126]S. Barthwal, Y.S. Kim, S.-H. Lim, Mechanically Robust Superamphiphobic Aluminum Surface with Nanopore-Embedded Microtexture, Langmuir. 29 (2013) 11966–11974. https://doi.org/10.1021/la402600h.

[127]R. Liao, Z. Zuo, C. Guo, Y. Yuan, A. Zhuang, Fabrication of superhydrophobic surface on aluminum by continuous chemical etching and its anti-icing property, Appl Surf Sci. 317 (2014) 701–709. https://doi.org/10.1016/j.apsusc.2014.08.187.

[128]J.H. Kim, A. Mirzaei, H.W. Kim, S.S. Kim, Facile fabrication of superhydrophobic surfaces from austenitic stainless steel (AISI 304) by chemical etching, Appl Surf Sci. 439 (2018) 598–604. https://doi.org/10.1016/j.apsusc.2017.12.211.

[129]M.R. Attar, E. Khajavian, S. Hosseinpour, A. Davoodi, Fabrication of micro–nano-roughened surface with superhydrophobic character on an aluminium alloy surface by a facile chemical etching process, Bulletin of Materials Science. 43 (2020) 31. https://doi.org/10.1007/s12034-019-1998-7.

[130]G. Liu, M. Xing, T. Yu, X. Lei, Fabrication of Low Adhesion Superhydrophobic Surface on Aluminum by TSA Cooperates with HCl Chemical Etching Method and Its Stability, Surface Technology. 48 (2019) 140-149+159. https://doi.org/10.16490/j.cnki.issn.1001-3660.2019.12.016.

[131]J. Lomga, P. Varshney, D. Nanda, M. Satapathy, S.S. Mohapatra, A. Kumar, Fabrication of durable and regenerable superhydrophobic coatings with excellent self-

cleaning and anti-fogging properties for aluminium surfaces, J Alloys Compd. 702 (2017) 161–170. https://doi.org/10.1016/j.jallcom.2017.01.243.

[132]D. Infante, K.W. Koch, P. Mazumder, L. Tian, A. Carrilero, D. Tulli, D. Baker, V. Pruneri, Durable, superhydrophobic, antireflection, and low haze glass surfaces using scalable metal dewetting nanostructuring, Nano Res. 6 (2013) 429–440. https://doi.org/10.1007/s12274-013-0320-z.

[133]T.B. Nguyen, S. Park, H. Lim, Effects of morphology parameters on anti-icing performance in superhydrophobic surfaces, Appl Surf Sci. 435 (2018) 585–591. https://doi.org/10.1016/j.apsusc.2017.11.137.

[134]C. Con, B. Cui, Surface Nanostructures Formed by Phase Separation of Metal Salt–Polymer Nanocomposite Film for Anti-reflection and Super-hydrophobic Applications, Nanoscale Res Lett. 12 (2017). https://doi.org/10.1186/s11671-017-2402-4.

[135]A. Steele, B.K. Nayak, A. Davis, M.C. Gupta, E. Loth, Linear abrasion of a titanium superhydrophobic surface prepared by ultrafast laser microtexturing, Journal of Micromechanics and Microengineering. 23 (2013) 115012. https://doi.org/10.1088/0960-1317/23/11/115012.

[136]A.Y. Vorobyev, C. Guo, Multifunctional surfaces produced by femtosecond laser pulses, J Appl Phys. 117 (2015) 33103. https://doi.org/10.1063/1.4905616.

[137]P. Li, Y. Zeng, H. Yan, J. Chen, Investigation on stable superhydrophobic polycarbonate based compound induced by KrF excimer laser irradiation, Appl Surf Sci. 457 (2018) 1110–1115. https://doi.org/10.1016/j.apsusc.2018.07.016.

[138]Z. Yang, X. Liu, Y. Tian, Novel metal-organic super-hydrophobic surface fabricated by nanosecond laser irradiation in solution, Colloids Surf A Physicochem Eng Asp. 587 (2020). https://doi.org/10.1016/j.colsurfa.2019.124343.

[139]X. Li, G. Wang, A.S. Moita, C. Zhang, S. Wang, Y. Liu, Fabrication of bio-inspired non-fluorinated superhydrophobic surfaces with anti-icing property and its wettability transformation analysis, Appl Surf Sci. 505 (2020). https://doi.org/10.1016/j.apsusc.2019.144386.

[140]C. Cui, X. Duan, B. Collier, K.M. Poduska, Fabrication and wettability analysis of hydrophobic stainless steel surfaces with microscale structures from nanosecond laser machining, J Micro Nanomanuf. 6 (2018) 031006. https://doi.org/10.1115/1.4040469.

[141]D. Ge, L. Yang, G. Wu, S. Yang, Spray coating of superhydrophobic and angle-independent coloured films, Chemical Communications. 50 (2014) 2469–2472. https://doi.org/10.1039/c3cc48962k.

[142]K. Feng, G.Y. Hung, J. Liu, M. Li, C. Zhou, M. Liu, Fabrication of high performance superhydrophobic coatings by spray-coating of polysiloxane modified halloysite nanotubes, Chemical Engineering Journal. 331 (2018) 744–754. https://doi.org/10.1016/j.cej.2017.09.023.

[143]Q.Y. Cheng, M.C. Liu, Y.D. Li, J. Zhu, A.K. Du, J.B. Zeng, Biobased super-hydrophobic coating on cotton fabric fabricated by spray-coating for efficient oil/water separation, Polym Test. 66 (2018) 41–47. https://doi.org/10.1016/j.polymertesting.2018.01.005.

[144]S. Pan, N. Wang, D. Xiong, Y. Deng, Y. Shi, Fabrication of superhydrophobic coating via spraying method and its applications in anti-icing and anti-corrosion, Appl Surf Sci. 389 (2016) 547–553. https://doi.org/10.1016/j.apsusc.2016.07.138.

[145]Y. Shen, Y. Wu, J. Tao, C. Zhu, H. Chen, Z. Wu, Y. Xie, Spraying Fabrication of Durable and Transparent Coatings for Anti-Icing Application: Dynamic Water Repellency, Icing Delay, and Ice Adhesion, ACS Appl Mater Interfaces. 11 (2019) 3590–3598. https://doi.org/10.1021/acsami.8b19225.

[146]D. Zhang, X.Z. Jin, T. Huang, N. Zhang, X.D. Qi, J.H. Yang, Z.W. Zhou, Y. Wang, Electrospun Fibrous Membranes with Dual-Scaled Porous Structure: Super Hydrophobicity, Super Lipophilicity, Excellent Water Adhesion, and Anti-Icing for Highly Efficient Oil Adsorption/Separation, ACS Appl Mater Interfaces. 11 (2019) 5073–5083. https://doi.org/10.1021/acsami.8b19523.

[147]C. Su, Y. Li, Y. Dai, F. Gao, K. Tang, H. Cao, Fabrication of three-dimensional superhydrophobic membranes with high porosity via simultaneous electrospraying and electrospinning, Mater Lett. 170 (2016) 67–71. https://doi.org/10.1016/j.matlet.2016.01.133.

[148]M. Long, S. Peng, W. Deng, X. Yang, K. Miao, N. Wen, X. Miao, W. Deng, Robust and thermal-healing superhydrophobic surfaces by spin-coating of polydimethylsiloxane, J Colloid Interface Sci. 508 (2017) 18–27. https://doi.org/10.1016/j.jcis.2017.08.027.

[149]H. Zhang, X. Lu, Z. Xin, W. Zhang, C. Zhou, Preparation of superhydrophobic polybenzoxazine/SiO2 films with self-cleaning and ice delay properties, Prog Org Coat. 123 (2018) 254–260. https://doi.org/10.1016/j.porgcoat.2018.03.026.

[150]I. Yilgor, S. Bilgin, M. Isik, E. Yilgor, Facile preparation of superhydrophobic polymer surfaces, Polymer (Guildf). 53 (2012) 1180–1188. https://doi.org/10.1016/j.polymer.2012.01.053.

[151]S. Amigoni, E.T. Givenchy De, M. Dufay, F. Guittard, Covalent layer-by-layer assembled superhydrophobic organic-inorganic hybrid films, Langmuir. 25 (2009) 11073–11077. https://doi.org/10.1021/la901369f.

[152]M.M. Ahmad, A. Eshaghi, Fabrication of antireflective superhydrophobic thin film based on the TMMS with self-cleaning and anti-icing properties, Prog Org Coat. 122 (2018) 199–206. https://doi.org/10.1016/j.porgcoat.2018.06.001.

[153]S. Sriram, R.K. Singh, A. Kumar, Silica and Silane based polymer composite coating on glass slide by dip-Coating Method, Surfaces and Interfaces. 19 (2020). https://doi.org/10.1016/j.surfin.2020.100472.

[154]B. Gao, K.M. Poduska, Electrodeposited Zn for Water-Repellent Coatings, J Electrochem Soc. 165 (2018) D472–D476. https://doi.org/10.1149/2.1141810jes.

[155]B. Zhang, S. Lu, W. Xu, Y. Cheng, Controllable wettability and morphology of electrodeposited surfaces on zinc substrates, Appl Surf Sci. 360 (2016) 904–914. https://doi.org/10.1016/j.apsusc.2015.11.083.

[156]L. Shen, M. Fan, M. Qiu, W. Jiang, Z. Wang, Superhydrophobic nickel coating fabricated by scanning electrodeposition, Appl Surf Sci. 483 (2019) 706–712. https://doi.org/10.1016/j.apsusc.2019.04.019.

[157]Z. Kang, W. Li, Facile and fast fabrication of superhydrophobic surface on magnesium alloy by one-step electrodeposition method, Journal of Industrial and Engineering Chemistry. 50 (2017) 50–56. https://doi.org/10.1016/j.jiec.2017.01.016.

[158]J. Li, J. Xu, Z. Lian, Z. Yu, H. Yu, Fabrication of antireflection surfaces with superhydrophobic property for titanium alloy by nanosecond laser irradiation, Opt Laser Technol. 126 (2020). https://doi.org/10.1016/j.optlastec.2020.106129.

[159]A. Alizadeh, V. Bahadur, S. Zhong, W. Shang, R. Li, J. Ruud, M. Yamada, L. Ge, A. Dhinojwala, M. Sohal, Temperature dependent droplet impact dynamics on flat and textured surfaces, Appl Phys Lett. 100 (2012) 111601. https://doi.org/10.1063/1.3692598.

[160]T. Xiang, M. Zhang, C. Li, S. Zheng, S. Ding, J. Wang, C. Dong, L. Yang, A facile method for fabrication of superhydrophobic surface with controllable water adhesion and its applications, J Alloys Compd. 704 (2017) 170–179. https://doi.org/10.1016/j.jallcom.2017.01.277.

[161]Z. Shi, X. Zhang, Contact angle hysteresis analysis on superhydrophobic surface based on the design of channel and pillar models, Mater Des. 131 (2017) 323–333. https://doi.org/10.1016/J.MATDES.2017.06.008.

[162]S. Barthwal, S.-H. Lim, Fabrication of long-term stable superoleophobic surface based on copper oxide/cobalt oxide with micro-nanoscale hierarchical roughness, Appl Surf Sci. 328 (2015) 296–305. https://doi.org/10.1016/j.apsusc.2014.11.182.

[163]N.J. Shirtcliffe, G. McHale, M.I. Newton, G. Chabrol, C.C. Perry, Dual-Scale Roughness Produces Unusually Water-Repellent Surfaces, Advanced Materials. 16 (2004) 1929–1932. https://doi.org/10.1002/adma.200400315.

[164]K.J. Kubiak, M.C.T. Wilson, T.G. Mathia, P. Carval, Wettability versus roughness of engineering surfaces, Wear. 271 (2011) 523–528. https://doi.org/10.1016/j.wear.2010.03.029.

[165]P. Li, J. Xie, Z. Deng, Characterization of irregularly micro-structured surfaces related to their wetting properties, Appl Surf Sci. 335 (2015) 29–38. https://doi.org/10.1016/j.apsusc.2015.01.220.

[166]P.-G. de Gennes, F. Brochard-Wyart, D. Quéré, Capillarity and Wetting Phenomena, 1st ed., Springer New York, New York, 2004. https://doi.org/10.1007/978-0-387-21656-0.

[167]J. Elms, Characterizing dynamic wetting behaviour on irregularly roughened surfaces, Thesis (Masters), Memorial University of Newfoundland, 2018. https://research.library.mun.ca/13594/1/thesis.pdf (accessed April 14, 2019).

[168]C.G.L. Furmidge, Studies at phase interfaces. I. The sliding of liquid drops on solid surfaces and a theory for spray retention, J Colloid Sci. 17 (1962) 309–324. https://doi.org/10.1016/0095-8522(62)90011-9.

[169]S. Gulec, S. Yadav, R. Das, V. Bhave, R. Tadmor, The Influence of Gravity on Contact Angle and Circumference of Sessile and Pendant Drops has a Crucial Historic Aspect, Langmuir. 35 (2019) 5435–5441. https://doi.org/10.1021/acs.langmuir.8b03861.

[170]M. Sakai, J.H. Song, N. Yoshida, S. Suzuki, Y. Kameshima, A. Nakajima, Relationship between sliding acceleration of water droplets and dynamic contact angles on hydrophobic surfaces, Surf Sci. 600 (2006). https://doi.org/10.1016/j.susc.2006.06.039.

[171]M. Sakai, A. Hashimoto, N. Yoshida, S. Suzuki, Y. Kameshima, A. Nakajima, Image analysis system for evaluating sliding behavior of a liquid droplet on a hydrophobic surface, Review of Scientific Instruments. 78 (2007) 45103. https://doi.org/10.1063/1.2716005.

[172]E. Pierce, F.J. Carmona, A. Amirfazli, Understanding of sliding and contact angle results in tilted plate experiments, Colloids Surf A Physicochem Eng Asp. 323 (2008) 73–82. https://doi.org/10.1016/j.colsurfa.2007.09.032.

[173]S. Ravi Annapragada, J.Y. Murthy, S. v. Garimella, Prediction of droplet dynamics on an incline, Int J Heat Mass Transf. 55 (2012) 1466–1474. https://doi.org/10.1016/J.IJHEATMASSTRANSFER.2011.10.028.

[174]N. Gao, F. Geyer, D.W. Pilat, S. Wooh, D. Vollmer, H.J. Butt, R. Berger, How drops start sliding over solid surfaces, Nat Phys. 14 (2018) 191–196. https://doi.org/10.1038/nphys4305.

[175]L. Makkonen, A thermodynamic model of contact angle hysteresis, Journal of Chemical Physics. 147 (2017) 64703. https://doi.org/10.1063/1.4996912.

[176]J. Xie, J. Xu, W. Shang, K. Zhang, Mode selection between sliding and rolling for droplet on inclined surface: Effect of surface wettability, Int J Heat Mass Transf. 122 (2018) 45–58. https://doi.org/10.1016/j.ijheatmasstransfer.2018.01.098.

[177]F. Tancini, Y.-L. Wu, W.B. Schweizer, J.-P. Gisselbrecht, C. Boudon, P.D. Jarowski, M.T. Beels, I. Biaggio, F. Diederich, 1,1-Dicyano-4-[4-(diethylamino)phenyl]buta-1,3-dienes: Structure-Property Relationships, European J Org Chem. 2012 (2012) 2756–2765. https://doi.org/10.1002/ejoc.201200111.

[178]N.H. Fletcher, Size effect in heterogeneous nucleation, J Chem Phys. 29 (1958) 572–576. https://doi.org/10.1063/1.1744540.

[179]L. Mishchenko, B. Hatton, V. Bahadur, J.A. Taylor, T. Krupenkin, J. Aizenberg, Design of Ice-free Nanostructured Surfaces Based on Repulsion of Impacting Water Droplets, ACS Nano. 4 (2010) 7699–7707. https://doi.org/10.1021/nn102557p.

[180]Z. Yoshimitsu, A. Nakajima, T. Watanabe, K. Hashimoto, Effects of Surface Structure on the Hydrophobicity and Sliding Behavior of Water Droplets, Langmuir. 18 (2002) 5818–5822. https://doi.org/10.1021/la020088p.

[181]S. Wang, K. Liu, X. Yao, L. Jiang, Bioinspired Surfaces with Superwettability: New Insight on Theory, Design, and Applications, Chem Rev. 115 (2015) 8230–8293. https://doi.org/10.1021/cr400083y.

[182]I. Malavasi, F. Veronesi, A. Caldarelli, M. Zani, M. Raimondo, M. Marengo, Is a Knowledge of Surface Topology and Contact Angles Enough to Define the Drop Impact Outcome?, Langmuir. 32 (2016). https://doi.org/10.1021/acs.langmuir.6b01117.

[183]S. Zhenyu, L. Zhanqiang, S. Hao, Z. Xianzhi, Prediction of contact angle for hydrophobic surface fabricated with micro-machining based on minimum Gibbs free energy, Appl Surf Sci. 364 (2016) 597–603. https://doi.org/10.1016/j.apsusc.2015.12.199.

[184]A.L. Yarin, DROP IMPACT DYNAMICS: Splashing, Spreading, Receding, Bouncing…, Annu Rev Fluid Mech. 38 (2006) 159–192. https://doi.org/10.1146/annurev.fluid.38.050304.092144.

[185]T. Mao, D.C.S.S. Kuhn, H. Tran, Spread and rebound of liquid droplets upon impact on flat surfaces, AIChE Journal. 43 (1997) 2169–2179. https://doi.org/10.1002/aic.690430903.

[186]L.S. Lam, K.R. Sultana, K. Pope, Y.S. Muzychka, Effect of thermal transport on solidification of salt and freshwater water droplets on marine surfaces, Int J Heat Mass Transf. 153 (2020) 119452. https://doi.org/10.1016/j.ijheatmasstransfer.2020.119452.

[187]E. Teodori, A.S. Moita, M. Moura, P. Pontes, A. Moreira, Y. Bai, X. Li, Y. Liu, Application of Bioinspired Superhydrophobic Surfaces in Two-phase Heat Transfer

Experiments, J Bionic Eng. 14 (2017) 506–519. https://doi.org/10.1016/S1672-6529(16)60417-1.

[188]S. Ding, Z. Hu, L. Dai, X. Zhang, X. Wu, Droplet impact dynamics on single-pillar superhydrophobic surfaces, Physics of Fluids. 33 (2021). https://doi.org/10.1063/5.0066366.

[189]X. Yao, J. Ju, Z. Yang, X. Yi, Z. Jin, Impingement and freezing of a supercooled large droplet on an ice surface, Physics of Fluids. 33 (2021). https://doi.org/10.1063/5.0069596.

[190]S.L.T.T. de Souza, I.L. Caldas, R.L. Viana, Damping control law for a chaotic impact oscillator, Chaos Solitons Fractals. 32 (2007) 745–750. https://doi.org/10.1016/j.chaos.2005.11.046.

[191]X. Zhang, X. Wu, J. Min, X. Liu, Modelling of sessile water droplet shape evolution during freezing with consideration of supercooling effect, Appl Therm Eng. 125 (2017) 644–651. https://doi.org/10.1016/j.applthermaleng.2017.07.017.

[192]X. Zhang, X. Liu, J. Min, X. Wu, Shape variation and unique tip formation of a sessile water droplet during freezing, Appl Therm Eng. 147 (2018) 927–934. https://doi.org/10.1016/j.applthermaleng.2018.09.040.

[193]X. Zhang, X. Liu, X. Wu, J. Min, Impacting-freezing dynamics of a supercooled water droplet on a cold surface: Rebound and adhesion, Int J Heat Mass Transf. 158 (2020) 119997. https://doi.org/10.1016/j.ijheatmasstransfer.2020.119997.

[194]B. Ding, H. Wang, X. Zhu, R. Chen, Q. Liao, Water droplet impact on superhydrophobic surfaces with various inclinations and supercooling degrees, Int J Heat

Mass Transf. 138 (2019) 844–851. https://doi.org/10.1016/j.ijheatmasstransfer.2019.04.106.

[195]W. Ranz, W. Marshall, Analysis evaporation from drops, Chem Eng Prog. 48 (1952) 141–146.

[196]W. Cui, Y. Jiang, K. Mielonen, T.A. Pakkanen, The verification of icephobic performance on biomimetic superhydrophobic surfaces and the effect of wettability and surface energy, Appl Surf Sci. 466 (2019) 503–514. https://doi.org/10.1016/j.apsusc.2018.10.042.

[197]P. Zhang, F.Y. Lv, A review of the recent advances in superhydrophobic surfaces and the emerging energy-related applications, Energy. 82 (2015) 1068–1087. https://doi.org/10.1016/j.energy.2015.01.061.

[198]S. Chang, H. Song, K. Wu, Experimental investigation on impact dynamics and freezing performance of water droplet on horizontal cold surface, Sustainable Energy Technologies and Assessments. 45 (2021) 101128. https://doi.org/10.1016/j.seta.2021.101128.

[199]Y. Pan, K. Shi, X. Duan, G. Naterer, Droplet Impact, Spreading and Freezing on Metallic Surfaces of varying Wettability, in: Progress in Canadian Mechanical Engineering, York University Libraries, 2018: pp. 1–5. https://doi.org/10.25071/10315/35339.

[200]F.J. Montes Ruiz-Cabello, S. Bermúdez-Romero, P.F. Ibáñez-Ibáñez, M.A. Cabrerizo-Vílchez, M.A. Rodríguez-Valverde, Freezing delay of sessile drops: Probing the impact of contact angle, surface roughness and thermal conductivity, Appl Surf Sci. 537 (2021) 147964. https://doi.org/10.1016/j.apsusc.2020.147964.

[201]R. Attarzadeh, A. Dolatabadi, Icephobic performance of superhydrophobic coatings: A numerical analysis, Int J Heat Mass Transf. 136 (2019) 1327–1337. https://doi.org/10.1016/j.ijheatmasstransfer.2019.03.079.

[202] and E.C.M. M.G. Ferrick, N.D. Mulherin, R.B. Haehnel, B.A. Coutermarsh, G.D. Durell, T.J. Tantillo, T.L. St. Clair, E.S. Weiser, R.J. Cano, T.M. Smith, Double Lap Shear Testing of Coating Modified Ice Adhesion to Liquid Oxygen Feed Line Bracket, Space Shuttle External Tank, 2006. https://doi.org/http://www.dtic.mil/dtic/tr/fulltext/u2/a448580.pdf.

[203]S. Akhtar, M. Xu, A.P. Sasmito, Development and validation of a semi-analytical framework for droplet freezing with heterogeneous nucleation and non-linear interface kinetics, Int J Heat Mass Transf. 166 (2021) 120734. https://doi.org/10.1016/j.ijheatmasstransfer.2020.120734.

[204]T. Jonsson, On the one dimensional Stefan problem with some numerical analysis, Degree of Bachelor, Umeå University, 2013. http://umu.diva-portal.org/smash/record.jsf?pid=diva2%3A647481&dswid=5957 (accessed July 1, 2022).

[205]M. Xu, S. Akhtar, A.F. Zueter, V. Auger, M.A. Alzoubi, A.P. Sasmito, Development of Analytical Solution for a Two-Phase Stefan Problem in Artificial Ground Freezing Using Singular Perturbation Theory, J Heat Transfer. 142 (2020). https://doi.org/10.1115/1.4048137.

[206]Q. Zeng, S. Xu, Thermodynamics and Characteristics of Heterogeneous Nucleation on Fractal Surfaces, J. Phys. Chem. C. 119 (2015) 45. https://doi.org/10.1021/acs.jpcc.5b07709.

[207]Q. Zeng, S. Xu, Thermodynamics and Characteristics of Heterogeneous Nucleation on Fractal Surfaces, J. Phys. Chem. C. 119 (2015) 30. https://doi.org/10.1021/acs.jpcc.5b07709.

[208]Z. Meng, P. Zhang, Dynamic propagation of ice-water phase front in a supercooled water droplet, Int J Heat Mass Transf. 152 (2020) 119468. https://doi.org/10.1016/j.ijheatmasstransfer.2020.119468.

[209]Y. Yamada, G. Onishi, A. Horibe, Sessile Droplet Freezing on Hydrophobic Structured Surfaces under Cold Ambient Conditions, Langmuir. 35 (2019) 16401–16406. https://doi.org/10.1021/acs.langmuir.9b01173.

[210]J.P. Hindmarsh, A.B. Russell, X.D. Chen, Experimental and numerical analysis of the temperature transition of a suspended freezing water droplet, Int J Heat Mass Transf. 46 (2003) 1199–1213. https://doi.org/10.1016/S0017-9310(02)00399-X.

[211]J. Madejski, Solidification of droplets on a cold surface, Int J Heat Mass Transf. 19 (1976) 1009–1013. https://doi.org/10.1016/0017-9310(76)90183-6.

[212]Y. Yonemoto, T. Kunugi, Analytical consideration of liquid droplet impingement on solid surfaces, Sci Rep. 7 (2017). https://doi.org/10.1038/s41598-017-02450-4.

[213]S. Akhtar, M. Xu, A.P. Sasmito, Development and validation of a semi-analytical framework for droplet freezing with heterogeneous nucleation and non-linear interface kinetics, Int J Heat Mass Transf. 166 (2021) 120734. https://doi.org/10.1016/j.ijheatmasstransfer.2020.120734.

[214]Y. Yao, C. Li, Z. Tao, R. Yang, H. Zhang, Experimental and numerical study on the impact and freezing process of a water droplet on a cold surface, Appl Therm Eng. 137 (2018) 83–92. https://doi.org/10.1016/j.applthermaleng.2018.03.057.

[215]J. Du, X. Wang, Y. Li, Q. Min, X. Wu, Analytical Consideration for the Maximum Spreading Factor of Liquid Droplet Impact on a Smooth Solid Surface, Langmuir. 37 (2021). https://doi.org/10.1021/acs.langmuir.1c01076.

[216]H. Zhang, Y. Zhao, R. Lv, C. Yang, Freezing of sessile water droplet for various contact angles, International Journal of Thermal Sciences. 101 (2016) 59–67. https://doi.org/10.1016/j.ijthermalsci.2015.10.027.

[217]M. Stiti, G. Castanet, A. Labergue, F. Lemoine, Icing of a droplet deposited onto a subcooled surface, Int J Heat Mass Transf. 159 (2020) 120116. https://doi.org/10.1016/j.ijheatmasstransfer.2020.120116.

[218]A. Alizadeh, M. Yamada, R. Li, W. Shang, S. Otta, S. Zhong, L. Ge, A. Dhinojwala, K.R. Conway, V. Bahadur, A.J. Vinciquerra, B. Stephens, M.L. Blohm, Dynamics of Ice Nucleation on Water Repellent Surfaces, Langmuir. 28 (2012) 3180–3186. https://doi.org/10.1021/la2045256.

[219]M. Pasandideh-Fard, S. Chandra, J. Mostaghimi, A three-dimensional model of droplet impact and solidification, Int J Heat Mass Transf. 45 (2002) 2229–2242. https://doi.org/10.1016/S0017-9310(01)00336-2.

[220]S. Wildeman, C.W. Visser, C. Sun, D. Lohse, On the spreading of impacting drops, J Fluid Mech. 805 (2016) 636–655. https://doi.org/10.1017/jfm.2016.584.

[221]T. Bennett, D. Poulikakos, Splat-quench solidification: estimating the maximum spreading of a droplet impacting a solid surface, J Mater Sci. 28 (1993) 963–970. https://doi.org/10.1007/BF00400880.

[222]I. v Roisman, R. Rioboo, C. Tropea, Normal impact of a liquid drop on a dry surface: model for spreading and receding, Proceedings of the Royal Society of London. Series A: Mathematical, Physical and Engineering Sciences. 458 (2002) 1411–1430. https://doi.org/10.1098/rspa.2001.0923.

[223]Q. Huang, Y. Zhang, G. Pan, Dynamic Behaviors and Energy Transition Mechanism of Droplets Impacting on Hydrophobic Surfaces, Discrete Dyn Nat Soc. 2016 (2016) 1–9. https://doi.org/10.1155/2016/8517309.

[224]N.D. Patil, R. Bhardwaj, A. Sharma, Droplet impact dynamics on micropillared hydrophobic surfaces, Exp Therm Fluid Sci. 74 (2016) 195–206. https://doi.org/10.1016/j.expthermflusci.2015.12.006.

[225]N.A.C. Sidik, M.Z. Rafaty, Numerical Study of Droplet Dynamics on Solid Surface, in: 2010 Second International Conference on Computer Research and Development, IEEE, Kuala Lumpur, Malaysia, 2010: pp. 493–496. https://doi.org/10.1109/ICCRD.2010.106.

[226]G. Karapetsas, N.T. Chamakos, A.G. Papathanasiou, Efficient modelling of droplet dynamics on complex surfaces, Journal of Physics Condensed Matter. 28 (2016) 16. https://doi.org/10.1088/0953-8984/28/8/085101.

[227]H. Wang, Q. Wu, J. Okagaki, A. Alizadeh, J.A. Shamim, W.-L. Hsu, H. Daiguji, Bouncing behavior of a water droplet on a super-hydrophobic surface near freezing

temperatures, Int J Heat Mass Transf. 174 (2021) 121304. https://doi.org/10.1016/j.ijheatmasstransfer.2021.121304.

[228]Y. Guo, S. Shen, S. Quan, Numerical simulation of dynamics of droplet impact on heated flat solid surface, International Journal of Low-Carbon Technologies. 8 (2013) 134–139. https://doi.org/10.1093/ijlct/cts010.

[229]G. Trapaga, J. Szekely, Mathematical Modeling of the Isothermal Impingement of Liquid Droplets in Spraying Processes, (n.d.).

[230]J. Fukai, Z. Zhao, D. Poulikakos, C.M. Megaridis, O. Miyatake, Modeling of the deformation of a liquid droplet impinging upon a flat surface, Physics of Fluids A: Fluid Dynamics. 5 (1993) 2588–2599. https://doi.org/10.1063/1.858724.

[231]M. Pasandideh-Fard, Y.M. Qiao, S. Chandra, J. Mostaghimi, Capillary effects during droplet impact on a solid surface, Physics of Fluids. 8 (1996) 650–659. https://doi.org/10.1063/1.868850.

[232]S. Shin, D. Juric, Simulation of droplet impact on a solid surface using the level contour reconstruction method, Journal of Mechanical Science and Technology. 23 (2009) 2434–2443. https://doi.org/10.1007/s12206-009-0621-z.

[233]H.F. Wu, K.A. Fichthorn, • A Borhan, Á.A. Borhan, A. Borhan, An atomistic-continuum hybrid scheme for numerical simulation of droplet spreading on a solid surface Surface gradient operator, 50 (2014) 351–361. https://doi.org/10.1007/s00231-013-1270-4.

[234]S. Shin, D. Juric, Simulation of droplet impact on a solid surface using the level contour reconstruction method †, Journal of Mechanical Science and Technology. 23 (2009) 2434–2443. https://doi.org/10.1007/s12206-009-0621-z.

[235]P.V. Hobbs, Ice physics, Illustrate, Oxford University Press, 2010.

[236]B. Zobrist, T. Koop, B.P. Luo, C. Marcolli, T. Peter, Heterogeneous Ice Nucleation Rate Coefficient of Water Droplets Coated by a Nonadecanol Monolayer, The Journal of Physical Chemistry C. 111 (2007) 2149–2155. https://doi.org/10.1021/jp066080w.

[237]M. Mohammadi, M. Tembely, A. Dolatabadi, Predictive Model of Supercooled Water Droplet Pinning/Repulsion Impacting a Superhydrophobic Surface: The Role of the Gas-Liquid Interface Temperature, Langmuir. 33 (2017) 1816–1825. https://doi.org/10.1021/acs.langmuir.6b04394.

[238]B.J. Murray, S.L. Broadley, T.W. Wilson, J.D. Atkinson, R.H. Wills, Heterogeneous freezing of water droplets containing kaolinite particles, Atmos Chem Phys. 11 (2011) 4191–4207. https://doi.org/10.5194/acp-11-4191-2011.

[239]R.P. Sear, Quantitative studies of crystal nucleation at constant supersaturation: experimental data and models, CrystEngComm. 16 (2014) 6506–6522. https://doi.org/10.1039/C4CE00344F.

[240]D. Duft, T. Leisner, Laboratory evidence for volume-dominated nucleation of ice in supercooled water microdroplets, Atmos Chem Phys. 4 (2004) 1997–2000. https://doi.org/10.5194/ACP-4-1997-2004.

[241]B.J. Murray, S.L. Broadley, T.W. Wilson, S.J. Bull, R.H. Wills, H.K. Christenson, E.J. Murray, Kinetics of the homogeneous freezing of water, Physical Chemistry Chemical Physics. 12 (2010) 10380. https://doi.org/10.1039/c003297b.

[242]M.E. Earle, T. Kuhn, A.F. Khalizov, J.J. Sloan, Volume nucleation rates for homogeneous freezing in supercooled water microdroplets: Results from a combined

experimental and modelling approach, Atmos Chem Phys. 10 (2010) 7945–7961. https://doi.org/10.5194/ACP-10-7945-2010.

[243]S.M.A. Malek, G.P. Morrow, I. Saika-Voivod, Crystallization of Lennard-Jones nanodroplets: From near melting to deeply supercooled, J Chem Phys. 142 (2015) 124506. https://doi.org/10.1063/1.4915917.

[244]B. Krämer, O. Hübner, H. Vortisch, L. Wöste, T. Leisner, M. Schwell, E. Rühl, H. Baumgärtel, Homogeneous nucleation rates of supercooled water measured in single levitated microdroplets, J Chem Phys. 111 (1999) 6521. https://doi.org/10.1063/1.479946.

[245]W.J. Dunning, R.P. Andres, J. Lothe, G.M. Pound, R.A. Sigsbee, A.G. Walton, E. Hornbogen, D. Walton, F.P. Price, J.J. Hammel, E.A. Boucher, A. VanHook, Nucleation, Marcel Dekker, New York, NY, 1969.

[246]S. Akhtar, M. Xu, A.P. Sasmito, Development and validation of a semi-analytical framework for droplet freezing with heterogeneous nucleation and non-linear interface kinetics, Int J Heat Mass Transf. 166 (2021) 120734. https://doi.org/10.1016/j.ijheatmasstransfer.2020.120734.

[247]G. Chaudhary, R. Li, Freezing of water droplets on solid surfaces: An experimental and numerical study, Exp Therm Fluid Sci. 57 (2014) 86–93. https://doi.org/10.1016/J.EXPTHERMFLUSCI.2014.04.007.

[248]S. Gai, Z. Peng, B. Moghtaderi, J. Yu, E. Doroodchi, LBM modelling of supercooled water freezing with inclusion of the recalescence stage, Int J Heat Mass Transf. 146 (2020) 118839. https://doi.org/10.1016/J.IJHEATMASSTRANSFER.2019.118839.

[249]L. Gránásy, T. Pusztai, P.F. James, Interfacial properties deduced from nucleation experiments: A Cahn–Hilliard analysis, J Chem Phys. 117 (2002) 6157–6168. https://doi.org/10.1063/1.1502652.

[250]H. Vehkamäki, A. Määttänen, A. Lauri, I. Napari, M. Kulmala, Technical Note: The heterogeneous Zeldovich factor, Atmos Chem Phys. 7 (2007) 309–313. https://doi.org/10.5194/acp-7-309-2007.

[251]K.K.K. Tanaka, T. Yamamoto, K. Nagashima, K. Tsukamoto, A new method of evaluation of melt/crystal interfacial energy and activation energy of diffusion, J Cryst Growth. 310 (2008) 1281–1286. https://doi.org/10.1016/j.jcrysgro.2007.06.038.

[252]M.H. Kim, H. Kim, K.S. Lee, D.R. Kim, Frosting characteristics on hydrophobic and superhydrophobic surfaces: A review, Energy Convers Manag. 138 (2017) 1–11. https://doi.org/10.1016/j.enconman.2017.01.067.

[253]T.M. Schutzius, S. Jung, T. Maitra, P. Eberle, C. Antonini, C. Stamatopoulos, D. Poulikakos, Physics of icing and rational design of surfaces with extraordinary icephobicity, Langmuir. 31 (2015) 4807–4821. https://doi.org/10.1021/la502586a.

[254]S. Jung, M.K. Tiwari, N. Vuong Doan, D. Poulikakos, N.V. Doan, D. Poulikakos, Mechanism of supercooled droplet freezing on surfaces, Nat Commun. 3 (2012) 615. https://doi.org/10.1038/ncomms1630.

[255]S. Jung, M. Dorrestijn, D. Raps, A. Das, C.M. Megaridis, D. Poulikakos, Are superhydrophobic surfaces best for icephobicity?, Langmuir. 27 (2011) 3059–3066. https://doi.org/10.1021/la104762g.

[256]J.M. Hill, One-dimensional Stefan problems : an introduction, Illustrate, Longman Scientific & Technical, 1987.

https://books.google.com/books/about/One_dimensional_Stefan_Problems.html?id=3LjvAAAAMAAJ (accessed July 28, 2022).

[257]M. Stiti, G. Castanet, A. Labergue, F. Lemoine, Icing of a droplet deposited onto a subcooled surface, Int J Heat Mass Transf. 159 (2020) 120116. https://doi.org/10.1016/j.ijheatmasstransfer.2020.120116.

[258]C. Guo, D. Maynes, J. Crockett, D. Zhao, Heat transfer to bouncing droplets on superhydrophobic surfaces, Int J Heat Mass Transf. 137 (2019) 857–867. https://doi.org/10.1016/j.ijheatmasstransfer.2019.03.103.

[259]H.Y. Kim, J.H. Chun, The recoiling of liquid droplets upon collision with solid surfaces, Physics of Fluids. 13 (2001) 643–659. https://doi.org/10.1063/1.1344183.

[260]T. Wang, Y. Lü, L. Ai, Y. Zhou, M. Chen, Dendritic Growth Model Involving Interface Kinetics for Supercooled Water, Langmuir. 35 (2019) 5162–5167. https://doi.org/10.1021/ACS.LANGMUIR.9B00214/ASSET/IMAGES/LARGE/LA-2019-00214W_0002.JPEG.

[261]FLETCHER NH, Active Sites and Ice Crystal Nucleation, J Atmos Sci. 26 (1969) 1266–1271. https://doi.org/10.1175/1520-0469(1969)026<1266:asaicn>2.0.co;2.

[262]R.H. Perry, D.W. Green, Perry's Chemical Engineer: Handbook, 8th ed., McGraw-Hill Education, 2007. https://imtk.ui.ac.id/wp-content/uploads/2014/02/perrys-handbook-LENGKAP.pdf (accessed July 31, 2022).

[263]M.A. Floriano, C.A. Angell, Surface tension and molar surface free energy and entropy of water to -27.2 °C, Journal of Physical Chemistry. 94 (1990) 4199–4202. https://doi.org/10.1021/J100373A059/ASSET/J100373A059.FP.PNG_V03.

[264]W.S. Price, H. Ide, Y. Arata, Self-Diffusion of Supercooled Water to 238 K Using PGSE NMR Diffusion Measurements, J Phys Chem A. 103 (1999) 448–450. https://doi.org/10.1021/jp9839044.

[265]Q. Dang, M. Song, C. Dang, T. Zhan, L. Zhang, Experimental Study on Solidification Characteristics of Sessile Urine Droplets on a Horizontal Cold Plate Surface under Natural Convection, Langmuir. (2022). https://doi.org/10.1021/ACS.LANGMUIR.2C01154.

[266]C. Wang, X. Wu, P. Hao, F. He, X. Zhang, Study on a mesoscopic model of droplets freezing considering the recalescence process, Physics of Fluids. 33 (2021) 092001. https://doi.org/10.1063/5.0064976/5.0064976.MM.ORIGINAL.V2.AVI.

[267]M. Amiriafshar, M. Rafieazad, X. Duan, A. Nasiri, Fabrication and coating adhesion study of superhydrophobic stainless steel surfaces: The effect of substrate surface roughness, Surfaces and Interfaces. 20 (2020) 100526. https://doi.org/10.1016/j.surfin.2020.100526.

[268]W.G. Bae, K.Y. Song, Y. Rahmawan, C.N. Chu, D. Kim, D.K. Chung, K.Y. Suh, One-Step Process for Superhydrophobic Metallic Surfaces by Wire Electrical Discharge Machining, ACS Appl Mater Interfaces. 4 (2012) 3685–3691. https://doi.org/10.1021/am3007802.

Appendix A Droplet Freezing Delay on Regularly Roughened Stainless Steel Surfaces[6]

A.1 Introduction

Appendix A presents the droplet freezing delay on regularly roughened stainless-steel surfaces at room temperature. Section A.2 shows the experimental setups, and section A.3 presents the characterization of the sample surface. An uncertainty analysis is demonstrated in section 0. A detailed heat transfer analysis is presented in section A.5. Section A.6 shows the major conclusions from this study.

A.2 Experimental apparatus and procedure

Figure A-1 shows the apparatus for the water droplet impact and freezing experiments on regularly roughened stainless-steel surfaces. It consists of a heavy-duty stand (Fisher Scientific) with a tilting base (World Precision Instruments, Stand Tilting, M-3) of adjustable inclination angles, a cold plate (AAVID Thermally) that is mounted on the tilting base to control the temperature of the sample surface, and a thermoelectric cooler (TE Technology) where a copper tubing of 1/16 inch diameter (Sigma-Aldrich) is used for

---

[6] The main content in this chapter is a part of a previously published paper (K. Shi, X. Duan, Heat Transfer Analysis of Icing Process on Metallic Surfaces of Different Wettabilities, in: H. Okada, S.N. Atluri (Eds.), Comput. Exp. Simulations Eng., Springer, Cham, 2020: pp. 201–206.) The author of this thesis is the first author of the published paper. The first author conducted droplet freezing delay experiments on regularly roughened stainless-steel surfaces at room temperature, identified the research topic, analyzed data, prepared the manuscripts and the corresponding revisions. Dr. Xili Duan, as the second author, provided his professional suggestions on this topic and assisted in preparing the manuscript and the corresponding revisions.

generating water droplets with controllable temperatures. Water comes from a syringe pump (Harvard, Syringe pump, MMP 3.3, not shown in this diagram). The cold plate is connected to a thermal bath (Fisher Scientific, ISO TEMP 6200), which provides control of the surface temperature of the testing samples.

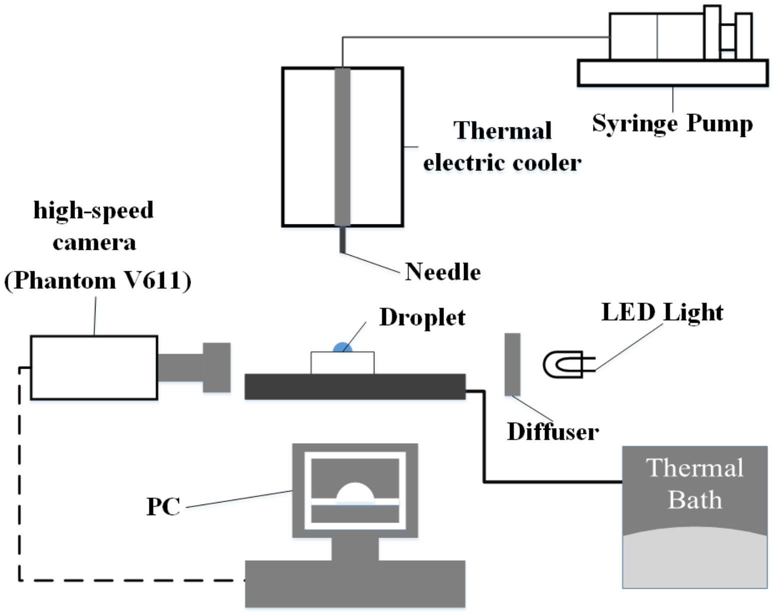

Figure A-1 Schematic of the experimental system, and the figure is adapted from [90] with the permission of Elsevier Science and Technology Journals.

High speed imaging was used to record the droplet dynamics and freezing process with a high-speed camera (Vision Research, Phantom V611). The camera is connected to a laptop for video and picture capturing. An LED light and a light diffuser (Edmund Optics, OPAL 50 mm) were used to provide proper light for the imaging process. The temperatures of the sample surfaces and droplets are measured by an infrared camera (FLIR). The droplet dynamics and freezing parameters (detailed in the next section) can be determined by analyzing the images taken by the high-speed camera.

This study investigates the effects of surface temperature, droplet impact velocity, surface inclined angle, droplet diameter, and surface wettability (static and dynamic contact angles) on droplet impact dynamics. The total icing time is defined as the time measured from when the droplet first impacts a sample surface until it is fully frozen. Five runs are conducted at each condition to minimize random experimental uncertainty. After each run, the sample surface was washed with deionized water and completely dried before the next run.

A.3 Sample surfaces

Table A-1 Sample surfaces with different wettability

Sample name	θ_s (°)	θ_a (°)	CAH (°)
ON	77 ± 3	88 ± 3	36 ± 3
Channel 1	112 ± 5	132 ± 5	27 ± 5
Channel 2	124 ± 5	123 ± 5	38 ± 5
Coated channel 1	128 ± 5	135 ± 5	31 ± 5
Varied channel	130 ± 5	149 ± 5	20± 5
Coated channel 2	139 ± 5	149 ± 5	20 ± 5
Coated varied channel	145 ± 4	150 ± 4	21 ± 4

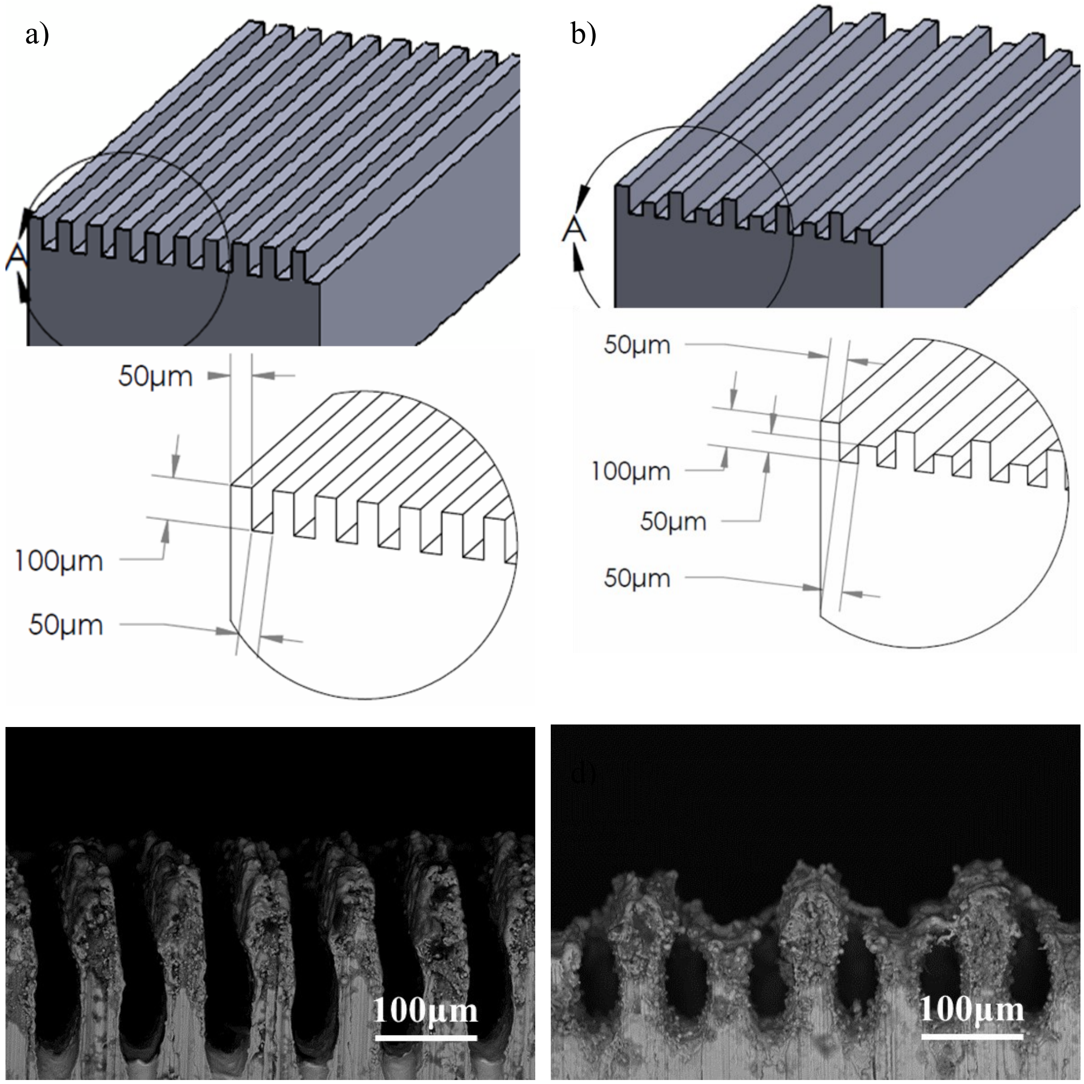

Figure A-2 Design drawings (a, b) and SEM images (c, d) of Channel 2 and Varied channel surfaces. The figure is adapted from [90] with the permission of Elsevier Science and Technology Journals.

A total of seven engineered surfaces with various wettability are used in the experiments and listed in Table A-1. The material is stainless steel (17-4 PH) for all samples. The ON had no mechanical machining or coating. Channel 1 is a 20×20 mm surface machined by wire electrical discharge machining (WEDM) [268]. Channel 2 and the Varied channel are 30×20 mm surfaces with micro/nano texturing fabricated with a nanosecond laser [140]. Figure A-2 shows detailed designs of the two micro-scale channels and scanning electron microscope (SEM) images showing the actual surface morphology after laser machining. Samples of these 3 designs were also coated with a low surface energy material, i.e., Aculon [140] to further increase their hydrophobicity. The more detailed sample preparation procedures have been presented in [90,140]. The static and dynamic contact angles of each sample surface, listed in Table A-1, was measured by a contact angle instrument (Dataphysics, OCA 15EC). Five measurements were taken for each sample, and the average values were used.

A.4 Uncertainties analysis

The uncertainties include precision errors obtained from equipment manuals and random errors within multiple measurements. The method of Kline and McClintock [190] has been used to determine the uncertainties of average heat transfer rate, heat transfer coefficient and other dimensionless parameters. Table A-2 represents the uncertainties in these experiments and heat transfer analysis.

Table A-2 Uncertainties

Parameters	Uncertainties
T_i and T_w	± 0.1°C and ± 1 °C
D_i and $t_{freezing}$	± 10 µm and ± 0.5 ms
We and We_i	± 0.5%.and ± 4%
Q_V and Q	± 0.9% and ± 1.9%

$\bar{q}$ and D_c^*	± 1.9% and ± 0.3%

A.5 Heat transfer analysis of the icing process

Icing experiments on horizontal surfaces were conducted under different conditions. The temperatures of the sample surfaces were controlled at T_w = -10 °C. The initial droplet diameters D_i were 1.80 mm. The droplet impact speeds varied from 0.77 m/s, 0.99 m/s, to 1.17 m/s. The initial droplet temperature was kept at T_i = 5 ºC. All experiments were conducted under approximately the same room air temperature (~ 15 °C) and relative humidity (~ 30%).

The heat transfer analysis is the same as in section 5.5.

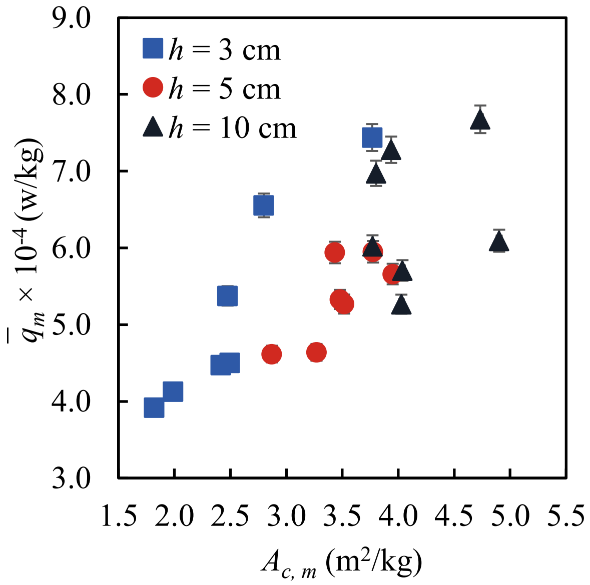

Figure A-3 The average cooling rates of droplets icing changed with final contact areas

Figure A-3 shows the average cooling rates $\bar{q}$ varied with the final contact areas A_c of droplets on different target surfaces. $\bar{q}$ tends to increase while the contact areas A_c is rising. This indicates that a higher contact area leads to a higher cooling rate, which is also indicated in Eq. 1. This contact area is the key to the cooling process of droplets icing on cold surfaces. It relates to the surface wettability and impact velocities of droplets.

Figure A-4 shows the variations of A_c^* with (a) the θ_s (static contact angle of water droplets on target surfaces) and (b) the We_i number. A_c^* decreases when the θ_s increases, i.e., a better wetting condition will lead to a larger final contact area. In other words, a water droplet will extend wider when it impacts a surface with better wettability, and the final contact area of a water droplet will be smaller when it impacts a more hydrophobic surface. Also, a higher We_i number leads to a larger A_c^* of water droplets. In addition, lower We_i means a lower impact speed on the same target surface or a droplet impact under the same speed on a poor wetting surface.

Figure A-4b demonstrates that a lower We_i leads to a smaller A_c^* of water droplets, which means that a droplet impacts under the same speed on a poor wetting surface will result in a smaller final contact area.

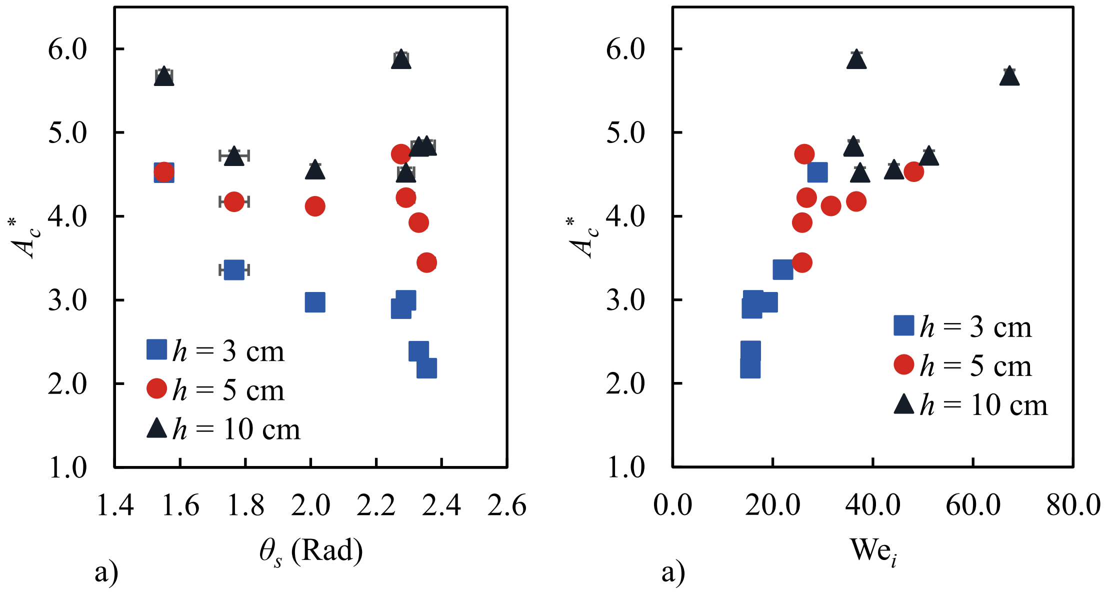

a) a)

Figure A-4 a) D_c^* of water droplets with different impact speeds changed with SAC (rad); b) D_c^* of water droplets varied with We_i number.

The experimental results demonstrate that hydrophobic or superhydrophobic surfaces can delay the icing process of a droplet, because the final contact area A_c of a water droplet on the surface decreases, which contributes to a relatively lower cooling rate for these surfaces.

A.6 Summary

The average cooling rate $\bar{q}$ is proportional to the final droplet-surface contact area A_c. A better wetting condition contributes to a larger final contact area A_c. This means hydrophobic or super-hydrophobic surfaces will have smaller contact areas and delay the cooling process of a droplet on it. Lower impact Weber number, due to lower impact velocity or a poor wetting surface, results in smaller D_c^* of water droplets, i.e., smaller final contact area A_c. So, for droplets with the same impact velocity, a poor wetting surface will lead to smaller final contact area A_c and a lower average cooling rate $\bar{q}$, resulting in icing delay.

Appendix B Hybrid Ice Protection Techniques[7]

B.1 Introduction

The passive techniques discussed above cannot achieve complete anti-icing in severe icing conditions, for example, in high humidity marine environments. The conventional active anti-icing/de-icing methods consume significant energy and may damage the substrate. With these limitations from either the passive or active techniques, researchers have been trying to investigate several hybrid ice protection techniques, i.e., a combination of active and passive techniques: electrothermal air isolating surfaces is presented in section B.2. Section B.3, section B.4 and section B.5 illustrate the electrothermal SLIPS, Phase change materials combined with SLIPS, and the photothermal technique integrated with air/oil isolating surfaces, respectively. Section B.6. presents the major conclusions from this review.

---

[7] The main content in this chapter is a part of a previously published paper (K. Shi, X. Duan, A Review of Ice Protection Techniques for Structures in the Arctic and Offshore Harsh Environments, J. Offshore Mech. Arct. Eng. 143 (2021).) The author of this thesis is the first author of the published paper. The first author conducted a comprehensive study on ice protection techniques for structures in the arctic and offshore harsh environments, identified the research topic, prepared the manuscripts and the corresponding revisions. Dr. Xili Duan, as the second author, provided his professional suggestions on this topic and assisted in preparing the manuscript and the corresponding revisions.

B.2 The electrothermal superhydrophobic surface

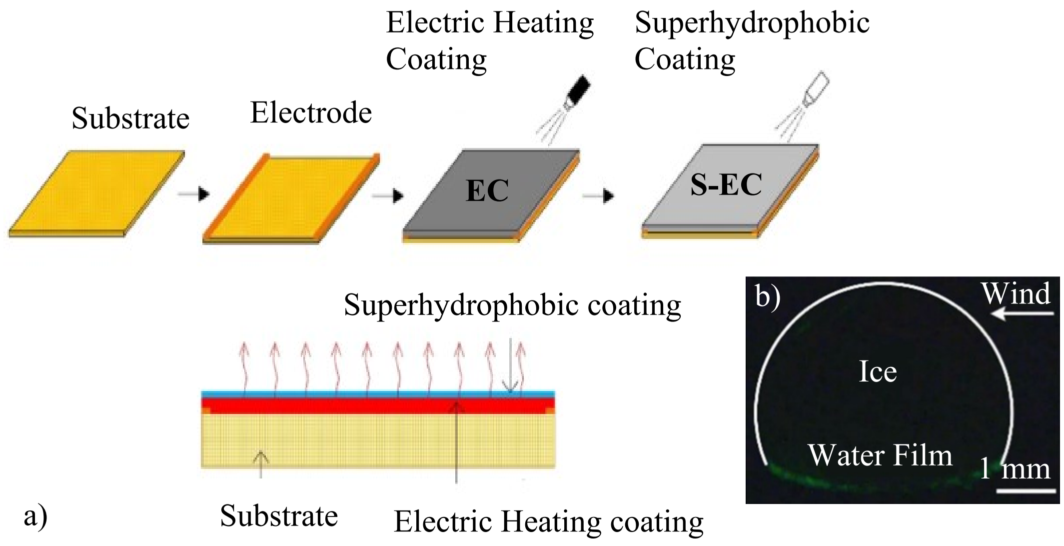

Figure B-1 Schematic of the fabrication process and the heating mode of a) superhydrophobic electrical heating coating (S-EC). The momentary fluorescence images of the ice drop before it was precisely blown away on (b) S-EC. The figure is adapted from [61] with the permission of Elsevier Science and Technology Journals.

A combination of electrical heating methods and superhydrophobic surfaces is investigated by Zhao et al. [61]. Figure B-1a presents the fabrication of the electrothermal superhydrophobic surface. The prepared electric heating coating dispersion was sprayed on the substrate with a copper foil electrode pasted on; the sample was heated at 50°C for 12 h to cure and obtain the electric heating coating (EC). The hydrophobic fumed silica was dispersed into the EC substrate to obtain the electrothermal superhydrophobic surface (S-EC). The superhydrophobic electric heating coating (S-EC) shows outstanding energy-saving performance in anti-icing/de-icing tests and realizes anti-icing in low temperatures (up to 58% heating power saving compared to traditional embedded heating mode discussed in Section 3.1, and the anti-icing temperature is about 7 °C). The feasibility of S-EC applied on rotating blades or irregular surfaces is verified by Zhao et al. [61]. However, the application on a metal surface is unknown, and it is quite power-consuming (4.1 kW/m^2) when applied to a large area for de-icing. The cost is also high for offshore structures due to the large coated area. The application requires an additional power source. Therefore, it is not applicable for stairs and working areas due to potential electrical shock hazards in offshore environments.

B.3 The electrothermal SLIPS technique

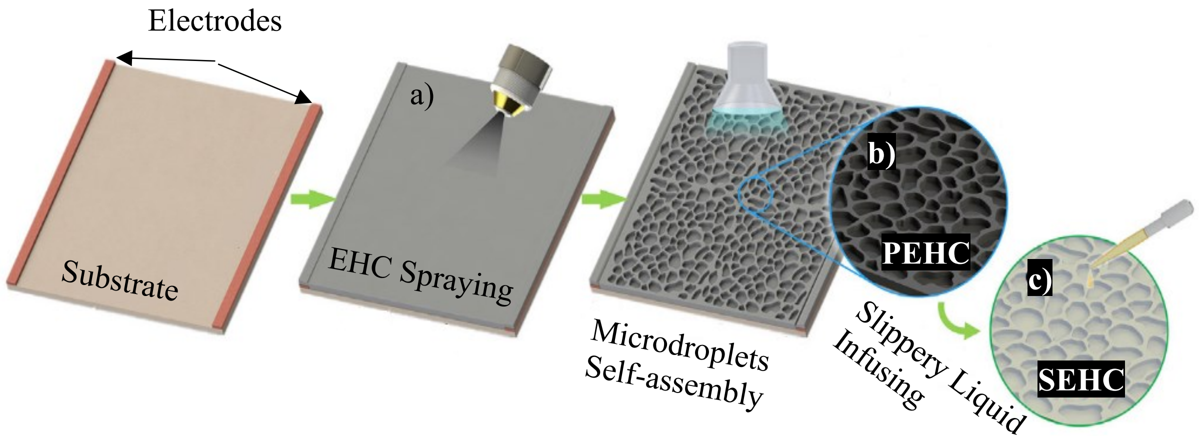

Figure B-2 Schematic of the fabrication of porous electric heating coatings: (a) smooth electrical heating coating (EHC), (b) EHC with close-aligned micropores (PEHC), (c) slippery silicone oil-infused PEHC (SEHC). The figure is adapted from [63] with the permission of Elsevier Science and Technology Journals.

This technique is a combination of electric heating coating and the SLIPS. The fabrication process is shown in Figure B-2. As verified experimentally, the slippery silicone oil-infused electric heating coating (SEHC) can significantly reduce ice adhesion strength. The ice adhesion on the smooth electric heating coating (EHC) is 1940 ± 210 kPa, while the adhesion strength on EHC with close-aligned micropores (PEHC) is 2770 ± 210 kPa. In comparison, the adhesion strength of ice on SEHC with close-aligned micropores (SEHC) is only 58 ± 7 kPa, which significantly decreases. Also, the SEHC has a power consumption of 0.58 W/cm^2, which is 53% and 23% lower than the smooth electric heating coating (EHC) and dry porous electrical heating coating (PEHC), respectively. The durability of SEHC is also better than S-EC [63]. However, it has the same disadvantages as S-EC, and its application on ships and offshore structures is limited because of the large metal surfaces on these structures (leading to high cost). The application requires an additional power source. Therefore, it is not applicable for stairs and working areas due to the potential to create electrical shock hazards in offshore environments.

B.4 Phase change materials (PCMs) integrated with SLIPS

Some researchers integrated the phase switching liquids (PSLs) with SLIPS and achieved excellent anti-icing performance. Figure B-3 illustrates a phase transition SLIPS (PTSLIPS) infused with peanut oil. The PTSLIPS inherits the advantages of SLIPS; it can self-repair even after bulk damage. When the ambient temperature is higher than 3 ºC, the lubricant in the liquid phase can flow to the damaged part by its surface tension. The peanut oil will solidify and remain in the solid phase when the temperature is below 0 ºC. The solidified peanut oil can prevent the lubricant from depleting, which compensates for the disadvantage of SLIPS and extends the durability of PTSLIPS. It was shown that the

PTSLIPS could reduce the ice adhesion strength to 16-20 kPa even after 30 icing and melting cycles. Also, after some mechanical damage, the ice adhesion strength remains in the range of 20-26 kPa [115].

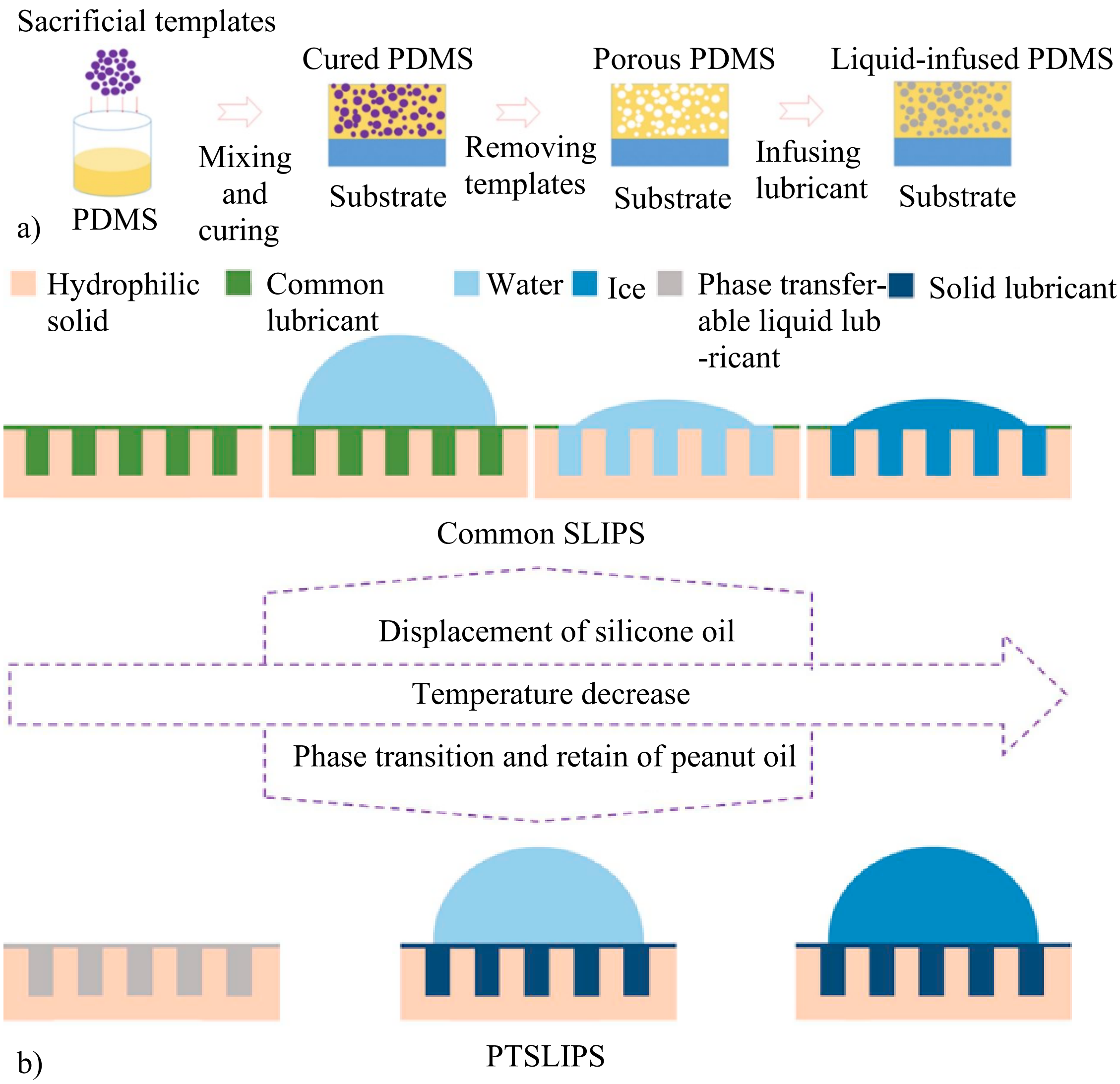

Figure B-3 Schematic of the PTSLIPS: a) fabrication procedure, b) the stability of SLIPS incused by silicone oil (top) and PTSLIPS infused by peanut oil (bottom) during the freezing process. The figure is adapted from [115] with the permission of Elsevier Science and Technology Journals.

Zhu et al. investigated the anti-icing performance of phase change microcapsules integrated with low surface energy materials (vulcanized (RTV) silicone rubber and fluorosilicone copolymers (FS)) [116]. The base material was aluminium. The ice adhesion strength on the vulcanized (RTV) silicone rubber phase change microcapsules (RTV/PCM) coating surfaces is in the range of 102-132 kPa, which is relatively lower than the ice adhesion strength on fluorosilicone copolymer phase change microcapsules (FS/PCM) coating surfaces (378-489 kPa). Also, the freezing delay of a water droplet on the RTV/PCM surface (98 s) is slightly longer than that with FS/PCM (84 s). However, the ice adhesion strengths are still much higher than those on the previously discussed icephobic surfaces (< 100 kPa) [87,89,92–95]. Further, the chemical and mechanical durability of these coatings has not yet been evaluated.

The applications of PCM on offshore and marine structures depend on the properties of PCMs used. PSLs can not be applied to marine facilities due to safety considerations. PTSLIPS are promising and could be applied to offshore superstructures, such as radars and antennas, but cannot be applied on decks, stairs, working areas, and lower structures because of their unknown abrasive and corrosive performance [93,104] and the possibility of slipping hazards.

B.5 The photothermal technique integrated with air/ oil film isolating surfaces

The photothermal technique can be integrated with some passive ice protection technologies. Cheng et al. 2015 investigated magnetic particle-based superhydrophobic coatings with a water contact angle of 160 ± 0.3º and contact angle hysteresis of 1.0 ± 0.6º [119]. The coatings can be sprayed on glass or silicon substrates. The surface temperature increases significantly when the coated substrate is in an alternating magnetic field or under solar/light irradiation. Figure B-4 illustrates the anti-icing and de-icing performance of magnetic particle-based super-hydrophobic coatings. They found that this coating can delay icing for 2878s (compared to 50s for the uncoated surface) and reduce the ice adhesion strength from 399.9 ± 138 kPa to 213.7 ± 6.9 kPa [119].

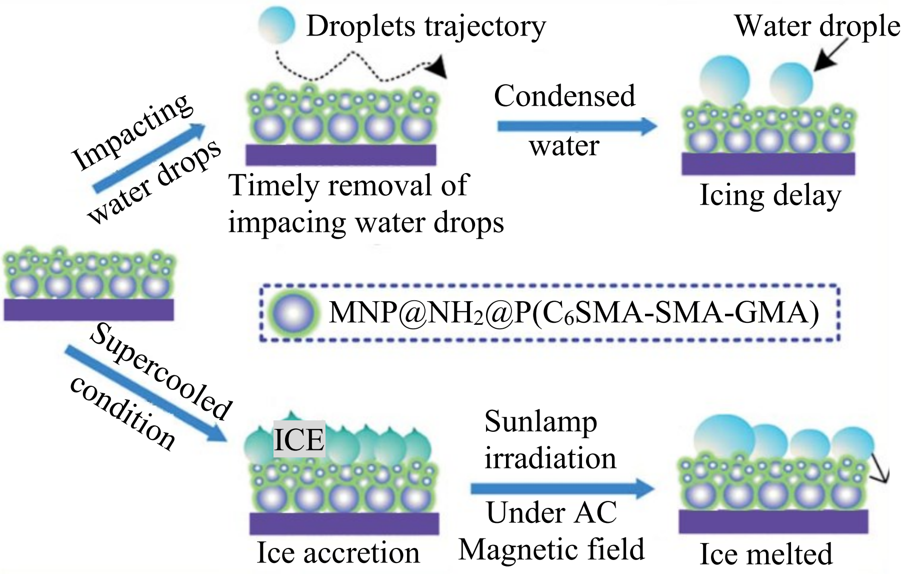

Figure B-4 Schematic of anti/de-icing properties on surfaces coated with a magnetic particle-based superhydrophobic coating. The figure is adapted from [119] with the permission of the Royal Society of Chemistry.

Fe_3O_4 nanoparticles have a high-efficiency photothermal effect under near-infrared irradiation. Yin et al. present a self-lubricated photothermal coating shown in Figure B-5 that has integrated the SLIPS with photothermal capabilities [120]. Firstly, the polystyrene microspheres are placed onto the substrate as a colloidal crystals template. Secondly, the silicone precursor with Fe_3O_4 nanoparticles is poured into the prepared template. Before the porous film is perfluorinated with perfluorosilane and filled with perfluoropolyether lubricants, the polystyrene microsphere template is removed. The coating can be sprayed on various substrates. However, the fabrication process is expensive, time-consuming, and cannot be applied to large-scale applications.

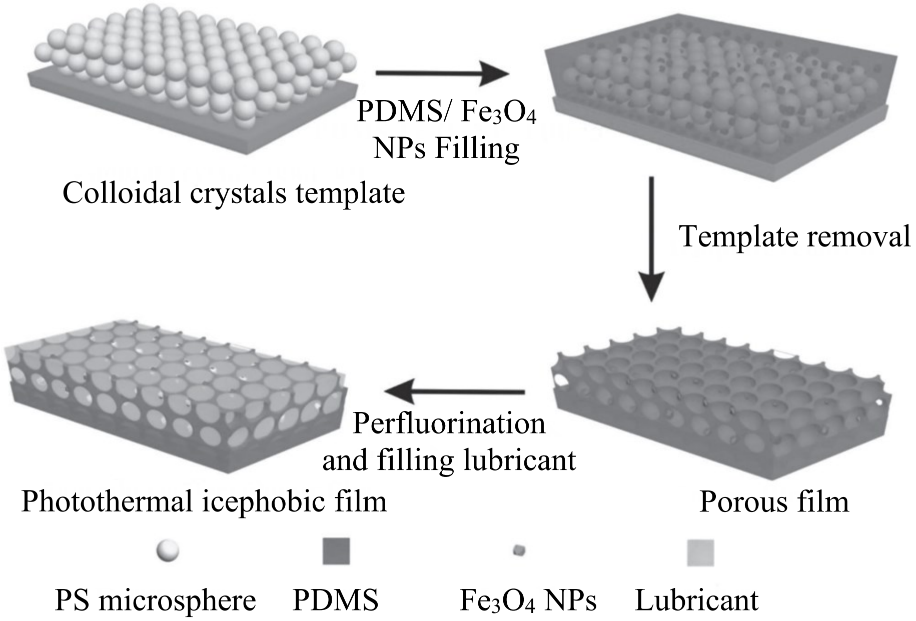

Figure B-5 Schematic procedures for fabricating photothermal icephobic film. The figure is adapted from [120] with the permission of the Royal Society of Chemistry.

Mitridis et al. designed an ultra-thin hybrid plasmonic metasurface with nanocomposites of gold and titanium dioxide [122], illustrated in Figure B-6. This coating is transparent and absorbs broadband visible light, which can increase the surface temperature to achieve de-icing. However, the materials are very expensive, and the coating cannot be applied to large-scale surfaces.

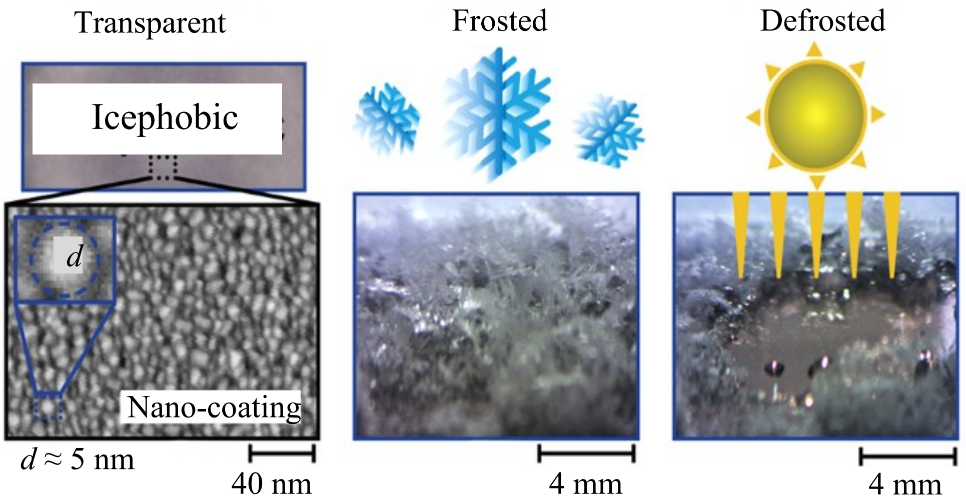

Figure B-6 Schematic of metasurfaces for sunlight-driven icephobicity. The figure is adapted from [122] with the permission of the American Chemical Society.

The hybrid photothermal technologies allow for remote de-icing. They can be applied to existing systems, and the photothermal materials can absorb solar irradiation to increase the surface temperature above the freezing point of water. Also, melting a thin layer of ice can significantly decrease the adhesion strength between ice and substrate, and the rest of the ice cap can be removed by gravity or moderate wind power [108,121]. These techniques have the same application potential as the photothermal methods discussed in section 2.3.5. For example, they can be applied on antennas, radar, walkways, stairs, cranes, windlasses, valves, firefighting and rescue equipment, and air intakes. However, this technology can be applied only in areas in direct sunlight or with additional illumination (LEDs or infrared lamps) [121]. The additional illumination can be more expensive than other active ice protection methods, such as direct heating. Ice can be formed during the night or the day in poor weather conditions. Further efforts are required for this method to be applied to offshore structures and marine vessels.

B.6 Summary

In the Arctic and harsh environments, effective anti/de-icing techniques allow for the safe operation of offshore facilities and marine transportation vessels and protect the safety of workers. Many ice protection techniques that are being used or can be potentially applied to offshore structures and marine vessels in these harsh environments (low temperature, high humidity and salinity) have been evaluated. These techniques have been divided into three categories based on their need for additional energy sources, i.e., the active, passive, and hybrid ice protection techniques.

The active methods require an extra energy supply, human power, extra space, or control systems, which can be expensive, energy-intensive, or environmentally damaging. The passive ice protection techniques require no additional energy; instead, they prevent or delay icing or reduce ice adhesion with the surface icephobic properties. This can significantly lower the operational cost. However, most passive techniques have limitations; for example, air isolating film surfaces are intolerant of high-humidity environments. Also, lubricants of oil isolating film surfaces, such as SLIPS, can be depleted after several cycles of freezing and melting. The water film lubricating layer can be slippery and potentially create slipping hazards for individuals working on the surfaces. The application of phase change materials (PCMs) for offshore structures depends on the properties of the materials being used. PSLs can not be applied to marine facilities due to safety considerations. PTSLIPS are promising and can be applied to offshore superstructures but cannot be applied on decks, stairs, working areas, and lower structures because of the unknown abrasive and corrosive performance and potential for slipping hazards. The newly proposed LIT materials/coatings are promising passive ice protection technologies. However, the durability of LIT materials requires further investigation.

It is difficult to achieve adequate ice protection in harsh environments with a single active or passive technique based on extensive studies. The cost of implementation and maintenance for active anti/de-icing approaches is too high for long-term use. Some passive ice protection techniques can delay icing, but they cannot prevent long-term ice formation completely, which leads to the eventual rapid accumulation of ice. The hybrid techniques combine multiple active and passive methods to take advantage of both techniques; for example, the electrothermal air film isolating surfaces and electrothermal SLIPS. Still, the application of these techniques is limited due to the potential of electrical shock hazards in offshore environments. There are more options for combining active and passive techniques or passive and passive techniques; for example, PCMs/PSLs integrated with SLIPS, where the combination of two passive anti/de-icing approaches presents excellent anti-icing performance. The photothermal technique integrated with air/ oil film isolating surfaces is promising but with limitations for different applications. Further investigation is required for the development and application of hybrid techniques.

Appendix C Uncertainty Analysis

The Uncertainty of Initial Droplet Diameter D_i

$$\begin{aligned} A_i &= \frac{\pi D_i^2}{4} \\ D_i &= \sqrt{\frac{4A_i}{\pi}} \\ U_{D_i} &= \sqrt{\left(\frac{\partial D_i}{\partial A_i}\right)^2 U_{A_i}^2} = \sqrt{\left(\sqrt{\frac{4}{\pi}} \cdot \frac{1}{2\sqrt{A_i}}\right)^2 \cdot U_{A_i}^2} \end{aligned} \tag{C-1}$$

The Uncertainty of Initial Droplet Volume V

$$\begin{aligned} V_D &= \frac{4}{3}\pi\left(\frac{D_i}{2}\right)^3 = \frac{\pi}{6} D_i^3 \\ U_{D_i} &= \sqrt{\left(\frac{\partial V}{\partial D_i}\right)^2 U_{D_i}^2} = \sqrt{\left(\frac{\pi}{2} D_i^2\right)^2 \cdot U_{D_i}^2} \end{aligned} \tag{C-2}$$

The Uncertainty of Sphere Radius R

$$\begin{aligned} R &= \frac{D_c}{2\sin\theta} \\ U_R &= \sqrt{\left(\frac{\partial R}{\partial D_c}\right)^2 U_{D_c}^2 + \left(\frac{\partial R}{\partial \sin\theta}\right)^2 U_\theta^2} = \sqrt{\left(\frac{1}{2\sin\theta}\right)^2 \cdot U_{D_c}^2 + \left(-\frac{D_c}{2\sin^2\theta}\right)^2 U_{\sin\theta}^2} \end{aligned} \tag{C-3}$$

The Uncertainty of Cap Height H

$$\begin{aligned} H &= R\left(1-\cos\theta\right) \\ U_H &= \sqrt{\left(\frac{\partial H}{\partial R}\right)^2 U_R^2 + \left(\frac{\partial H}{\partial \cos\theta}\right)^2 U_{\cos\theta}^2} = \sqrt{\left(1-\cos\theta\right)^2 \cdot U_R^2 + \left(-R\right)^2 U_{\cos\theta}^2} \end{aligned} \tag{C-4}$$

The Uncertainty of Cap Volume V

$$V = \pi H^2 \left(R - \frac{H}{3} \right)$$

$$U_V = \sqrt{\left(\frac{\partial H}{\partial V} \right)^2 U_H^2 + \left(\frac{\partial R}{\partial \cos\theta} \right)^2 U_R^2} = \sqrt{\left(2\pi R \cdot H - \pi H^2 \right)^2 \cdot U_H^2 + \left(\pi H^2 \right)^2 U_R^2} \qquad \text{(C-5)}$$

The Uncertainty of Final contact area A_c

$$A_c = \frac{\pi D_c^2}{4}$$

$$U_{A_c} = \sqrt{\left(\frac{\partial A_c}{\partial D_c} \right)^2 U_{A_i}^2} = \sqrt{\left(\frac{\pi D_c}{2} \right)^2 \cdot U_{D_c}^2} \qquad \text{(C-6)}$$

The Uncertainty of Falling Time t_f

$$t_f = \sqrt{\frac{2h}{g}}$$

$$U_{t_f} = \sqrt{\left(\frac{\partial t_f}{\partial h} \right)^2 U_h^2} = \sqrt{\left(\sqrt{\frac{2}{g}} \cdot \frac{1}{2\sqrt{h}} \right)^2 \cdot U_h^2} \qquad \text{(C-7)}$$

The Uncertainty of The Average Convective Heat Transfer Coefficient $\overline{h_D}$

$$\overline{h_D} = \frac{\overline{Nu_D} k}{D_i} = \frac{k(2 + 0.6 Re_D^{1/2} Pr^{1/3})}{D_i}$$

$$U_{\overline{h_D}} = \sqrt{\left(\frac{\partial \overline{h_D}}{\partial D_i} \right)^2 U_{D_i}^2} = \sqrt{\left(-\frac{k(2 + 0.6 Re_D^{1/2} Pr^{1/3})}{D_i^2} \right)^2 \cdot U_{D_i}^2} \qquad \text{(C-8)}$$

The Uncertainty of Droplet Impact Temperature T_{impact}

$$
\begin{aligned}
T_{impact} &= \left(T_i - T_\infty\right)\cdot \exp\left[-\left(\frac{\overline{h_D}A_D}{\rho V_D c_p}\right)\cdot\sqrt{\frac{2h}{g}}\right] + T_\infty \\
&= \left(T_i - T_\infty\right)\cdot \exp\left[-\left(\frac{6\overline{h_D}}{\rho D_i c_p}\right)\cdot\sqrt{\frac{2h}{g}}\right] + T_\infty
\end{aligned}
$$

$$
U_{T_{impact}} = \sqrt{\begin{aligned}&\left(\frac{\partial T_{impact}}{\partial T_i}\right)^2 U_{T_i}^2 + \left(\frac{\partial T_{impact}}{\partial T_\infty}\right)^2 U_{T_\infty}^2 + \left(\frac{\partial T_{impact}}{\partial \overline{h_D}}\right)^2 U_{\overline{h_D}}^2 \\ &+ \left(\frac{\partial T_{impact}}{\partial D_i}\right)^2 U_{D_i}^2 + \left(\frac{\partial T_{impact}}{\partial h}\right)^2 U_h^2\end{aligned}} \tag{C-9}
$$

$$
U_{T_{impact}} = \sqrt{\begin{aligned}
&\left\{\exp\left[-\left(\frac{6\overline{h_D}}{\rho D_i c_p}\right)\cdot\sqrt{\frac{2h}{g}}\right]\right\}^2 U_{T_i}^2 \\
&+\left\{1-\exp\left[-\left(\frac{6\overline{h_D}}{\rho D_i c_p}\right)\cdot\sqrt{\frac{2h}{g}}\right]\right\}^2 U_{T_\infty}^2 \\
&+\left\{\left(T_i - T_\infty\right)\cdot\left[-\left(\frac{6}{\rho D_i c_p}\right)\cdot\sqrt{\frac{2h}{g}}\right]\cdot\exp\left[-\left(\frac{6\overline{h_D}}{\rho D_i c_p}\right)\cdot\sqrt{\frac{2h}{g}}\right]\right\}^2 U_{\overline{h_D}}^2 \\
&-\left\{\frac{\left(T_i - T_\infty\right)\cdot\left[-\left(\frac{6\overline{h_D}}{\rho c_p}\right)\cdot\sqrt{\frac{2h}{g}}\right]\cdot\exp\left[-\left(\frac{6\overline{h_D}}{\rho D_i c_p}\right)\cdot\sqrt{\frac{2h}{g}}\right]}{D_i^2}\right\}^2 U_{D_i}^2 \\
&+\left\{\frac{\left(T_i - T_\infty\right)\cdot\exp\left[-\left(\frac{6\overline{h_D}}{\rho D_i c_p}\right)\cdot\sqrt{\frac{2h}{g}}\right]}{2\sqrt{h}}\right\}^2 U_h^2
\end{aligned}}
$$

The Uncertainty of the Total Heat Transfer Q

$$Q = Q_v \cdot V_D = -\rho V_D c_p (T_f - T_{\text{impact}}) + \rho V_D H_{ls}$$
$$U_Q = \sqrt{\left(\frac{\partial Q}{\partial V_D}\right)^2 U_{V_D}^2 + \left(\frac{\partial Q}{\partial T_{\text{impact}}}\right)^2 U_{T_{\text{impact}}}^2} \qquad \text{(C-10)}$$
$$U_Q = \sqrt{\left(-\rho c_p (T_f - T_{\text{impact}}) + \rho H_{ls}\right)^2 U_{V_D}^2 + \left(\rho V_D c_p\right)^2 U_{T_{\text{impact}}}^2}$$

The Uncertainty of the Average Freezing Rate $\bar{q}$

$$\bar{q} = \frac{Q}{t_{freezing}}$$
$$U_{\bar{q}} = \sqrt{\left(\frac{\partial \bar{q}}{\partial Q}\right)^2 U_Q^2 + \left(\frac{\partial \bar{q}}{\partial t_{freezing}}\right)^2 U_{t_{freezing}}^2} = \sqrt{\left(\frac{1}{t_{freezing}}\right)^2 U_Q^2 + \left(-\frac{Q}{t_{freezing}^2}\right)^2 U_{t_{freezing}}^2} \qquad \text{(C-11)}$$

The Uncertainty of the Average Freezing Rate per Mass $\overline{q_m}$

$$\overline{q_m} = \frac{\bar{q}}{m_D} = \frac{\bar{q}}{\rho V_D}$$
$$U_{\overline{q_m}} = \sqrt{\left(\frac{\partial \overline{q_m}}{\partial \bar{q}}\right)^2 U_{\bar{q}}^2 + \left(\frac{\partial \overline{q_m}}{\partial V_D}\right)^2 U_{V_D}^2} = \sqrt{\left(\frac{1}{\rho V_D}\right)^2 U_{\bar{q}}^2 + \left(-\frac{\bar{q}}{\rho V_D^2}\right)^2 U_{V_D}^2} \qquad \text{(C-12)}$$

The Uncertainty of the Average Freezing Rate per Volume $\overline{q_V}$

$$\overline{q_V} = \frac{\bar{q}}{V_D}$$
$$U_{\overline{q_V}} = \sqrt{\left(\frac{\partial \overline{q_V}}{\partial \bar{q}}\right)^2 U_{\bar{q}}^2 + \left(\frac{\partial \overline{q_V}}{\partial V_D}\right)^2 U_{V_D}^2} = \sqrt{\left(\frac{1}{V_D}\right)^2 U_{\bar{q}}^2 + \left(-\frac{\bar{q}}{V_D^2}\right)^2 U_{V_D}^2} \qquad \text{(C-13)}$$

The Uncertainty of the Dimensionless Final Contact Diameter D_c^*

$$D_c^* = \frac{D_c}{D_i}$$

$$U_{D_c^*} = \sqrt{\left(\frac{\partial D_c^*}{\partial D_c}\right)^2 U_{D_c}^2 + \left(\frac{\partial D_c^*}{\partial D_i}\right)^2 U_{D_i}^2} = \sqrt{\left(\frac{1}{D_i}\right)^2 U_{D_c}^2 + \left(-\frac{D_c}{D_i^2}\right)^2 U_{D_i}^2} \quad \text{(C-14)}$$

The Uncertainty of the Dimensionless Final Contact Area $A_c{}^*$

$$A_c^* = \frac{A_c}{A_i}$$

$$U_{A_c^*} = \sqrt{\left(\frac{\partial A_c^*}{\partial A_c}\right)^2 U_{A_c}^2 + \left(\frac{\partial A_c^*}{\partial A_i}\right)^2 U_{A_i}^2} = \sqrt{\left(\frac{1}{A_i}\right)^2 U_{A_c}^2 + \left(-\frac{A_c}{A_i^2}\right)^2 U_{A_i}^2} \quad \text{(C-15)}$$

The Uncertainty of the Dimensionless Freezing Delay Time

$$\text{(C-16)}$$

$$t^* = \frac{t_{freezing} \cdot \sqrt{2gh}}{D_i}$$

$$U_{t^*} = \sqrt{\left(\frac{\partial t^*}{\partial t_{freezing}}\right)^2 U_{t_{freezing}}^2 + \left(\frac{\partial t^*}{\partial D_i}\right)^2 U_{D_i}^2 + \left(\frac{\partial t^*}{\partial h}\right)^2 U_h^2}$$

$$= \sqrt{\left(\frac{\sqrt{2gh}}{D_i}\right)^2 U_{t_{freezing}}^2 + \left(-\frac{t_{freezing} \cdot \sqrt{2gh}}{D_i^2}\right)^2 U_{D_i}^2 + \left(\frac{t_{freezing} \cdot g}{D_i \sqrt{2gh}}\right)^2 U_h^2}$$

The Uncertainty of Impact Velocity u

$$u = \sqrt{2gh}$$

$$U_u = \sqrt{\left(\frac{du}{dh}\right)^2 U_h^2} = \sqrt{\left(\frac{1}{2}\sqrt{\frac{2g}{h}}\right)^2 U_h^2} \quad \text{(C-17)}$$

The Uncertainty of Weber Number We

$$We = \frac{\rho u^2 D_i}{\sigma}$$

$$U_{We} = \sqrt{\left(\frac{\partial We}{\partial u}\right)^2 U_u^2 + \left(\frac{\partial We}{\partial D_i}\right)^2 U_{D_i}^2} = \sqrt{\left(\frac{2\rho u D_i}{\sigma}\right)^2 U_u^2 + \left(\frac{\rho u^2}{\sigma}\right)^2 U_{D_i}^2} \tag{C-18}$$

The Uncertainty of Impact Weber Number We$_i$

$$\mathrm{We}_i = \frac{\mathrm{We}}{0.5(1-\cos\theta_a)} = \frac{2\rho u^2 D_i}{\sigma(1-\cos\theta_a)} \tag{C-19}$$

$$U_{\mathrm{We}_i} = \sqrt{\left(\frac{\partial\,\mathrm{We}_i}{\partial\,\mathrm{We}}\right)^2 U_{\mathrm{We}}^2 + \left(\frac{\partial\,\mathrm{We}_i}{\partial\cos\theta_a}\right)^2 U_{\cos\theta_a}^2}$$

$$= \sqrt{\left(\frac{2}{(1-\cos\theta_a)}\right)^2 U_{\mathrm{We}}^2 + \left(\frac{2\,\mathrm{We}}{(1-\cos\theta_a)^2}\right)^2 U_{\cos\theta_a}^2}$$

The Uncertainty of the Total Freezing Delay Time per Volume $t_{freezing,\,V}$

$$t_{freezing,\,V} = \frac{t_{freezing}}{V_D} \tag{C-20}$$

$$U_{t_{freezing,\,V}} = \sqrt{\left(\frac{\partial t_{freezing,\,V}}{\partial t_{freezing}}\right)^2 U_{\bar{q}}^2 + \left(\frac{\partial t_{freezing,\,V}}{\partial V_D}\right)^2 U_{V_D}^2}$$

$$= \sqrt{\left(\frac{1}{V_D}\right)^2 U_{t_{freezing}}^2 + \left(-\frac{t_{freezing}}{V_D^2}\right)^2 U_{V_D}^2}$$

The Uncertainty of the Total Freezing Delay Time Diameter per Unit Mass $t_{freezing,\,m}$

$$t_{freezing,\,m} = \frac{t_{freezing}}{m_D} = \frac{t_{freezing}}{\rho V_D} \tag{C-21}$$

$$U_{t_{freezing,\,m}} = \sqrt{\left(\frac{\partial t_{freezing,\,m}}{\partial t_{freezing}}\right)^2 U_{t_{freezing}}^2 + \left(\frac{\partial t_{freezing,\,m}}{\partial V_D}\right)^2 U_{V_D}^2}$$

$$= \sqrt{\left(\frac{1}{\rho V_D}\right)^2 U_{t_{freezing}}^2 + \left(-\frac{t_{freezing}}{\rho V_D^2}\right)^2 U_{V_D}^2}$$

Appendix D Similarity Solutions for 1-D Transient Heat Conduction Equations

The similarity solutions for 1-D transient heat conduction equations in section 6.4 is presented as follows. The approach is to solve the heat transfer equation for two separate domains shown in Figure 6-3. The governing equations are expressed below:

$$\frac{\partial^2 T_{sub}}{\partial x^2} = \frac{1}{\alpha_{sub}} \cdot \frac{\partial T_{sub}}{\partial t} \text{ in the substrate domain: } 0 < x \le \delta \qquad \text{(D-1)}$$

$$\frac{\partial^2 T_w}{\partial x^2} = \frac{1}{\alpha_w} \cdot \frac{\partial T_w}{\partial t} \text{ in the droplet domain: } x \ge \delta \qquad \text{(D-2)}$$

where T_{sub} is the temperature of the substrate, T_w is the droplet temperature, h is the thickness of the substrate, α_{sub} and α_w are the thermal diffusivities of substrate and water, respectively. These governing equations are subject to the following initial and boundary conditions.

$$\begin{cases} T_{sub}(0,t) = T_{cp} \\ T_w(\delta,t) = T_{sub}(\delta,t) \\ T_w(\infty,t) = T_{impcat} \\ T_{sub}(\delta,0) = T_w(x,0) = T_{impact} \text{ at } x \ge \delta \end{cases} \qquad \text{(D-3)}$$

To solve this problem, the following variables are defined as:

$$\theta_{sub}(\eta_{sub}) = T_{sub}(x,t) - T_{impact} \qquad \text{(D-4)}$$

$$\theta_w(\eta_w) = T_w(x,t) - T_{impact} \qquad \text{(D-5)}$$

where η is the similarity parameters to reducing the partial differential equations (PDEs) to the ordinary differential equations (ODEs), expressed as follows.

$$\eta_{sub} = \frac{1}{2} \cdot \frac{x}{\sqrt{\alpha_{sub} t}} \tag{D-6}$$

$$\eta_{w} = \frac{1}{2} \cdot \frac{x}{\sqrt{\alpha_{w} t}} \tag{D-7}$$

By substituting Eq. (D-4), Eq. (D-5), Eq. (D-6) and Eq. (D-7) into Eq. (D-1) and Eq. (D-2), the original governing equations transforms to ODEs and are expressed as follows.

$$\frac{d^2\theta_{sub}}{d\eta_{sub}^{\ 2}} + 2\eta_{sub} \cdot \frac{d\theta_{sub}}{d\eta_{sub}} = 0 \tag{D-8}$$

$$\frac{d^2\theta_{w}}{d\eta_{w}^{\ 2}} + 2\eta_{w} \cdot \frac{d\theta_{w}}{d\eta_{w}} = 0 \tag{D-9}$$

By substituting Eq. (D-4), Eq. (D-5), Eq. (D-6) and Eq. (D-7) into Eq. (D-3), the initial and boundary conditions are expressed as:

$$\begin{cases} \theta_{sub}\left(\eta_{sub} = 0\right) = T_{cp} - T_{impact} \\ \theta_{w}\left(\eta_{w} = \dfrac{\delta}{2\sqrt{\alpha_{w} t}}\right) = \theta_{sub}\left(\eta_{sub} = \dfrac{\delta}{2\sqrt{\alpha_{sub} t}}\right) \\ \theta_{w}\left(\eta_{w} \to \infty\right) = 0 \text{ at } x \to \infty \\ \theta_{w}\left(\eta_{w} \to \infty\right) = \theta_{sub}\left(\eta_{sub} \to \infty\right) = 0 \text{ at } t = 0 \end{cases} \tag{D-10}$$

Eq. (D-8) and Eq. (D-9) can be reduced from second-order ODEs to first-order ODEs by substituting the following variables.

$$U_{sub} = \frac{d\theta_{sub}}{d\eta_{sub}} \tag{D-11}$$

$$U_{w} = \frac{d\theta_{w}}{d\eta_{w}} \tag{D-12}$$

The reduced first-order ODEs can be expressed as:

$$\frac{dU_{sub}}{d\eta_{sub}} + 2\eta_{sub} \cdot U_{sub} = 0 \tag{D-13}$$

$$\frac{dU_w}{d\eta_w} + 2\eta_w \cdot U_w = 0 \tag{D-14}$$

Eq. (D-13) and Eq. (D-14) can be solved and yield as follows.

$$U_{sub} = C_{1,sub} \exp\left(-\eta_{sub}\right) = \frac{d\theta_{sub}}{d\eta_{sub}} \tag{D-15}$$

$$U_w = C_{1,w} \exp\left(-\eta_w\right) = \frac{d\theta_w}{d\eta_w} \tag{D-16}$$

where $C_{1,\ sub}$ and $C_{1,\ w}$ are constants. Therefore, the solutions for Eq. (D-15) and Eq. (D-16) can be yielded as follows:

$$\theta_{sub}\left(\eta_{sub}\right) = C_{sub} + C_{2,sub} erf\left(\eta_{sub}\right) \tag{D-17}$$

$$\theta_w\left(\eta_w\right) = C_w + C_{2,w} erf\left(\eta_w\right) \tag{D-18}$$

The constant C_{sub}, $C_{2,\ sub}$ C_w, $C_{2,\ w}$ can be calculated by substituting the initial and boundary conditions.

$$\begin{cases} C_{sub} = \theta_{sub}\left(0\right) \\ C_{2,sub} = -C_{sub} = -\theta_{sub}\left(0\right) \end{cases} \tag{D-19}$$

$$\begin{cases} C_w = \theta_{sub}\left(0\right) \dfrac{erfc\left(\eta_{sub}\right)}{erfc\left(\eta_w\right)} \\ C_{2,w} = -C_w = -\theta_{sub}\left(0\right) \dfrac{erfc\left(\eta_{sub}\right)}{erfc\left(\eta_w\right)} \end{cases} \tag{D-20}$$

By substituting Eq. (D-19) and Eq. (D-20) into Eq. (D-17) and Eq. (D-18), we yield:

$$\theta_{sub}\left(\eta_{sub}\right) = \theta_{sub}\left(0\right)\left[1 - erf\left(\eta_{sub}\right)\right] = \theta_{sub}\left(0\right) erfc\left(\eta_{sub}\right) \tag{D-21}$$

$$\begin{aligned}\theta_w(\eta_w) &= \theta_{sub}(0)\frac{erfc\left(\eta_{sub}=\dfrac{\delta}{2\sqrt{\alpha_{sub}t}}\right)}{erfc\left(\eta_w=\dfrac{\delta}{2\sqrt{\alpha_w t}}\right)}\left[1-erf(\eta_w)\right]\\ &= \theta_{sub}(0)\frac{erfc\left(\eta_{sub}=\dfrac{\delta}{2\sqrt{\alpha_{sub}t}}\right)}{erfc\left(\eta_w=\dfrac{\delta}{2\sqrt{\alpha_w t}}\right)}erfc(\eta_w)\end{aligned} \tag{D-22}$$

where *erfc*(*x*) is the complementary error function and *erfc*(*x*) = 1- *erf*(*x*). By substituting Eq. (D-4) and Eq. (D-5) into Eq. (D-21) and Eq. (D-22), we yield:

$$T_{sub}(x,t)=T_{impact}+\left(T_{cp}-T_{impact}\right)erfc\left(\frac{x}{2\sqrt{\alpha_{sub}t}}\right) \tag{D-23}$$

$$T_w(x,t)=T_{impact}+\left(T_{cp}-T_{impact}\right)\frac{erfc\left(\dfrac{\delta}{2\sqrt{\alpha_{sub}t}}\right)}{erfc\left(\dfrac{\delta}{2\sqrt{\alpha_w t}}\right)}erfc\left(\frac{x}{2\sqrt{\alpha_w t}}\right) \tag{D-24}$$

Hence, the temperature at the interface T_{int} (*t*) can be estimated as follows.

$$T_{\text{int}}(t)=T_{impact}+\left(T_{cp}-T_{impact}\right)erfc\left(\frac{\delta}{2\sqrt{\alpha_{sub}t}}\right) \tag{D-25}$$

These solutions are also applicable to address the temperature profiles for the solid subcooling stage in section 6.4.4.

Appendix E MATLAB Code for the Droplet Freezing on Substrate Surfaces

Nucleation

```
clear all;

close all;

clc
```

Comment parameters

```
% Contact angle (\dgree)

CA = deg2rad(input value);


% Final contact diameter

D_c = input value;


% Calculating time

period = input value;


% Nucleating particle size

R_p = input value;


% Botlzmann constant

k_B = 1.38064*10^(-23);
```

```
% Droplet volume

V_0 = input value;


% Initial temperature of the water droplet

T_impact = = input value + 273.15;


% Thickness of the sample

delta = input value;


% The temperature of the cold plate

T_cp = input value + 273.15;


% Assumed constant

C_A = input value

% Time span

span_t = 0.05;
```

Symoblic simplification

```
syms alpha_sub rho_s c_p_s k_s t

% Temperature of the interface before the nucleation stage

T = T_impact+(T_cp-T_impact)*erfc(h/(2*(sqrt(alpha_sub*t))));
```

```
% The thermal diffusibity of sample
Asub = k_s/(rho_s*c_p_s);
T = subs(T,alpha_sub,Asub);
T = subs(T,[h k_s rho_s c_p_s],[0.0008 17 7780 400]);
T = vpa(simplify(T));

syms T_m Delta_H_v
% The free energy difference for unit volume of ice embryo between matter in water and ice.
Delta_G_v = ((T-T_m )/T_m)*Delta_H_v;
Delta_G_v = subs(Delta_G_v,[T_m Delta_H_v],[273.15 334000000]);

syms C_1 C_2
% Surface tension
sigma_IW = C_1 +C_2*(T-T_m);
sigma_IW = subs(sigma_IW,[C_1 C_2 T_m],[0.028 0.00025 273.15]);

% The radius of the critical ice embryo
r_str = -2*sigma_IW/Delta_G_v;
r_str = simplify(r_str);

% m is the cosine of contact angle between ice and the nucleating material
syms sigma_IG sigma_WG theta
```

```
symstr_m = (sigma_IG-sigma_WG)*cos(theta)/sigma_IW;
m = subs(symstr_m,[sigma_IG sigma_WG],[0.106 0.077]);
m = simplify(subs(m,theta,CA));

% X is the ratio between the radius of the nucleating particle and the radius of the critical ice embryo
X = R_p/r_str;

% g is a function of X and m
g = (1-2*m*X+X^2)^(1/2);

% The geometrical factor f
f = 1+(((1-m*X)/g)^3)+(X^3)*(2-3*((X-m)/g)+(((X-m)/g)^3))+3*m*(X^2)*(((X-m)/g)-1);

% The critical free energy barrier for nucleation
Delta_G_str = simplify(8*pi*(sigma_IW^3)*(f/(3*(Delta_G_v^2))));

% N_A is Avogadro's constant
% rho_w is the density of water (kg/m^3)
% M_w is the Molecular weight of water (kg/mol)
% rho_s is the density of ice (kg/m^3)
syms N_A rho_w M_w rho_s
```

```
% n_l is the number density of molecules in the liquid
n_l = N_A*rho_w/M_w;

% n_s is the number density of molecules in the solid
n_s = N_A*rho_s/M_w;
n_l = subs(n_l,[N_A rho_w M_w],[6.022*10^23 999.8 18.05*10^(-3)]);
n_l = vpa(simplify(n_l));
n_s = subs(n_s,[N_A rho_s M_w],[6.022*10^23 916.2 18.05*10^(-3)]);
n_s = vpa(simplify(n_s));

% Another geometrical factor in the Zeldovich factor
zeta_f = (1-X*cos(theta))*(2-4*X*cos(theta)-(X^2)*(((cos(theta))^2)-3))/((1-2*X*cos(theta)+(X^2))^(3/2));
zeta_f = simplify(subs(zeta_f,theta, CA));

% The Zeldovich factor
Z_het = ((sigma_IW/(k_B*T))^(1/2))*((4/(2+zeta_f))^(1/2))/(2*pi*n_s*(r_str^2));
Z_het = simplify(Z_het);

% The mean particle separation distance
r_0 = (3/(4*pi*n_s))^(1/3);

% The surface area of a water molecule
```

```
A = vpa(4*pi*r_0^2);

% The critical number of water molecules in ice embryo
i_str = ((r_str*n_s*A)/3)^3;

% The self-diffusion coefficient of water
D_T = (4*10^(-8))*exp(-371/(T-169.1));
pro_ist = (nthroot(i_str,3))^2;

% The net rate of attachment to the critical nucleus
F = A*D_T*(n_l^(4/3))*pro_ist;
a1 = k_B*T;
a2 = exp(-1*(Delta_G_str/a1));

% The nucleation rate
 J = n_l*Z_het*F*exp((-Delta_G_str*C_A)/(k_B*T));
V_c = simplify((4/3)*pi*r_str);
Fun_t = simplify((V_0-V_c)*J);

% Time series
start_time = 0;
Time = start_time:span_t:period;
```

Integration

```
% Let f(t) = (V_0 - V_c)*J

Fun_t_r = zeros(1,length(time));

J_t_r = zeros(1,length(time));

Area = zeros(1,length(time));


for i = 1:length(time)

    if i1 == 1

        continue

    else

    mid_time = (time(i)+time(i-1))/2;

    % value of f(t)

    Fun_t_r(i) = subs(Fun_t,t,mid_time);

    % value of J(t)

    J_t_r(i) = subs(J,t,mid_time);

    % Area under the curve

    Area(i) = Fun_t_r(i)*span_t;

    end

end


% Total area under the curve

Total_Area = zeros(1,length(Area));

for j = 1:length(Area)
```

```
    if j == 1
        Total_Area(1) = Area (1);
    else
        Total_Area(j) = Total_Area(j-1) + Area(i);
        if Total_Area(j) == inf
            Total_Area(j) = 0;
        end
     end
 end

% Find N~1
standard_num = 1;
for z = 2:length(Area)
    if abs((standard_num - Total_Area(z))) < abs((standard_num – Total_Area(z)))
       Approximate_N = Total_Area(z);
       Nucleation_t = time(z);
       A_sub_1 = 17/(7780*400);
       Nucleation_T = (T_d+(T_sub-
T_d)*erfc(h/(2*(sqrt(A_sub_1*Nucleation_t)))))-273.15;
     end
 end
```

1-D One Region Stefan Problem

```
% Latent heat fusion

H_L_s = 334000;

% Heat capacity of ice

C_p_s_1 = 2100;

% Heat capacity of water

C_p_w_1 = 4200;

% Density of water

rho_w_1 = 999.8;

% Density of ice

rho_s_1 = 916.;

% Thermal conductivity of water

k_w_1 = 0.555;

% Thermal conductivity of ice

k_s_1 = 2.22;

% Melting temperature of ice

T_m = 0;


A_w = (k_w_1/(C_p_w_1*rho_w_1));

A_s = (k_s_1/(C_p_s_1*rho_w_1));

v = sqrt(A_w/A_s)


syms lambda
```

```
eqn =((C_p_s_1*(T_m-Nucleation_T))/H_L_s)/((exp(lambda^(2)))*erf(lambda)) ==
lambda*sqrt(pi)
Lambda_sol = solve(eqn,lambda,"Real",true)
Lambda_sol = double(Lambda_sol);


% The tadius of the 2-D project droplet (front)
r_c = D_c /(2*sin(CA));
if CA < deg2rad(90)
        % 2-D Project Area of the Droplet
        A_c = CA*(r_c^(2))-(D_c/2)*r_c*cos(CA);
        % Characteristic length
        L = A_c/ D_c;
        % Equilibrium Solidification Time
        t_s = ((L / (2 * Lambda_sol))^(2))/(A_s);
else
        %theta >= 90 deg.
        A_c = (pi-CA)*(r_c^(2))-(D_c/2)*r_c*cos(CA);
        L = A_c/ D_c;
        t_s = ((L / (2 * Lambda_sol))^(2))/(A_s);
end
t_s = double(t_s);


% the Total Freezing Delay Time
```

```
t_freezing = Nucleation_t + t_s;
t_freezing = double(t_freezing);
t_freezingm = (t_freezing / (rho_w_1*V_0)) * 10^(-6);
A_c = double(A_c);
r_c = double(r_c);
Final_results = table (Nucleation_t,Approximate_N,Nucleation_T,Lambda_sol,r_c,A_c,X,t_s,t_freezing,t_freezingm,'VariableNames',["t_n (s)", "N ~ 1","T_n (*C)","Lambda","r_c (m)","A_c (m2)","Solidification Thickness L (m)","t_s (s)","t_freezing (FDT) (s)","unit mass FDT (s/kg)"]);
Final_results_trans = rows2vars(Final_results)
```

Appendix F Publications by the Candidate

F.1 Journal publications

1 **K. Shi**, X. Duan, Freezing delay of water droplets on metallic hydrophobic surfaces in a cold environment, Appl. Therm. Eng. 216 (2022) 119131. https://doi.org/10.1016/j.applthermaleng.2022.119131.

2 **K. Shi**, X. Duan, A Review of Ice Protection Techniques for Structures in the Arctic and Offshore Harsh Environments, J. Offshore Mech. Arct. Eng. 143 (2021). https://doi.org/10.1115/1.4050893.

3 **K. Shi**, J. Elms, X. Duan, K.M. Poduska, Droplet asymmetry and wetting dynamics on irregularly roughened surfaces, J. Coatings Technol. Res. 18 (2021) 911–919. https://doi.org/10.1007/s11998-020-00456-8.

4 Y. Pan, **K. Shi**, X. Duan, G.F. Naterer, Experimental investigation of water droplet impact and freezing on micropatterned stainless steel surfaces with varying wettabilities, Int. J. Heat Mass Transf. 129 (2019) 953–964. https://doi.org/10.1016/j.ijheatmasstransfer.2018.10.032.

F.2 Conference proceedings

1 **K. Shi**, X. Duan, Heat Transfer Analysis of Icing Process on Metallic Surfaces of Different Wettabilities, in: H. Okada, S.N. Atluri (Eds.), Comput. Exp. Simulations Eng., Springer, Cham, 2020: pp. 201–206. https://doi.org/10.1007/978-3-030-27053-7_19.

2 **K. Shi**, X. Duan, The Icing Process of Water Droplet Postponed on the Zinc-Deposited Steel Surface in a Low-Temperature Environment, in: Prog. Can. Mech. Eng. Vol. 3,

University of Prince Edward Island. Robertson Library, Charlottetown, P.E.I., 2020. https://doi.org/10.32393/csme.2020.1133.

3 S. S. Rhythm, **K. Shi**, X. Duan, "Measurement of Ice Adhesion on Stainless Steel Hydrophobic Surfaces", CSME-CFDSC Congress 2019, June 2-5, 2019, London, Canada

4 Y. Pan, **K. Shi**, X. Duan, G.F. Naterer, "Droplet impact, spreading and freezing on metallic surfaces of varying wettability", CSME International Congress 2018, May 27-30, 2018, Toronto, Canada.

5 **K. Shi**, F. Su, H. Ma, X. Duan, Thin Film Evaporation of Liquid Nitrogen on a Micro Structured Surface, in: Proceeding Second Therm. Fluids Eng. Conf., Begellhouse, Connecticut, 2018: pp. 2647–2653. https://doi.org/10.1615/tfec2017.mst.017617.

6 Y. Pan, **K. Shi**, X. Duan, G.F. Naterer, "Experimental investigation of droplet oscillation and impact on hydrophilic and hydrophobic surfaces with varying wettability", 26th CANCAM Conference, May 29 – June 1, 2017, Victoria, Canada.